Cavity State Reservoir Engineering in Circuit Quantum Electrodynamics

A Dissertation
Presented to the Faculty of the Graduate School
of
Yale University
in Candidacy for the Degree of
Doctor of Philosophy

by
Eric T. Holland

Dissertation Director: Robert J. Schoelkopf

December 2015

Abstract

Cavity State Reservoir Engineering in Circuit Quantum Electrodynamics

Eric T. Holland
2015

Engineered quantum systems are poised to revolutionize information science in the near future. A persistent challenge in applied quantum technology is creating controllable, quantum interactions while preventing information loss to the environment, decoherence. In this thesis, we realize mesoscopic superconducting circuits whose macroscopic collective degrees of freedom, such as voltages and currents, behave quantum mechanically. We couple these mesoscopic devices to microwave cavities forming a cavity quantum electrodynamics (QED) architecture comprised entirely of circuit elements. This application of cavity QED is dubbed Circuit QED and is an interdisciplinary field seated at the intersection of electrical engineering, superconductivity, quantum optics, and quantum information science. Two popular methods for taming active quantum systems in the presence of decoherence are discrete feedback conditioned on an ancillary system or quantum reservoir engineering. Quantum reservoir engineering maintains a desired subset of a Hilbert space through a combination of drives and designed entropy evacuation. Circuit QED provides a favorable platform for investigating quantum reservoir engineering proposals. A major advancement of this thesis is the development of a quantum reservoir engineering protocol which maintains the quantum state of a microwave cavity in the presence of decoherence. This thesis synthesizes strongly coupled, coherent devices whose solutions to its driven, dissipative Hamiltonian are predicted *a priori*. This work lays the foundation for future advancements in cavity centered quantum reservoir engineering protocols realizing hardware efficient circuit QED designs.

Contents

List of Figures

List of Tables

Publication List

This thesis is based on the following publications:

1. M. Reagor, W. Pfaff, C. Axline, R. W. Heeres, N. Ofek, K. Sliwa, E. T. Holland, C. Wang, J. Blumoff, K. Chou, M. J. Hatridge, L. Frunzio, M. H. Devoret, L. Jiang, and R. J. Schoelkopf. (2015)

2. E. T. Holland, B. Vlastakis, R. W. Heeres, M. J. Reagor, U. Vool, Z. Leghtas, L. Frunzio, G. Kirchmair, M. H. Devoret, M. Mirrahimi, and R. J. Schoelkopf. Accepted for publication in *Phys. Rev. Lett.* (2015)

3. R. W. Heeres, B. Vlastakis, E. T. Holland, S. Krastanov, V. V. Albert, L. Frunzio, L. Jiang, and R. J. Schoelkopf. *Phys. Rev. Lett.* 115, 137002 (2015)

4. M. J. Reagor, H. Paik, G. Catelani, L. Sun, C. Axline, E. T. Holland, I. M. Pop, N. A. Masluk, T. Brecht, L. Frunzio, et al. *Appl. Phys. Lett.* 102, 192604 (2013)

Acknowledgments

First and foremost I would like to thank my advisor, Robert Schoelkopf, for the past six years. Much of what I have learned about microwave and quantum measurement has been through discussions with him. Furthermore, the 4^{th} floor of Becton is a hub of innovative quantum research. Few other places can boast the intellectual and physical resources that are available there. Next I would like to thank Luigi Frunzio for his unbridled enthusiasm for science coupled with his meticulous attention to detail. It has been a pleasure working with and learning from Luigi over the last six years. Michel Devoret has been a seemingly never ending source for profound pedagogical insight into physics. An under appreciated quality of Michel is his wit. Being funny in your native language is a skill most people never acquire and it is all the more impressive when it is achieved consistently in another language. Lastly, I would like to thank Mazyar Mirrahimi for all his discussions where he clearly and succinctly unveiled the underlying physics.

As a whole I would like to thank present and past RSL and QuLab members. I am forever indebted for their contributions and daily interactions. I would like to thank Matt Reagor for the past five years. He is a dear friend, a sounding board for ideas, and generally has great insight into a variety of topics. Brian Vlastakis has consistently been a fun and upbeat guy to discuss physics with and for that I thank him. Reinier Heeres was fantastically helpful in regards to the work done in chapter 6 and I thank him for helping me refining measurement techniques. Gerhard Kirchmair was an extremely positive and popular force in RSL. I am forever indebted to him for teaching me the fundamentals of quantum measurement. I would like to thank Adam Sears for being the person who always knew that answer for questions I weren't sure who to ask. Finally, I would like to thank Luyan Sun for all the early work we did in developing what is presented in chapter 3.

1

Introduction

Quantum mechanics is amongst the most visible branches of physics. Yet the concept of quantization in the real world to a general audience is initially baffling. Discussing the quantization of examples such as currency or integer numbers are largely considered straight-forward; however, the quantization of our natural world requires inherent complications such as the wave-like behavior of

matter. This creates abstract physical and philosophical concepts not easily intuited by laymen and experts alike. Fortunately, quantum optics, a subfield of quantum mechanics, theoretically and experimentally investigates counterintuitive quantum phenomena solidifying in experiment what initially seems to be philosophical.

As an experimentalist, the theoretical development of quantum mechanics is all the more impressive considering the technological state of the early 20^{th} century. One cannot help but wonder how a modern day version of the Bohr-Einstein letters would read if they were able to cite present day work where one routinely has full quantum control over an atom, artificial atom, or a single photon. For instance, Schrödinger remarked, "we never experiment with just one electron or atom or molecule. In thought-experiments we sometimes assume that we do; this invariably entails ridiculous consequences... we are not experimenting with single particles any more than we can raise Ichthyosauria in the zoo" [1]. However, at the start of the 21^{st} century a wide range of experimental platforms exist to investigate single photon or single atom interactions verifying and expanding early theories.

The 1980's had truly foundational work in not only quantum computing but also in the development of mesoscopic systems that would thrive in quantum information experiments some twenty years later. One may wonder if the rich and unique physics that occurs with single or small number of atoms can be analogously achieved with a large collection of atoms. This may at first seem a little far fetched but early in a mechanics course, Newton's 3^{rd} law is used to explain

how an extended object can be treated as a point particle. Anthony Leggett theoretically undertook the question of whether or not a massively macroscopic system such as a circuit could exhibit quantum behavior and be faithfully described by a few quantum operators [2, 3]. Furthermore, Leggett along with Caldeira investigated coupling to an infinite sea of harmonic oscillators giving rise to tunneling [4]. On the experimental front, at the University of California at Berkeley Michel Devoret, John Martinis, and John Clarke (thirty years later all are familiar names in the quantum superconducting circuit community) carried out the first demonstration of the quantum mechanical nature of electrical circuits [5, 6, 7, 8, 9]. Electrical circuits typically have of order Avogadro's number of atoms and for quantum mechanical processes to be apparent the degrees of freedom of the system must be substantially less than the number of atoms involved which further underscores how impressive and fundamental this work was. In hindsight, it would seem exploiting these artificial atoms for quantum computing or quantum optics would be a natural progression. However, in a sense, these landmark discoveries predated their future applications. Neither quantum computing nor quantum optics were the well developed fields that they are today. It wasn't until the late 90's that superconducting circuits were explicitly demonstrated with an outlook towards quantum computing [10, 11].

Towards the end of his life, Richard Feynman was a proponent of developing quantum machines. Feynman's insight was that some tasks such as simulating a quantum system, may be accomplished more naturally with a well controlled quantum system rather than a classical system [12]. The first hard look

at quantum computing was by David Deutsch in 1985 [13]. From there theoretical investigations in both quantum algorithms and the necessary quantum error correction to make said quantum algorithms possible in the presence of noise took off in the 90s [14, 15, 16, 17, 18, 19, 20, 21]. A foundational reference to quantum computation and information is the textbook by Nielsen and Chuang [22] whose initial release is temporally closer to the first few quantum algorithms than present day. In the coming years the first logical qubit will be experimentally demonstrated which can be thought of as the first quantum transistor–the foundational bit that will comprise a quantum computer.

Looking back historically it is not necessarily the first demonstration of a given technique that becomes ubiquitous in the field but rather the demonstration which can most easily overcome its current obstacles. For instance, an early leader in experimental demonstrations of quantum computing and quantum algorithms was NMR [23, 24, 25, 26]. However, progress in NMR based quantum computation has largely been stymied by fundamental obstacles [27]. Since this is a dissertation focused on quantum phenomena in superconducting circuits it is inherently biased towards that application. However, other systems also offer viable platforms for the pursuit of quantum computation. A leading implementation is ion trapped based systems [28, 29, 30, 31, 32]; however, other platforms exist such as optical lattices of neutral atoms [33], semiconductor quantum dots [34, 35, 36, 37, 38], and diamond nitrogen vacancy centers [39, 40, 41, 42, 43].

1.1 Thesis Overview

This thesis contains work that incrementally advances the field of circuit quantum electrodynamics. Chapter 2 lays the foundation and sets the tone of this thesis by describing common electrical circuits that will be realized. A successful approach to circuit based quantum systems is by attacking the problem as an RF engineer. Chapter 2 describes circuits as harmonic oscillators and quantifies loss mechanisms of circuits which serves as a guiding principle in designing experiments.

Chapter 3 is devoted to the early stage development of a scalable technology. Early designs and experiments of an architecture that combines and leverages highly coherent 3D structures with the robustness of lithographically defined features. Great progress has been achieved on this front but fundamental investigations on design and integration are ongoing.

Chapter 4 serves as a brief introduction to the rich field of circuit quantum electrodynamics. Some key topics are discussed to give the reader a sense and a flavor for the field; however, it does not aim to be an exhaustive review of the field of quantum information with superconducting circuits.

Chapter 5 is devoted to the experimental techniques used to make, measure and characterize quantum devices at microwave frequencies.

Chapter 6 presents two unique advances in circuit quantum electrodynamics. The first being a single photon resolved cavity-cavity state dependent shift. The state dependent shift enables a demonstration of a protocol that stabilizes

photon number states in one of the microwave cavities.

Finally, the dissertation ends in chapter 7 with concluding remarks and a warranted positive outlook for the field of quantum information with superconducting circuits.

2

Resonator Theory

This chapter lays the foundation upon which the rest of this thesis is built. We begin with a classical description of resonators in terms of their circuit components: capacitors, inductors, and transmission lines. We do this because we will understand the constituents of our superconducting systems, artificial atoms and cavities, in terms of circuit elements. Additionally, we will use these circuit

elements to understand coupling between artificial atoms and cavities as well as the coupling to the external environment. In later chapters, using only circuit components a cavity quantum electrodynamics analogue will be achieved. The circuit analogue to cavity quantum electrodynamics is realized with circuit elements comprising both the cavities and the artificial atoms dubbed circuit quantum electrodynamics or simply cQED.

Furthermore, resonators provide a means to investigate the loss mechanism of our cQED systems. Since our circuit systems are designed and fabricated by the scientist it is unclear which superconductors, if any, are more suitable building blocks for resonators and artificial atoms. The final part of this chapter is devoted to developing the concept of participation ratios which provides a means to make "apples" to "apples" comparisons between the wide variety of resonators and artificial atoms in the 5-10 GHz regime. Having the concept of participation ratios is of paramount importance for progress to continue at the historically accustomed rate [44] in the superconducting circuit community.

2.1 LC Circuit

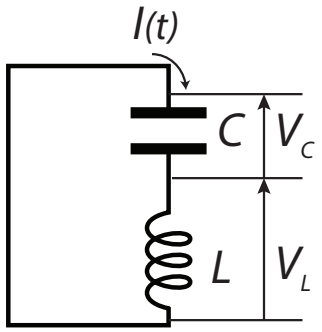

Figure 2.1: LC Circuit Diagram. An ideal capacitor, C, is connected in series with an ideal inductor, L. We will describe the harmonic motion of either the charge on the capacitor, $Q(t)$, or its conjugate variable the flux in the inductor, $\Phi(t)$.

We will begin with a simple series inductor-capacitor (L, C) system that is isolated from the environment (Fig. 2.1). Looking at the voltage drop around this circuit, we can derive the equations of motion for the charge on the capacitor, $Q(t)$:

$$\begin{aligned} V_C + V_L &= 0 \\ \frac{Q(t)}{C} + L\frac{\mathbf{d^2}Q(t)}{\mathbf{dt^2}} &= 0 \\ \frac{\mathbf{d^2}Q(t)}{\mathbf{dt^2}} + \frac{Q(t)}{LC} &= 0 \qquad (2.1) \\ \frac{\mathbf{d^2}Q(t)}{\mathbf{dt^2}} + \omega_0^2 Q(t) &= 0 \qquad (2.2) \end{aligned}$$

We notice that the solution to our equation in terms of the charge on the capacitor, $Q(t)$, satisfies a harmonic oscillator equation with $\omega_0^2 = \frac{1}{LC}$. In later

chapters, we will rely on the fact that an LC circuit is a harmonic oscillator when electrical circuits are quantized. For completeness we demonstrate that the flux in the inductor also satisfies the harmonic oscillator equation and begin again with the voltage:

$$V_L + V_C = 0$$

$$\frac{\mathbf{d^2}\Phi(t)}{\mathbf{dt^2}} + \frac{\Phi(t)}{LC} = 0 \tag{2.3}$$

$$\frac{\mathbf{d^2}\Phi(t)}{\mathbf{dt^2}} + \omega_0^2\Phi(t) = 0 \tag{2.4}$$

As expected the flux in the inductor, $\Phi(t)$, also satisfies the harmonic oscillator equation with the same resonance frequency found in equation 2.2 ($\omega_0^2 = \frac{1}{LC}$). Conceptually one could think of the charge sloshing back and forth from the different sides of the capacitor through the inductor versus the time dynamics of the flux. However, in chapter 4 we will find that it is easier to describe our systems in terms of the flux because the nonlinearities introduced by the Josephson junction perturb the potential when described in the flux basis rather than when describing the charge and distorting the 'mass'. Regardless, as we have shown either variable satisfactorily describes an LC circuit as a harmonic oscillator which we will make use of later in cQED systems.

2.2 LCR Circuit

It is useful to expand the work in the previous section to include dissipation. Practically speaking, there will always be some form of dissipation in any circuit

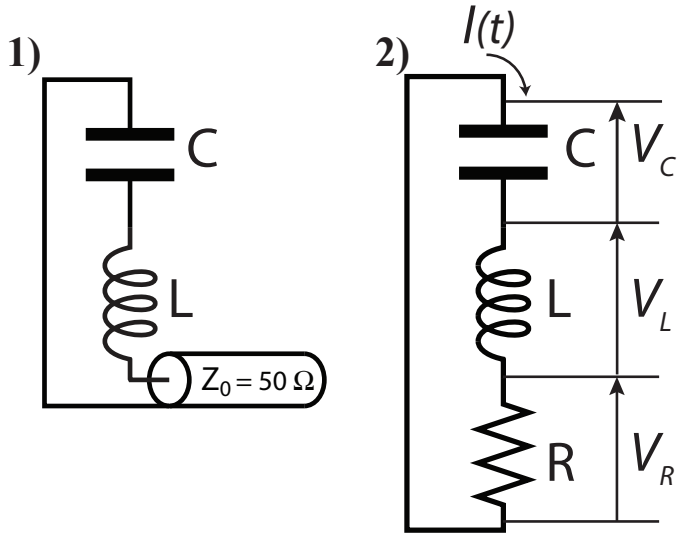

Figure 2.2: LCR Circuit Diagram. **1** An ideal capacitor, C, is connected in series with an ideal inductor, L which are connected to a transmission line with $Z_0 = 50\ \Omega$. **2** The transmission line can be replaced with a dissipative resistor, R. This LCR circuit will be described as a damped harmonic motion in terms of the charge on the capacitor, $Q(t)$.

whether it be in the form of intended coupling to the 50 Ω world, resistive heating, or residual coupling to the environment. One consequence of dissipation is that our resonances will have a nonzero bandwidth. A finite, or even large bandwidth, is desirable for the measurement chain enabling repeated quantum non-demolition measurements [45, 46]. Dissipation in the form of information removal from the quantum system under study to the physicist is advantageous and necessary.

In figure 2.2 dissipation is taken into account by including a resistor, R. The voltage for this term will generally be $V_R = \frac{\mathbf{d}Q(t)}{\mathbf{dt}}R + V_N(t)$ where $V_N(t)$ is the noise term of the resistor. The noise of the resistor is non-neglible for excita-

tions of a few photons; however, if we restrict our view to large excitations we can suppress the noise term and eq. 2.1 becomes:

$$\frac{\mathbf{d^2}Q(t)}{\mathbf{dt^2}} + \frac{\mathbf{d}Q(t)}{\mathbf{dt}}\frac{R}{L} + \frac{Q(t)}{LC} = 0 \tag{2.5}$$

$$\frac{\mathbf{d^2}Q(t)}{\mathbf{dt^2}} + 2\alpha\frac{\mathbf{d}Q(t)}{\mathbf{dt}} + \omega_0^2 Q(t) = 0 \tag{2.6}$$

The LCR circuit takes the form of a damped harmonic oscillator with damping attenuation $\alpha = \frac{R}{2L}$, resonance frequency of $\omega_0^2 = \frac{1}{LC}$, and damping factor, ζ defined as:

$$\zeta = \frac{\alpha}{\omega_0} = \frac{R}{2}\sqrt{\frac{L}{C}} = \frac{R}{2\omega_0 C} \tag{2.7}$$

Since our LCR circuits will be relatively low loss, superconductors at gigahertz frequencies, we can ignore corrections to the resonance frequency of the oscillator due to damping.

2.3 Quality factors

The quality factor, Q, of a resonator is defined as:

$$\mathrm{Q} = \omega_0 \frac{\text{average energy stored}}{\text{dissipated power}} \tag{2.8}$$

Q is an important quantity not only because it defines the bandwidth of the resonance ($\mathrm{BW} = \frac{1}{\mathrm{Q}}$) but also because it quantifies the different loss mechanisms of our RF circuits.

2.3.1 Quality Factor Parallel LCR Circuit

To determine the quality factor of a parallel LCR circuit we begin by looking at the power dissipated by the resistor, P_d:

$$P_d = \frac{V^2}{2R} \tag{2.9}$$

The average stored energy in the electric field by the capacitor, E_c, will be:

$$E_c = \frac{1}{4}V^2C \tag{2.10}$$

Also, the average stored energy in the magnetic field by the inductor, E_i, will be:

$$E_i = \frac{1}{4}\frac{V^2}{\omega_0^2 L} \tag{2.11}$$

If we now use equations, 2.9, 2.10, and 2.11 in equation 2.8 we get:

$$\begin{aligned} \mathrm{Q}_{\,\mathrm{LCR}} &= \omega_0 \frac{\frac{1}{4}V^2C + \frac{1}{4}V^2/(\omega_0^2 L)}{\frac{V^2}{2R}} \\ \mathrm{Q}_{\,\mathrm{LCR}} &= \omega_0 RC = \omega_0 \tau \end{aligned} \tag{2.12}$$

In the case of a parallel LCR circuit we see that the bandwidth will be set by the resonance frequency of the oscillator as well as its "RC" time which is defined in the usual way as τ. From equation 2.12 we notice that for a fixed total quality factor the total lifetime of the circuit can be increased simply by lowering the resonance frequency and not at all altering the dissipation. This is a

reason why discussing the quality factor of a resonance is preferred to discussing the lifetime of a resonance. It must be noted that one cannot make the resonance frequency of the artificial atom or resonator arbitrarily low just to have a long lifetime. One reason is that lowering the frequency makes is easier for the thermal bath to provide excitations. For instance 1 GHz corresponds to roughly 50 mK. Other considerations when lowering the frequency of artificial atoms are, for charge based designs such as the transmon, that charge dispersion (dephasing) grows exponentially as the frequency of the device is lowered [47].

For completeness we note that for an oscillator its quality factor can always be written in the form of equation 2.12 as well as being written as [48]:

$$\mathrm{Q} = \frac{\omega_0}{\Delta\omega_0} = \frac{f_0}{\Delta f_0} \tag{2.13}$$

Additionally, for series circuit elements we can define the quality factor in terms of its impedance, $Z(\omega)$, as:

$$\mathrm{Q} = \frac{\mathbf{Im}[Z(\omega)]}{\mathbf{Re}[Z(\omega)]} \tag{2.14}$$

Also, for the case of parallel circuit elements we can define the quality factor in terms of the admittance, $Y(\omega)$, as:

$$\mathrm{Q} = \frac{\mathbf{Im}[Y(\omega)]}{\mathbf{Re}[Y(\omega)]} \tag{2.15}$$

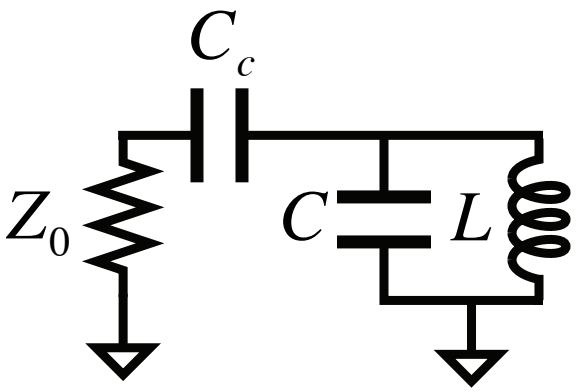

Figure 2.3: Coupling to LC Oscillator. We model coupling to an LC oscillator as a series coupling capacitor, C_c, to the Z_0 of the environment.

2.4 Coupling to LC Oscillator

We begin with the case of an LC oscillator capacitively coupled to the Z_0 (50 Ω) environment by a coupling capacitor, C_c, as shown in figure 2.3. The coupling capacitor and the Z_0 (50 Ω) line can be described as a shunt admittance Y_s:

$$Y_s = j\omega C_c \frac{1 - jq}{1 + q^2} \tag{2.16}$$

In equation 2.16 we have defined $q = \omega Z_0 C_c$. We take the real part of this shunt admittance because it will in part determine the quality factor of our resonance.

$$\mathbf{Re}[Y_s] \approx \frac{q^2}{Z_0} \tag{2.17}$$

In equation 2.17 we have made the simplification that $q \ll 1$. Using equation 2.17 the total quality factor of the LC oscillator is:

$$\begin{aligned} Q &= \frac{\omega_0 C}{\mathbf{Re}[Y_s]} \\ Q &= \frac{\omega_0 C Z_0}{q^2} \end{aligned} \tag{2.18}$$

For the LC oscillator we remember that its resonance frequency, ω_0, and its characteristic impedance, Z_c, are:

$$\omega_0 = \frac{1}{\sqrt{LC}} \tag{2.19}$$

$$Z_c = \sqrt{\frac{L}{C}} \tag{2.20}$$

Using equations 2.19 and 2.20 we solve for the capacitance as:

$$C = \frac{1}{\omega_0 Z_c} \tag{2.21}$$

Now we simplify equation 2.18 by using equation 2.21:

$$Q = \frac{1}{q^2}\frac{Z_0}{Z_c} \tag{2.22}$$

$$Q \approx \frac{1}{q^2} \tag{2.23}$$

$$C_c = \frac{1}{\omega_0 Z_0 \sqrt{Q}} \tag{2.24}$$

To go from 2.22 to equation 2.23 we make the approximation that the characteristic impedance of the transmission line normalized by the characteristic impedance of the LC oscillator is of order unity. From equation 2.24 we can now estimate the value of the capacitor needed to have a total quality factor of no worse than a million. If we assume a resonance at 8 GHz and a characteristic impedance of 50 Ω then our coupling capacitor is 400 aF. For a total quality factor of 10^{10} this would require a net coupling capacitor of 4 aF. This is why the evanescent coupling, which allows exponential suppression to the external environment, is so useful in realizing weak coupling.

2.5 Participation Ratios

In this final section, quality factors are used to develop the concept of participation ratios giving an implementation independent means to describe dissipation in a RF circuit.

2.5.1 Lossy Capacitor

We begin our investigation into participation ratios by looking at a capacitor whose loss originates from having a material with a complex dielectric constant, $\epsilon = \epsilon_r + i\epsilon_i$ ($i = \sqrt{-1}$). As a simple example we will look at a parallel plate capacitor (Fig. 2.4) which we acknowledge for all frequencies is not a capacitor [49] but nevertheless gives insight into the problem of handling a lossy capaci-

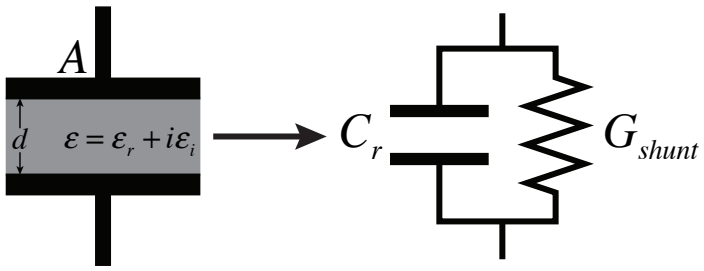

Figure 2.4: Lossy Parallel Plate Capacitor. To frame the discussion of participation ratios a lossy parallel plate capacitor will be considered. The results for describing the lossy parallel plate capacitor will be quite general and not specific to this geometry. We decompose the lossy capacitor into an idealized capacitor, C_r shunted by a lossy element G_{shunt}.

tor. In general, the admittance for a capacitor is simply:

$$Y_c = j\omega C \tag{2.25}$$

Where C is the capacitance of the object, ω is the angular frequency, and j is in the standard electrical engineer definition ($j = -i$). In the case of a parallel plate capacitor filled with a material with a complex dielectric constant the capacitance for this parallel plate is:

$$C_{pp} = \epsilon \frac{A}{d} \tag{2.26}$$

Where ϵ is the complex permittivity, A is the area of the plates, and d is the distance for the plates (Fig. 2.4). If we use equation 2.26 in equation 2.25 then

the admittance for this lossy capacitor is:

$$Y_{cpp} = j\omega\epsilon\frac{A}{d} \tag{2.27}$$

Explicitly writing out the complex permittivity equation 2.27 becomes:

$$\begin{aligned} Y_{cpp} &= j\omega(\epsilon_r + i\epsilon_i)\frac{A}{d} \\ Y_{cpp} &= j\omega\epsilon_r\frac{A}{d} + ji\omega\epsilon_i\frac{A}{d} \\ Y_{cpp} &= j\omega\epsilon_r\frac{A}{d} + \omega\epsilon_i\frac{A}{d} \qquad (2.28) \\ Y_{cpp} &= j\omega C_r + G_{\text{shunt}} \qquad (2.29) \end{aligned}$$

We rewrite our result in equation 2.28 as two terms in equation 2.29. The first term in equation 2.29 stores energy in the **E** or **D** fields and acts as an idealized capacitor. The second term in equation 2.29 is a dissipative term which shunts the idealized capacitor. This shunt resistance, G_{shunt}, is not ohmic and has zero DC contribution but has an appreciable RF value. To determine the quality factor of this lossy capacitor we can take the ratio between the imaginary and the real parts of equation 2.29:

$$\begin{aligned} \text{Q}_{\ cpp} &= \frac{\mathbf{Im}[Y_{cpp}]}{\mathbf{Re}[Y_{cpp}]} \\ \text{Q}_{\ cpp} &= \frac{\epsilon_r}{\epsilon_i} = \frac{1}{\tan\delta} \qquad (2.30) \end{aligned}$$

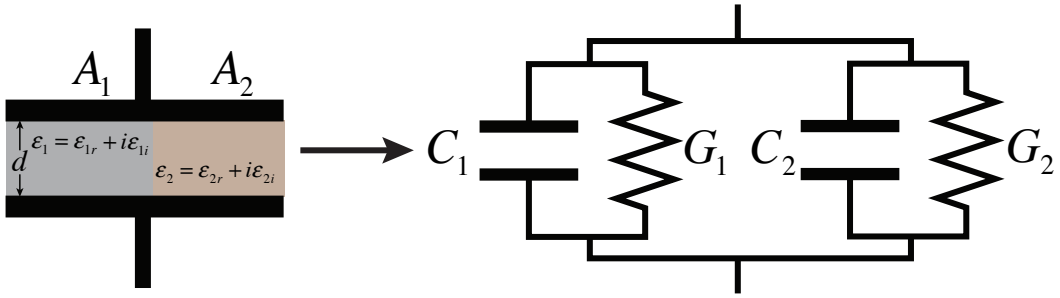

Figure 2.5: Lossy Capacitor-Two Dielectrics: Parallel. Parallel plate capacitor with lossy dielectrics whose surface interface is parallel to **E** or **D** fields is considered. The above case of a parallel plate capacitor filled with two different complex dielectrics $\epsilon_{\mathbf{1,2}}$ is presented. The two different regions can be modeled as an idealized capacitor $C_{1,2}$ shunted by $G_{1,2}$ with each region circuit equivalent being in parallel with the other regions circuit equivalent.

In equation 2.30 we find a relationship between the quality factor of this circuit element and its loss tangent, $\tan\delta$. The loss tangent of a dielectric is a common materials property in electrical engineering [48] which is generally held to be a frequency independent quantity. We find that in the case of the lossy capacitor, the quality factor is set by the loss tangent of the dielectric.

2.5.2 Partially Filled Lossy Capacitor-Parallel

The next two sections are devoted to a more realistic situation: multiple dielectrics that contain **E** and **D** fields. We will look at two extreme cases: fields perpendicular to the dielectric interfaces and fields parallel to the dielectric interfaces. In this section we undertake the case where a parallel plate capacitor is completely filled two different lossy dielectrics complex dielectric constants $\epsilon_{\mathbf{1}}$ and $\epsilon_{\mathbf{2}}$ (Fig. 2.5). The dielectric interface will take place parallel to the **E** and **D** fields. Since each section of dielectric has the same voltage across it, these

two lossy capacitors are in parallel. Following a similar formalism as in section 2.5.1 we can describe each region as a capacitor shunted by a resistor. If we assume that for each dielectric there is a corresponding area, A_1 , A_2 then for the capacitors in region 1 and 2 we have:

$$C_1 = \epsilon_{1r}\frac{A_1}{d} \tag{2.31}$$

$$G_1 = \tan\delta_1 C_1\omega \tag{2.32}$$

$$C_2 = \epsilon_{2r}\frac{A_2}{d} \tag{2.33}$$

$$G_2 = \tan\delta_2 C_2\omega \tag{2.34}$$

These circuit elements are all in parallel and it is straight forward to calculate their total capacitance, C_{tot}, and total conductance, G_{tot}:

$$C_{tot} = C_1 + C_2 = \epsilon_{1r}\frac{A_1}{d} + \epsilon_{2r}\frac{A_2}{d} \tag{2.35}$$

$$G_{tot} = G_1 + G_2 = \tan\delta_1 C_1\omega + \tan\delta_2 C_2\omega \tag{2.36}$$

We can use equations 2.35 and 2.36 to write down the impedance for the circuit equivalent of a parallel plate capacitor filled with two different lossy dielectrics as:

$$Z_{cp} = G_{tot} + j\omega C_{tot} \tag{2.37}$$

Using the the total impedance, Z_{cp}, we can readily determine the quality factor:

$$\begin{aligned} \mathrm{Q}_{cp} &= \frac{\mathbf{Im}[Z_{cp}]}{\mathbf{Re}[Z_{cp}]} \\ \mathrm{Q}_{cp} &= \frac{C_{tot}}{\tan\delta_1 C_1 + \tan\delta_2 C_2} \end{aligned} \tag{2.38}$$

If we invert equation 2.38 we have:

$$\frac{1}{\mathrm{Q}_{cp}} = \frac{C_1}{C_{tot}}\tan\delta_1 + \frac{C_2}{C_{tot}}\tan\delta_2$$

$$\frac{1}{\mathrm{Q}_{cp}} = \frac{C_1}{C_{tot}}\frac{1}{Q_1} + \frac{C_2}{C_{tot}}\frac{1}{Q_2} \tag{2.39}$$

$$\frac{1}{\mathrm{Q}_{cp}} = \frac{p_1}{Q_1} + \frac{p_2}{Q_2} \tag{2.40}$$

Equations 2.39 and 2.40 define the capacitive participation ratio in the case where the field lines are parallel to the interface–explicitly $p_i = \frac{C_i}{C_{tot}}$. Conceptually we understand this participation ratio to be the electric field energy stored in the given region normalized by the entire electric field energy. The sum of all participation ratios multiplied by their respective loss rate results in the total loss rate of the resonance and is inverse to the total quality factor. We gain the intuition that if we must include lossy components then our circuit design should be such that the lossiest part has the smallest participation ratio, minimally spoiling the total quality factor.

For example, 3D resonators coupled to qubits with lifetimes of order 1 ms in the 5-10 GHz [50, 51, 52] regime give total quality factors in excess of 10^7. If we have a dielectric with a loss tangent of 10^{-5} in the quantum regime, then

no more than 1% of the total electric field energy can be stored in the lossy dielectric. Furthermore, we can also consider manipulations on the quantum state of a cavity that require conditional qubit rotations which take of order 1 μs [53, 54]. For qubit decay to be less than a percent during the cavity manipulation, qubit lifetimes must also be of order 100 μs leading to the conclusion that no more than 10% of the total electric field energy can be stored in a relatively low loss dielectric. The major point is that the physicist must carefully design the resonant circuit or artificial atom with participation ratios in mind so to minimally spoil the coherence of the quantum system.

2.5.3 Partially Filled Lossy Capacitor-Series

The other key case for a lossy capacitor is when it is filled with two different dielectrics $\epsilon_\mathbf{1}$ and $\epsilon_\mathbf{2}$ whose interfaces are perpendicular to the **E** and **D** field lines (Fig. 2.6). This partially filled capacitor can be modeled as two lossy capacitors in series. Each lossy capacitor's admittance is:

$$Y_{cs1} = j\omega C_1 + \omega C_1 \tan\delta_1 = G_1 + j\omega C_1 \tag{2.41}$$

$$Y_{cs2} = j\omega C_2 + \omega C_2 \tan\delta_2 = G_2 + j\omega C_2 \tag{2.42}$$

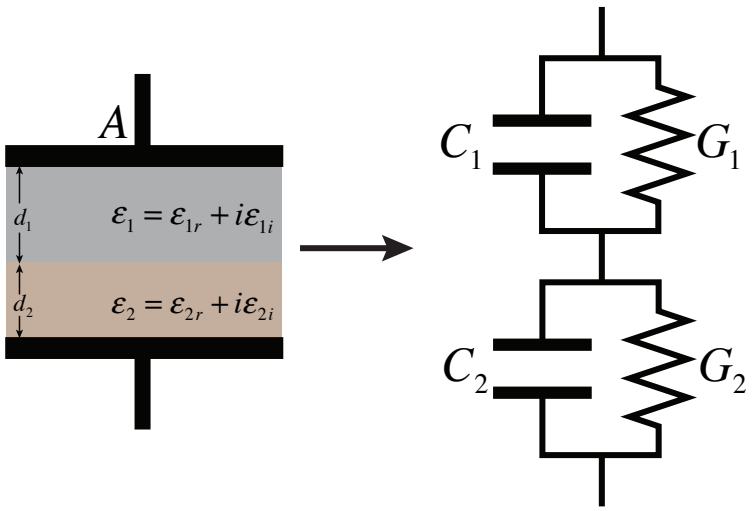

Figure 2.6: Lossy Capacitor-Partially Filled Series. To gain insight for how lossy dielectrics which are parallel to **E** or **D** fields contribute to the total quality factor, the above case of a parallel plate capacitor filled with two different complex dielectrics $\epsilon_{\mathbf{1,2}}$ is presented. The two different regions can be modeled as an idealized capacitor $C_{1,2}$ shunted by $G_{1,2}$ with each region circuit equivalent being in series with the other regions circuit equivalent.

Where $C_{1,2} = \epsilon_{1,2r}\frac{A}{d_{1,2}}$. We now combine these two series lossy capacitors to determine the total impedance, Z_{tot}:

$$\begin{aligned} Z_{tot} &= \frac{1}{Y_{cs1}} + \frac{1}{Y_{cs2}} \\ Z_{tot} &\approx \frac{C_2 \tan\delta_1 + C_1 \tan\delta_2 + j(C_1 + C_2)}{\omega C_1 C_2} \end{aligned} \tag{2.43}$$

We define $C_{tot} = \frac{C_1 C_2}{C_1 + C_2}$ so that we can now determine the total quality factor:

$$\begin{aligned} \frac{1}{\mathrm{Q}_{\ tots}} &= \frac{\mathbf{Re}[Z_{tot}]}{\mathbf{Im}[Z_{tot}]} \\ \frac{1}{\mathrm{Q}_{\ tots}} &= p_1 \tan\delta_1 + p_2 \tan\delta_2 \end{aligned} \tag{2.44}$$

We arrive at similar result again. The total quality factor will be set by the loss tangent of each item scaled by its participation ratio which in the case for field lines perpendicular to the interface is $p_i = \frac{C_{tot}}{C_i}$. If we use the parallel plate capacitor as an example and look at one of the participation ratios we have:

$$p_1 = \frac{C_{tot}}{C_1} = \frac{C_2}{C_1 + C_2} = \frac{\epsilon_{2r} A/d_2}{\epsilon_{1r} A/d_1 + \epsilon_{2r} A/d_2} = \left(1 + \frac{\epsilon_{1r}}{\epsilon_{2r}}\frac{d_2}{d_1}\right)^{-1} \tag{2.45}$$

As one would expect the participation ratio for a given layer increases with increasing relative thickness of the layer under investigation. A counter intuitive result is that by increasing the dielectric constant of a given layer actually reduces the participation ratio! In planar resonators a method that has been shown to increase the quality factor of the resonator is removing the dielectric near the edges, trenching [55, 56, 57]. A possible method to improve on trench-

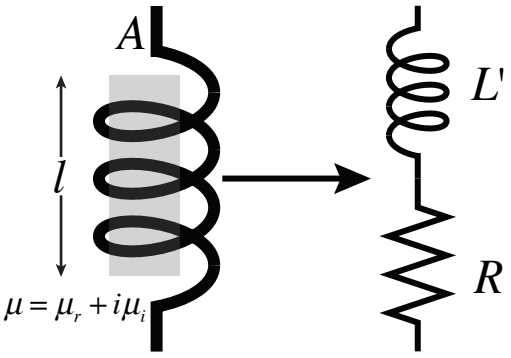

Figure 2.7: Lossy Inductor. To understand how lossy permeable material affect the quality factor of an inductor we will analyze the case of a solenoid of length l, cross sectional area A, complex permeability μ, and whose number of terms per unit length is n. This lossy solenoid will be described as an idealized inductor L' in series with a resistor R.

ing would be to use a material with a very large dielectric constant that can be thinly deposited underneath the resonator. This could allow for more aggressive trenching and structural support resulting in more energy stored in lossless vacuum. The idea of trenching could also prove useful for superconducting artificial atoms in the GHz frequency range, which unequivocally must be fabricated through lithographic processes and metal deposition in contrast to cavities which can be machined out of high purity superconductors.

2.5.4 Lossy Inductor

Up until this point all the discussion of participation ratios has been in terms of the **E** and **D** fields. However, we can and will produce analogous results for **B** and **H** fields. In a similar fashion to the lossy parallel plate capacitor we begin with a solenoid filled with a lossy material. The solenoid consists of n turns per

unit length, is filled with a lossy material with a complex permeability μ, has an cross sectional area A, and length l. The inductance for the lossy solenoid is:

$$L = \mu n^2 A l \tag{2.46}$$

Using equation 2.46 the impedance of a lossy solenoid is:

$$Z_{solenoid} = j\omega L = j\omega\mu n^2 A l = j\omega(\mu_r + i\mu_i)n^2 A l = \omega\mu_i n^2 A l + j\omega\mu_r n^2 A l = R + j\omega L' \tag{2.47}$$

From the solenoid impedance the quality factor can be calculated as:

$$\begin{aligned} \mathrm{Q}_{\ solenoid} &= \frac{\mathbf{Im}[Z_{solenoid}]}{\mathbf{Re}[Z_{solenoid}]} \\ \mathrm{Q}_{\ solenoid} &= \frac{\mu_r}{\mu_i} = \frac{1}{\tan\delta_l} \end{aligned} \tag{2.48}$$

Where in equation 2.48 we have defined an analogous loss tangent for permeable materials as $\tan\delta_l = \frac{\mu_i}{\mu_r}$. In the same manner as with the lossy capacitor, in the case of the lossy inductor its quality factor will be set by its inductive loss tangent.

2.5.5 Partially Filled Lossy Inductor-Series

Now we begin our treatment of inductors that have two different lossy permeable cores. In this section, we undertake the situation where the **B** and **H** fields are perpendicular to the surface interface of the two permeable materials

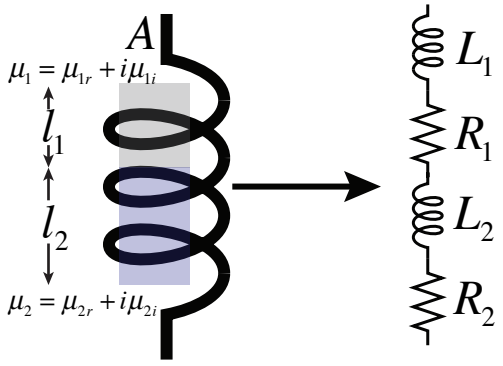

Figure 2.8: Lossy Inductor-Partially Filled Series. In the above, a solenoid is filled with two different permeable materials with complex permeabilities $\mu_{\mathbf{1,2}}$ whose interface is perpendicular to the **B** and **H** fields in the solenoid. By rewriting this as idealized inductors $L_{1,2}$ and resistors $R_{1,2}$ we gain insight as to how these permeable materials affect the total quality factor. It is also worth noting that the resistance we discuss here is non-ohmic and has zero DC resistance but nonzero resistance at RF frequencies.

(Fig. 2.8). The inductance for either region is:

$$L_{1,2} = \mu_{r\ 1,2} n^2 A l_{1,2} \tag{2.49}$$

We can also use equation 2.49 to readily write down the resistance in either region as:

$$R_{1,2} = \omega \tan \delta_{l\ 1,2} L_{1,2} \tag{2.50}$$

Using equations 2.49, 2.50, and that these idealized circuit elements are in series the total inductance and resistance are:

$$L_{tot} = n^2 A(\mu_{r\ 1} l_1 + \mu_{r\ 2} l_2) \tag{2.51}$$

$$R_{tot} = \omega n^2 A(\tan \delta_{l\ 1} \mu_{r\ 1} l_1 + \tan \delta_{l\ 2} \mu_{r\ 2} l_2) \tag{2.52}$$

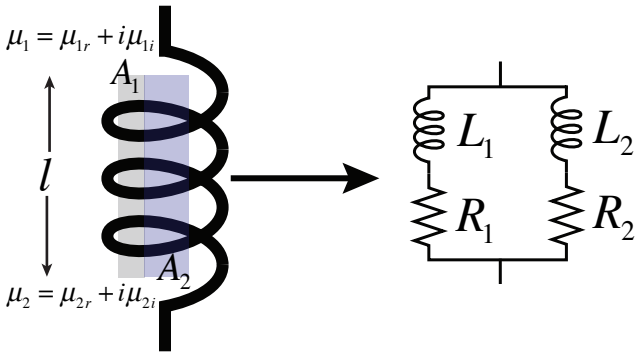

Figure 2.9: Lossy Inductor-Partially Filled Series. In the above, a solenoid is filled with two different permeable materials with complex permeabilities $\mu_{\mathbf{1,2}}$ whose interface is parallel to the **B** and **H** fields in the solenoid. By rewriting this as idealized inductors $L_{1,2}$ and resistors $R_{1,2}$ we gain insight as to how these permeable materials affect the total quality factor.

From equations 2.51 and 2.52 the quality factor of the lossy solenoid is:

$$\begin{aligned} \frac{1}{\mathrm{Q}_{\ tots}} &= \frac{\mathbf{Re}[Z_{tot}]}{\mathbf{Im}[Z_{tot}]} \\ \frac{1}{\mathrm{Q}_{\ tots}} &= p_1 \tan\delta_{l\ 1} + p_2 \tan\delta_{l\ 2} \end{aligned} \tag{2.53}$$

Where we have defined the participation ratios for the **B** and **H** fields when the permeable materials are in series as $p_i = \mu_{r\ i} l_i / (\Sigma \mu_{r\ j} l_j)$. As expected the sections with longest length and highest permeability contribute most to the total quality factor.

2.5.6 Partially Filled Lossy Inductor-Parallel

In this final section, we under take the case that a solenoid is entirely filled with permeable material but that the interface between two distinct regions is per-

pendicular to the **B** and **H** fields (Fig. 2.9). Each section will have an inductance and resistance of:

$$L_{1,2} = \mu_{r\ 1,2} n^2 A_{1,2} l \tag{2.54}$$

$$R_{1,2} = \omega \tan \delta_{1,2} L_{1,2} \tag{2.55}$$

The impedance for either region can be written as:

$$Z_{1,2} = R_{1,2} + j\omega L_{1,2} \tag{2.56}$$

Since these two regions are in parallel we combine them to find their total impedance:

$$\begin{aligned} Z_{net} &= \frac{Z_1 Z_2}{Z_1 + Z_2} \\ Z_{net} &\approx \frac{\omega^2 L_1^2 R_2 + \omega^2 L_2^2 R_1 + j\omega^3 L_1 L_2 (L_1 + L_2)}{\omega^2 (L_1 + L_2)^2} \end{aligned} \tag{2.57}$$

Now to determine the quality factor of this solenoid we again take the ratio of the imaginary part of the net impedance to the real part:

$$\begin{aligned} \frac{1}{\mathrm{Q}_{\ totp}} &= \frac{\mathbf{Re}[Z_{tot}]}{\mathbf{Im}[Z_{tot}]} \\ \frac{1}{\mathrm{Q}_{\ totp}} &= p_2 \tan \delta_{l\ 2} + p_1 \tan \delta_{l\ 1} \end{aligned} \tag{2.58}$$

Where we have used that the total inductance is $L_{tot} = \frac{L_1 L_2}{L_1 + L_2}$. We use the total inductance to define the participation ratio for each element as $p_i = \frac{L_{tot}}{L_i}$.

In the case of a solenoid we can find the participation ratio to be:

$$\begin{aligned} p_1 &= \frac{L_{tot}}{L_1} \\ p_1 &= \left(\frac{\mu_{r\ 1}}{\mu_{r\ 2}}\frac{A_1}{A_2}+1\right)^{-1} \end{aligned} \tag{2.59}$$

From this we find two surprising results. That the participation ratio increases for smaller areas and for smaller permeabilities! Once again we find a scenario where a small bit of vacuum could substantially improve the quality factor of a resonator. It is not too surprising that this case would be the one with a beneficial outcome since an electromagnetic wave in free space has the electric and magnetic fields perpendicular to each other. From the results of section 2.5.3 for the electric field participation ratios we could have naively guessed that the orthogonal magnetic field would scale similarly; however, it is quite nice that it did work out to be the case.

2.6 Final Thoughts

The major ideas we have developed in this chapter, quality factors and participation ratios, will be used extensively in the next two chapters which are on the physical implementation of microwave cavities and resonators. Quality factors give a frequency independent way to quantify the loss of a resonant mode. Although two cavities or qubits could have the same quality factor for their resonance those with lower frequencies have longer lifetimes from equation 2.12. Also, participation ratios give a means to quantify resonances with similar qual-

ity factors by being able to break down the contributing loss mechanisms to see if results are consistent or inconsistent.

3

Transmission Line Resonators

The main goal of this chapter is to describe and adapt a microwave geometry for circuit quantum electrodynamics. Cavities with lifetimes in excess of 1 ms in the quantum regime [58, 50, 51, 52] can be constructed from bulk superconductors materials. However, to access the rich physics of cQED it is necessary to have an atomic like object [59]. In cQED the atomic like object relies originates

from the Josephson junction. Incorporating a Josephson junction to realize resonances in the 5-10 GHz range requires fabrication with lithography and deposition making fabrication nano-fabrication an essential part of cQED. Thoughtful integration is required to build more complex structures while maintaing the coherence found in waveguide cavities. To fulfill this demand, we seek to implement a novel, lithographically defined transmission line geometry. As we will see, the transmission line structure can realize a resonant cavity. This resonant cavity in principle can be used for: state readout of the 'artificial atom', protecting the 'artificial atom' from radiating into the environment, and serving as a test bed for different superconducting materials, dielectrics, and lithographic procedures.

3.1 Historical Development

Microwave circuits are by no means a new development as their use date back to the 1930s. Although waveguide structures were quite successful in the 1940s, the desire for an increased bandwidth as well as complexity and integration spurred the development of two new geometries: stripline and microstrip [60] (Fig. 3.1). The invention of the stripline architecture is credited to Robert M. Barrett in the 1950s at the Air Force Cambridge Research Center [60]. The original development by Barrett used dielectric materials only to support the center conductor between the two ground planes (Fig. 3.1 **C**). Although now any structure with a flat conductor between two ground planes is referred to as a stripline, in the 1950s if the device was mostly filled by vacuum then it was

called a stripline and if the device was filled entirely with a dielectric material it was referred to as "tri-plate" (Fig. 3.1 **B**). Striplines were an attractive geometry for microwave engineers in part because it is a TEM structure with no cut off frequency. At the same time the stripline was being developed so too was the microstrip geometry (Fig. 3.1 **A**). The microstrip relies on the fields being concentrated between the center conductor and a sole ground plane. Issues with the microstrip geometry are radiative losses as well as a greatly distorted phase velocity due to the large difference in dielectrics. For improved performance microstrips typically need an enclosure and for this reason we elect to develop a stripline structure.

3.2 Characteristic Impedance

Figure 3.2 shows the prototypical stripline. The ground planes are separated by a distance, H, filled with a dielectric with relative dielectric ϵ_r, and with the center conductor placed symmetrically between the ground planes. The center conductor has a width, W, and thickness, t. Since there are two conductors this is a TEM structure [48]. Closed form solutions to the characteristic impedance, Z_c, of this transmission line exist [61]; however, a more simplified form that does not deviate by more than 1% [48] of the true value is:

$$Z_c = \frac{60}{\sqrt{\epsilon_r}} \ln\left(\frac{4H}{.67\pi W(.8 + \frac{t}{W})}\right) \tag{3.1}$$

In our particular case the thickness will be 200 nm or less and the widths will

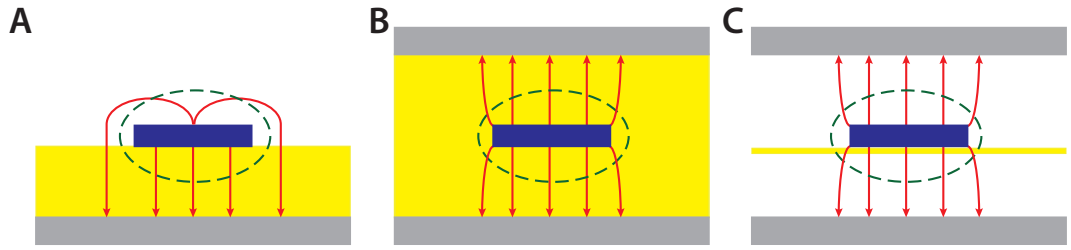

Figure 3.1: In all sketches, a conducting strip (blue) is deposited on a substrate (yellow) and then kept a distance away from another conductor, ground, (grey). In all cases, electric field lines are drawn in red and magnetic field lines are drawn as green dashed lines. **A** a cartoon figure of a microstrip geometry which has only one ground plane and is quasi-TEM transmission line [48]. **B** A cartoon schematic of a tri-plate structure which is a center conductor fully surrounded by a dielectric substrate with a top and bottom ground plane. **C** A cartoon schematic of the original stripline design where the center conductor is deposited on a substrate only thick enough to provide mechanical support and is mostly vacuum (air). As we saw in chapter 2, the electric field energy density will be greater in the region with the lower dielectric constant if the electric field is perpendicular at the interface so in the original stripline design the majority of the electric field energy will reside in vacuum (air). The substrate sits between two conducting ground planes and is a TEM transmission line [48]. All sketches of microstrip, tri-plate, and striplines with electric and magnetic fields based on Ref. [60].

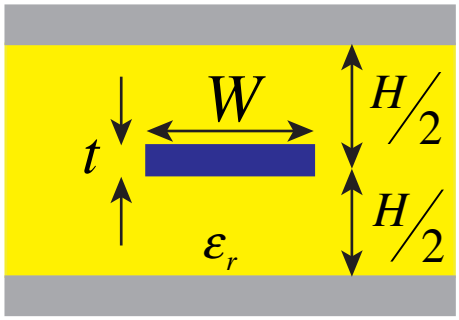

Figure 3.2: Prototypical stripline. The ground planes (grey) are separated by a distance, H, filled with a dielectric with relative dielectric ϵ_r (yellow), and with the center conductor (blue) placed symmetrically between the ground planes. The center conductor has a width, W, and thickness, t.

be 300 microns or more so we can neglect the $\frac{t}{W}$ contribution and simplify eq. 3.1 to:

$$Z_c = \frac{60}{\sqrt{\epsilon_r}} \ln\left(\frac{4H}{.54\pi W}\right) \tag{3.2}$$

We can use the above to gain some intuition as to the relative sizes our physical structure requires. For this structure to have a characteristic impedance of 50 Ω, assuming $\epsilon_r = 10$, the height to width ratio is roughly a factor of 5. In this thesis, a height to width ratio of 3 was used. The smaller height to width ratio is a consequence of the dielectric being roughly half vacuum.

3.3 Design Consideration

In this section, we undertake the design of a stripline structure that will be readily compatible with the standard cQED environment. We seek to minimize fabrication steps required and elect to construct the grounding structure out of

bulk superconductor so different chips can be readily swapped in and out. The thought process was to minimize the ambiguity in future results that depend on complicated fabrication and deposition procedures. A substrate inserted into the superconducting structure will have a deposited thin film which acts as the center pin for the stripline structure. By having a finite length of the center conductor we can realize a half wave length resonator with respect to the voltage on the center pin.

Since we will be building an enclosed stripline to minimize radiative and environmental losses we must acknowledge that the enclosure is really a rectangular waveguide. We will design this rectangular waveguide to have a high cutoff frequency (> 20 GHz) to avoid any extraneous modes coupling to our superconducting structures. The cutoff frequency, $f_{c,mn}$, of the rectangular waveguide, with sides of length a and b, is [48]:

$$f_{c,mn} = \frac{c}{2\pi\sqrt{\mu_r \epsilon_r}} \sqrt{\left(\frac{m\pi}{a}\right)^2 + \left(\frac{n\pi}{b}\right)^2} \tag{3.3}$$

In equation 3.3, c is the speed of light in vacuum, μ_r and ϵ_r are the relative permeability and permitivity respectfully, and m, n are the different transverse mode indices. Rectangular waveguides are analyzed as a single conductor and consequently cannot support TEM wave propagation. For this reason, the rectangular waveguide can only support $\mathrm{TE_{mn}}$ or $\mathrm{TM_{mn}}$ modes. Equation 3.3 gives the cut off frequency for either $\mathrm{TE_{mn}}$ or $\mathrm{TM_{mn}}$ modes. In our design we care only about the frequency that the first mode of the structure that propagates rather than higher modes. The lowest mode will be the $\mathrm{TE_{10}}$ defined by the

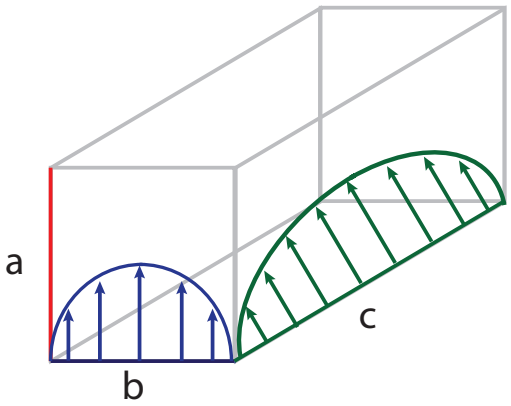

Figure 3.3: Rectangular Waveguide Cavity. A rectangular waveguide with dimensions **a** (red), **b** (blue), and **c** (green). Shown in blue and green arrows are the amplitude of the electric field along either the $\hat{\mathbf{b}}$, $\hat{\mathbf{c}}$ directions which due to boundary conditions must be zero at the walls of the rectangular waveguide cavity.

longest side of the rectangle [48]:

$$f_{c,10} = \frac{c}{2a\sqrt{\mu_r \epsilon_r}} \tag{3.4}$$

The longest length that can be tolerated for a cutoff frequency of 20 GHz is roughly 5mm assuming that the waveguide is fully filled with a relative dielectric of 10. Decreasing the relative dielectric will increase the cutoff frequency and consequently increase the relevant length scale.

A similar consideration to investigate is the consequence of having a finite length rectangular waveguide. The sample box itself is rectangular (figure 3.3),

with sides a, b, and c, and will have resonance frequencies given by [48]:

$$f_{mnl} = \frac{c}{2\pi\sqrt{\mu_r \epsilon_r}} \sqrt{\left(\frac{m\pi}{a}\right)^2 + \left(\frac{n\pi}{b}\right)^2 + \left(\frac{l\pi}{c}\right)^2} \tag{3.5}$$

In equation 3.5 c is the speed of light in vacuum, μ_r and ϵ_r are the relative permeability and permitivity respectfully, and m, n are the different transverse mode indices and l is the longitudinal index. Once again the dominant mode, lowest frequency, will be the TE_{101}. This assumes that $c > a > b$ which means that the external conductor will be longer than either of the sides making up the cross-sectional rectangle. From equation 3.5 we gain the insight that the longer we make the structure the less it depends on the length. For a TE_{101} mode, in the limit that $c \gg a$ equation 3.5 reduces to equation 3.4 but has the interpretation of being a resonance frequency rather than the cutoff frequency.

3.4 First Design

In the first design we choose the width of our rectangular cross section to be 1.2 mm, the height to be 1mm, and the length of the structure to be 25mm. If the structure were entirely filled with $\epsilon_r = 10$ then the cutoff frequency from equation 3.4 is 40 GHz. If the relative dielectric is smaller than that only increases the cutoff frequency. The resonant mode of this holder will also be approximately 40 GHz because of the extreme length to width ratio.

Figure 3.10a, b contain diagrams with cross sections of the enclosed stripline that will be the focus of this chapter. We have chosen to have a very narrow

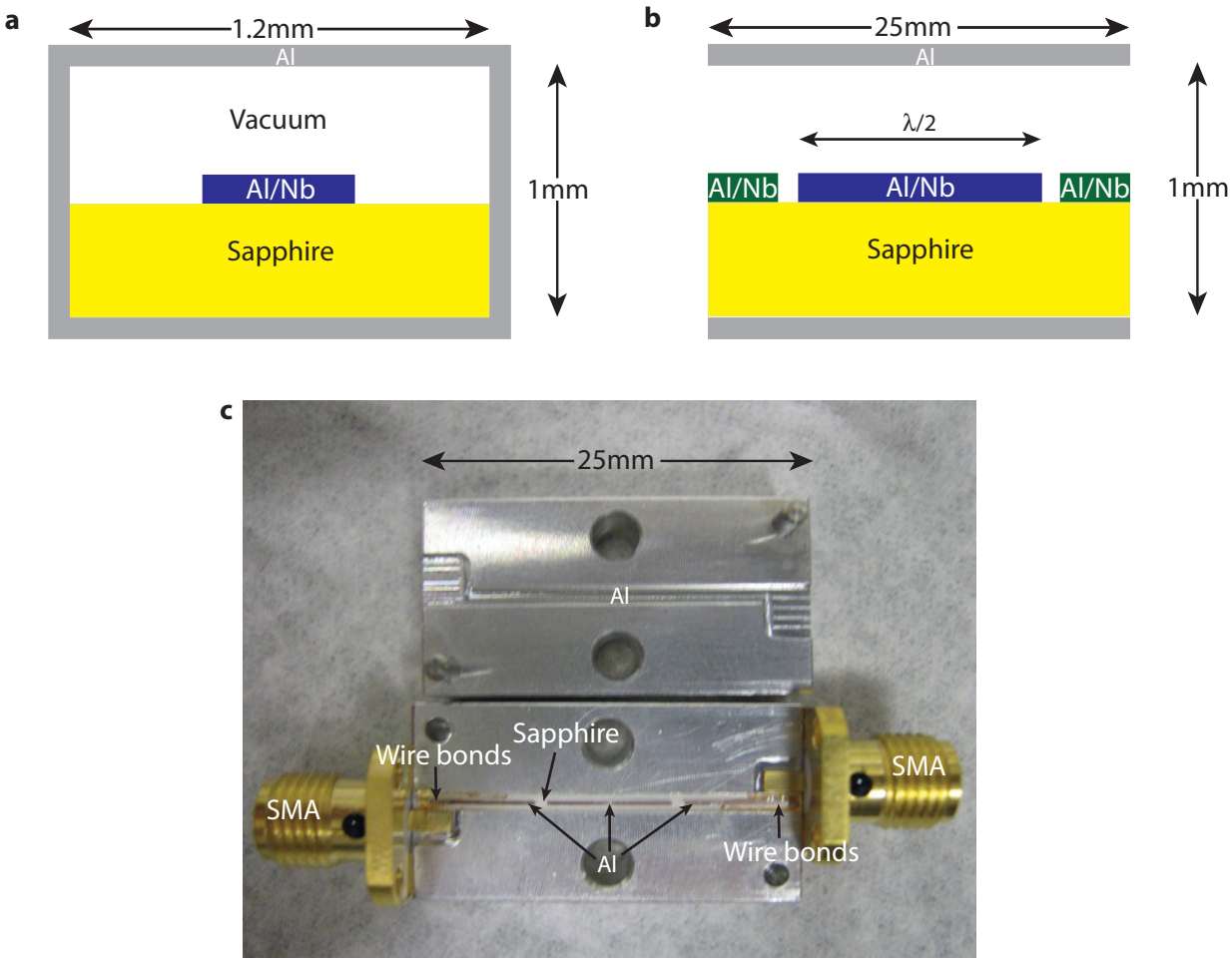

Figure 3.4: First generation stripline design. a) Cross section of design. In grey is the outer conductor whose internal dimensions are 1 mm by 1.2 mm. In yellow is the substrate for the deposited film (blue). The substrate primarily used is sapphire; however, any dielectric can be used. This structure is flexible enough to accommodate many different dielectrics and conductors to measure their loss. b) Side cut lengthwise down holder. In grey is the outer conductor whose total length is 25 mm and height is 1mm. In yellow is the dielectric material with deposited superconducting material (blue and green). Although different colors are used the superconducting material is the same. In green are the superconducting leads which are gap coupled to the superconducting half wave length resonator, blue. c) Photo of actual sample. The external structure has two symmetric halves that close into each other. One half has the sapphire substrate with the deposited superconductor. SMA connectors are wire-bonded to the superconducting leads to allow measurement of the resonator.

structure to force all undesired modes to be quite high in frequency. All though most of the discussion up until this point has discussed the stripline with a uniformly filled dielectric we have elected to only partially fill the structure. The main reason for this decision is for frequency stability. In preliminary tests it was found that adding in dielectric on top would cause fluctuations in the frequency of the resonator. As we will see later even with half filled dielectric it accounts for roughly 90% of the electric participation ratio so adding dielectric on top was an unnecessary complication in the early development.

3.5 Participation Ratios

In this section we undertake analytically calculating participation ratios for both the surface loss of a lossy dielectric and the bulk loss of a dielectric in a stripline geometry. To achieve these calculations one must make some approximations that are not exact in real experiments. The goal with these analytical calculations is not to accurately calculate participation ratios to arbitrary precision but rather to give the experimentalist intuition for the order of magnitude of loss and what to expect when a given geometry is changed.

To accurately calculate a participation ratio is is essential for one to use a finite elemental solver. The software of choice in this thesis is Ansys' HFSS (High Frequency Structural Simulator). HFSS allows one to draw all structures in a CAD environment and solve for the scattering, impedance, or admittance matrices. HFSS partitions the drawn structure into many small tetrahedrals and solves Maxwell's equations inside each tetrahedral. Since HFSS solves for the

electric and magnetic fields it is relatively straight forward to use their fields calculator to sum the electric or magnetic field energy in a given region or volume. One can setup the field calculation ahead of time to calculate a participation ratio and then use the participation ratio as the numerical quantity that is used to determine whether or not a solution converged. Additionally, HFSS can be used to simulate Hamiltonian parameters which is discussed in chapter 4.

3.5.1 Surface Dielectric Loss

We now undertake calculating dielectric losses to know how loss will determine our quality factors as well as give insight into which knobs we have available to change as an experimental parameter. First we will calculate the loss from dielectric surfaces. The total energy per unit length stored in the electric field of a stripline of length L, with capacitance per unit length, c, and voltage, V, is:

$$\frac{U_{tot}}{L} = \frac{1}{2}cV^2 \tag{3.6}$$

To calculate the energy per unit length stored in the lossy dielectric of thickness t and length L we must calculate the following integral:

$$U_{surf} = \frac{1}{2}Lt \int \epsilon |E_{surf}|^2 \mathbf{dw} \tag{3.7}$$

To evaluate equation 3.7 we must determine E_{surf}. Assuming a uniform charge

per unit area, σ, on the center conductor the electric field is:

$$E_{surf} = \frac{\sigma}{\epsilon_0 \epsilon_r} \tag{3.8}$$

We can rewrite E_{surf} in terms of the total charge, Q, and the length, L, and width, W, of the center conductor equation 3.8 becomes:

$$E_{surf} = \frac{\sigma}{\epsilon_0 \epsilon_r} = \frac{Q}{LW\epsilon_0 \epsilon_r} \tag{3.9}$$

We can rewrite equation 3.9 by using the capacitance relation between the charge per unit length, the capacitance per unit length, and the voltage:

$$\frac{Q}{L} = cV \tag{3.10}$$

With equations 3.9 and 3.10 we can find the surface electric field is:

$$E_{surf} = \frac{cV}{W\epsilon_0 \epsilon_r} \tag{3.11}$$

Using equation 3.11 in equation 3.7 we can determine the energy per unit length stored in the lossy surface dielectric:

$$\begin{aligned} U_{surf} &= \frac{1}{2} Lt \int \epsilon |E_{surf}|^2 \mathbf{dW} \\ U_{surf} &= \frac{1}{2} LtW\epsilon_0 \epsilon_r \left(\frac{cV}{W\epsilon_0 \epsilon_r} \right)^2 \\ \frac{U_{surf}}{L} &= \frac{1}{2} \frac{t}{W\epsilon_0 \epsilon_r} (cV)^2 \end{aligned}$$

We can now calculate the participation ratio for a lossy surface dielectric for the stripline using equations 3.6 and 3.10 is:

$$\begin{aligned} p_{surf} &= \left(\frac{U_{surf}}{L}\right)\left(\frac{U_{tot}}{L}\right)^{-1} \\ p_{surf} &= \left(\frac{1}{2}\frac{t}{W\epsilon_0\epsilon_r}(cV)^2\right)\left(\frac{1}{2}cV^2\right)^{-1} \\ p_{surf} &= \frac{tc}{W\epsilon_0\epsilon_r} \end{aligned}$$

We find that the surface participation ratio is dependent mostly on well defined quantities such as the thickness of the lossy dielectric, t, its width, w, and the relative dielectric constant, ϵ_r. The only unknown quantity we need to determine is the capacitance per unit length, c. We remember that for a transmission line its characteristic impedance in terms of its inductance per unit length l and capacitance per unit length c is:

$$Z_c = \sqrt{\frac{l}{c}} \tag{3.12}$$

Also, the speed of light in the transmission line is:

$$v = \frac{1}{\sqrt{lc}} \tag{3.13}$$

Using equations 3.12 and 3.13 we can solve for the capacitance per unit length as:

$$c = \frac{1}{Z_c v} \tag{3.14}$$

Now we can rewrite the surface participation ratio using equation 3.14 as:

$$p_{surf} = \frac{t}{W\epsilon_0\epsilon_r Z_c v} \tag{3.15}$$

We can further simplify this by using that velocity of light in the transmission line in terms of the speed of light $\mathbf{c}$ and the relative dielectric constant ϵ_r is $v = \frac{\mathbf{c}}{\sqrt{\epsilon_r}}$:

$$p_{surf} = \frac{t}{W\epsilon_0\sqrt{\epsilon_r} Z_c \mathbf{c}} \tag{3.16}$$

Plotted in figure 3.5 is equation 3.16 as a function of center trace width for realistic parameters. As an example, we can use equation 3.16 for a typical stripline geometry. For a lossy surface layer with thickness of 3 nm, a center conductor width of 300 μm, relative dielectric of 6, and $Z_c = 50\ \Omega$ from equation 3.2, we get a surface participation ratio of order $\sim 10^{-5}$. From this we learn that to have a total quality factor in excess of a million the lossy surface layer need only have a quality factor of ten. However, at the writing of this thesis the state of the art cavity lifetime when coupled to a qubit is of order 1 ms which if realized in a stripline geometry requires the lossy layer to have a quality factor no worse than a few hundred.

3.5.2 Bulk Dielectric Loss

The bulk dielectric loss will be a more straight forward calculation than the surface dielectric loss. We assume that the center conductor is symmetrically placed between the ground planes. To determine the energy stored in the dielec-

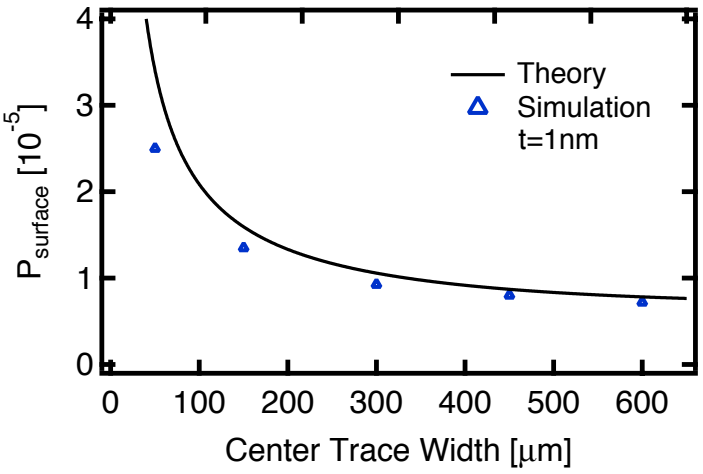

Figure 3.5: Center Conductor Surface Participation Ratio. Plotted as a function of the width of the center conductor of the stripline structure is the surface participation ratio for dielectric losses. In solid black is the theoretical predictions from equation 3.16 where the lossy layer has been assumed to be 1 nm, a relative dielectric of 6, and the characteristic impedance is calculated from equation 3.2. In blue triangles are the results from HFSS simulations at different center widths. In HFSS one can specifically calculate the ratio of electric field integrals and then multiplying that ratio by the assumed thickness one readily has the dielectric surface participation ratio. For smaller widths such as 50 μm and 100 μm the HFSS simulation does not converge. Explicitly this means that the simulation computer does not have enough RAM to store the meshing necessary to properly evaluate the electric field integral. This is a common issue when there are extreme aspect ratios. For larger widths the simulation does converge giving us confidence that the analytical value and the simulation roughly agree.

tric substrate we need only compare the energy stored in the dielectric to the total energy stored. Therefore the electric field energy stored in the dielectric is:

$$U_{bulk} = \frac{1}{2}\int \epsilon_0\epsilon_r |E|^2 \mathbf{dV} \tag{3.17}$$

The energy stored in vacuum will be:

$$U_{vac} = \frac{1}{2}\int \epsilon_0 |E|^2 \mathbf{dV} \tag{3.18}$$

The bulk participation ratio p_E is then:

$$\begin{aligned} p_E &= \frac{U_{bulk}}{U_{vac} + U_{bulk}} \\ p_E &= \frac{\frac{1}{2}\int \epsilon_0\epsilon_r |E|^2 \mathbf{dV}}{\frac{1}{2}\int \epsilon_0 |E|^2 \mathbf{dV} + \frac{1}{2}\int \epsilon_0\epsilon_r |E|^2 \mathbf{dV}} \\ p_E &= \frac{\epsilon_r}{1+\epsilon_r} \end{aligned} \tag{3.19}$$

For sapphire we can take $\epsilon_r = 10$ and then $p_E = .91$ which agrees with an HFSS simulation giving the bulk dielectric participation ratio as $p_E = .92$.

3.5.3 Inductive losses and Kinetic Inductance Ratio

To calculate the kinetic inductance ratio, α, between the center pin and the total geometric inductance we begin with the reactance associated with the kinetic inductance of a superconductor with uniform current density:

$$\mathrm{X}_k = \omega\mu_0\lambda_0 = \omega L_k \tag{3.20}$$

In equation 3.20, ω is frequency, μ_0 is the free space permeability, and λ_0 is the London penetration depth of the superconductor, and we have defined the product $\mu_0\lambda_0$ as the kinetic inductance, L_k. We now say that the superconducting strip has a width, w, which we divide by to get the kinetic inductance per unit length:

$$l_k = \frac{L_k}{w} = \frac{\mu_0\lambda_0}{w} \tag{3.21}$$

Now the kinetic inductance ratio can be formally defined in terms of the kinetic inductance per unit length, l_k, and the geometric inductance per unit length, l_g, as:

$$\alpha = \frac{l_k}{l_g} \tag{3.22}$$

To determine l_g we use the characteristic impedance of the transmission line its propagation velocity $v = \dfrac{1}{\sqrt{l_g c_g}}$.

$$\begin{aligned} Z_0 &= \sqrt{\frac{l_g}{c_g}} \\ l_g &= \frac{Z_0\sqrt{\epsilon_r}}{c} \end{aligned} \tag{3.23}$$

Using equations 3.21 and 3.23 in equation 3.22 yields:

$$\alpha_{sl} = \frac{l_k}{l_g} = \frac{\mu_0\lambda_0 c}{wZ_0\sqrt{\epsilon_r}} \tag{3.24}$$

Equation 3.24 depends mostly on fundamental or materials properties and the only external knob we have as an experimentalist is the width of the center

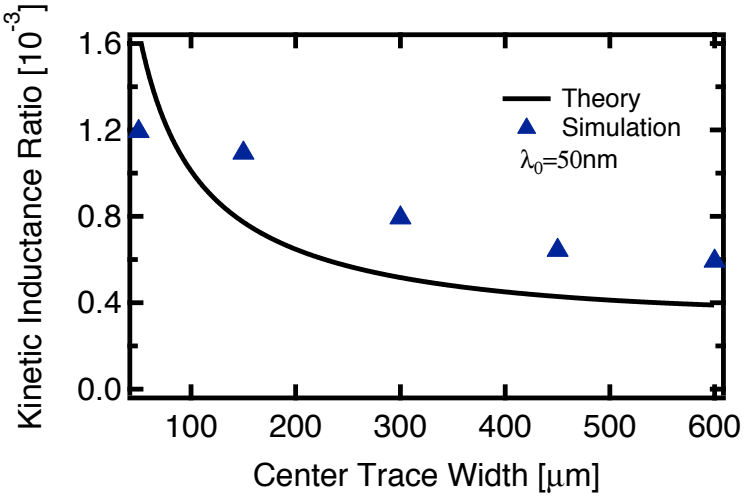

Figure 3.6: Kinetic Inductance Calculation. Kinetic inductance ratio is plotted as a function of the center conductor width of the stripline. The solid line is equation 3.24 with $\lambda_0 = 50$nm, $\epsilon_r = 6$, and Z_0 calculated from equation 3.2. In blue triangles are the results from HFSS simulations done where the magnetic field integrals are specifically evaluated. This once again gives the benefit of only needing to scale the simulation result by the London penetration length. As in figure 3.5, for smaller widths the simulation is unable to converge on a value. An additional discrepancy is that for equation 3.24 a uniform current distribution is assumed whereas in simulation a non-uniform current distribution is observed. Regardless, both simulation and analytical values are still within a factor of two so our intuition and order of magnitude estimate are correct.

trace. Although the characteristic impedance will also change dependent on the width of the center strip as in equation 3.2 the dependence is weak (logarithmic). Plotted in figure 3.6 is a plot of the kinetic inductance fraction for realistic values of the stripline structure.

3.6 Evanescent Coupling

In this section we will describe the coupling between stripline structures under the umbrella of evanescent coupling. The conceptual idea is that we will send a wave at a barrier that does not allow propagation at the intended frequency; however, on the other side of the barrier is another region where the wave can propagate. It has long been known for electromagnetic waves that evanescent coupling is possible and is well described by Feynman [49]. Evanescent coupling has been successfully leveraged for measurements in the quantum regime with 3D cavities [58, 62, 63, 64]. In the case of the stripline we will have the scenario where the incoming signal is propagating down the transmission line structure, it will then encounter a rectangular cavity with a signal frequency below the cutoff of the wave guide exponentially reflecting the signal based on the length of the waveguide. Finally, the signal in the waveguide below cutoff is met with a half wavelength resonator formed in the stripline. At each boundary the overlap between the electric and magnetic fields of the different modes will determine which modes participate and control the coupling. Although closed form solutions do not exist for TEM wave propagating down the stripline, from the field lines in 3.1 we can approximate the transverse electric and magnetic fields as

[65]:

$$E_{x,TEM}(x,y,z) = -E_{0x}\cos\left(\frac{\pi x}{a}\right)\sin\left(\frac{\pi y}{b}\right)e^{\,j(\beta z-\omega t)} \quad (3.25)$$

$$E_{y,TEM}(x,y,z) = -E_{0y}\sin\left(\frac{\pi x}{a}\right)\cos\left(\frac{\pi y}{b}\right)e^{\,j(\beta z-\omega t)} \quad (3.26)$$

$$H_{x,TEM}(x,y,z) = H_{0x}\sin\left(\frac{\pi x}{a}\right)\cos\left(\frac{\pi y}{b}\right)e^{\,j(\beta z-\omega t)} \quad (3.27)$$

$$H_{y,TEM}(x,y,z) = -H_{0y}\cos\left(\frac{\pi x}{a}\right)\sin\left(\frac{\pi y}{b}\right)e^{\,j(\beta z-\omega t)} \quad (3.28)$$

Since this is a TEM structure the propagation constant, β, is equal to the wave number–explicitly, $\beta = k = \frac{2\pi}{\lambda}$. We must determine the overlap between this mode and the possible modes of the rectangular waveguide which cannot support TEM waves but can support either transverse electric, TE_{mn}, or transverse magnetic, TM_{mn}, modes. The TE_{mn} modes are [48]:

$$E_{x,TE}(x,y,z) = \frac{j\omega\mu n\pi}{k_c^2 b}A_{mn}\cos\left(\frac{m\pi x}{a}\right)\sin\left(\frac{n\pi y}{b}\right)e^{\,j(\beta z-\omega t)} \quad (3.29)$$

$$E_{y,TE}(x,y,z) = -\frac{j\omega\mu n\pi}{k_c^2 a}A_{mn}\sin\left(\frac{m\pi x}{a}\right)\cos\left(\frac{n\pi y}{b}\right)e^{\,j(\beta z-\omega t)} \quad (3.30)$$

$$H_{x,TE}(x,y,z) = \frac{j\beta m\pi}{k_c^2 a}A_{mn}\sin\left(\frac{m\pi x}{a}\right)\cos\left(\frac{n\pi y}{b}\right)e^{\,j(\beta z-\omega t)} \quad (3.31)$$

$$H_{y,TE}(x,y,z) = \frac{j\beta m\pi}{k_c^2 b}A_{mn}\cos\left(\frac{m\pi x}{a}\right)\sin\left(\frac{n\pi y}{b}\right)e^{\,j(\beta z-\omega t)} \quad (3.32)$$

Likewise the TM_{mn} modes of the rectangular waveguide are [48]:

$$E_{x,TM}(x,y,z) = -\frac{j\beta m\pi}{k_c^2 a} B_{mn} \cos\left(\frac{m\pi x}{a}\right) \sin\left(\frac{n\pi y}{b}\right) e^{\,j(\beta z-\omega t)} \quad (3.33)$$

$$E_{y,TM}(x,y,z) = -\frac{j\beta n\pi}{k_c^2 b} B_{mn} \sin\left(\frac{m\pi x}{a}\right) \cos\left(\frac{n\pi y}{b}\right) e^{\,j(\beta z-\omega t)} \quad (3.34)$$

$$H_{x,TM}(x,y,z) = \frac{j\omega\epsilon m\pi}{k_c^2 b} B_{mn} \sin\left(\frac{m\pi x}{a}\right) \cos\left(\frac{n\pi y}{b}\right) e^{\,j(\beta z-\omega t)} \quad (3.35)$$

$$H_{y,TM}(x,y,z) = -\frac{j\omega\epsilon m\pi}{k_c^2 a} B_{mn} \cos\left(\frac{m\pi x}{a}\right) \sin\left(\frac{n\pi y}{b}\right) e^{\,j(\beta z-\omega t)} \quad (3.36)$$

The propagation constant in the waveguide will be determined by the wave number k and the cutoff wave number k_c. Explicitly:

$$\beta = \sqrt{k^2 - k_c^2} \quad (3.37)$$

If $k < k_c$ we get some neat physics. The propagation constant becomes imaginary and instead of a propagating wave an exponentially reflected wave is the solution in the given region. From equation 3.37 we see that higher cutoff wave numbers, higher frequencies, will reflect more of the signal. This means we are concerned most with the first rectangular waveguide mode that has a nonzero overlap with the incoming TEM wave because that will be the dominant transfer of electromagnetic waves. By computing the overlap:

$$O = \int_0^a \int_0^b E_{TEM} \cdot E_{TE/TM} \mathbf{dxdy} \quad (3.38)$$

The first nonzero overlap from equation 3.38 is the TM_{11} mode. Due to the very tight dimensions of the stripline we expect the TM_{11} mode to account for the vast majority of the transferred signal due to the very high cutoff frequency of the rectangular waveguide. The last part we need to check is that the TM_{11} has a nonzero overlap with the standing wave of the stripline. The approximated fields at the end of the stripline half wavelength resonator are:

$$E_{x,hw}(x,y,z) = 0 \tag{3.39}$$

$$E_{y,hw}(x,y,z) = E_{0y}\Theta(y-\frac{b}{2})\cos\left(\frac{(2m+1)\pi}{L}z\right)e^{\ -j\omega t} \tag{3.40}$$

$$H_{x,hw}(x,y,z) = H_{y,hw}(x,y,z) = 0 \tag{3.41}$$

In the above, $\Theta(y-\frac{b}{2})$ is the Heaviside unit step function. This means that at $t=0$ the electric field exists only above the center conductor and not below it. Fortuitously the overlap is nonzero between the TM_{11} mode and the end of the stripline. This means that we expect the transmitted power into and out of the stripline resonator will exponentially depend on the length of rectangular wave guide. Explicitly, the coupling quality factor, Q_c will be:

$$Q_c \propto e^{2\beta z} \tag{3.42}$$

From equation 3.42 we have an amazingly simple relation for the coupling quality factor to a half wavelength stripline resonator which is plotted in figure 3.7. As a function of the length of waveguide, z, all we need to know for the Q_c scaling is the propagation constant in the waveguide. It is true that the ex-

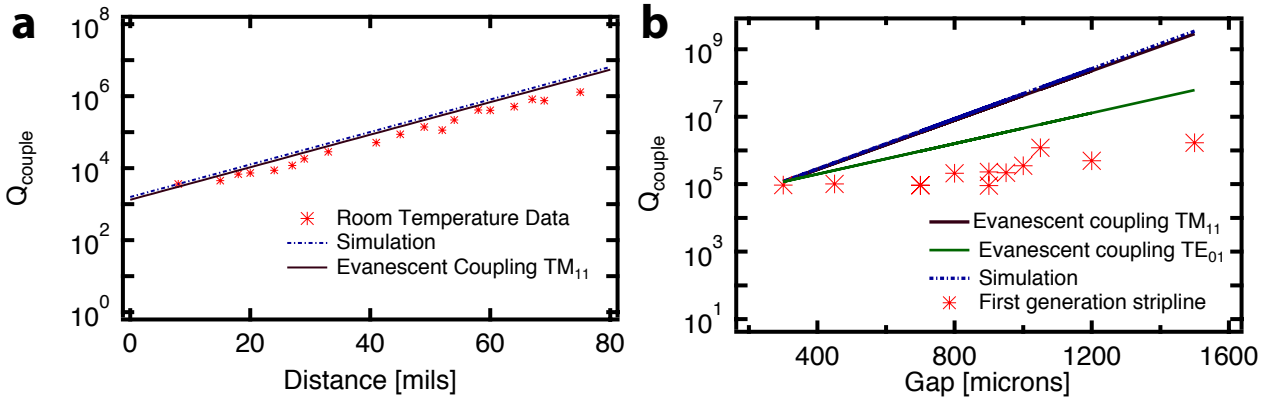

Figure 3.7: Evanescent Coupling to 3D Cavity and Stripline. In both figures the coupling quality factor is obtained through room temperature measurements of $|S_{21}|^2$ using the formula derived in section 5.4.1. a) Evanescent coupling to a rectangular waveguide cavity. Plotted as a blue dashed line are results from an HFSS simulation where one varies the distance between a rectangular wave guide cavity and the distance to the coupler pin. As the pin is retracted exponential growth of the coupling quality factor is observed. Plotted as a solid black line is an analytical prediction for the rectangular waveguide cavity based on the same principles used in section 3.6. The procedure used only gives the scaling (slope in the above plot). The first value of the analytical result is normalized to have the same value as the simulation and then plotted based on the '2β' value which is the slope. As points is data measured at room temperature in incremental steps. Excellent agreement is found between all three. b) Evanescent coupling to a stripline resonator. The dashing blue line is the results for coupling quality factor from an HFSS measurement as the distance between the resonator and incoming leads is increased. In solid black, is a line normalized to the first coupling quality factor found from simulation and whose slope is determined from the '2β' value calculated for the stripline. In green, is a line predicting the coupling quality factor if the stripline was coupled to the lowest mode allowed to propagate in the rectangular waveguide which has a $2\beta = 5.2mm^{-1}$. In red are measurements performed at room temperature of the stripline setup. The slope of the measurements, $2\beta = 2.7mm^{-1}$, is substantially different than theoretical, $2\beta = 8.2mm^{-1}$ and simulated predictions, $2\beta = 8.3mm^{-1}$. It seems that no matter how long the gap is between the resonator and the leads a residual coupling remains. In green are measurements of coupling quality factor carried out in an indium coated stripline holder that is then welded together. The slope from this data seems to be better in line with what is expected.

act propagation constant for a rectangular waveguide cavity partially filled with dielectric requires solving a transcendental equation corresponding to the exact mode in the waveguide [48]. However, due to the small cross section of the rectangular waveguide (1mm by 1.2mm) the propagation constant is changed by less than a .5% between vacuum or filled entirely with sapphire ($\epsilon_r = 10$). For these reasons we will use the relative dielectric constant of 6 and not worry about the sub percent precision. In our case $2\beta \approx 8.2\text{mm}^{-1}$. This means that for every 85 microns of rectangular waveguide added between the stripline resonator and the incoming leads we expect the coupling quality factor to double.

3.6.1 Asymmetry and Coupling Through TE_{01} Mode

A potential caveat to the previous section was that largely the asymmetry between the top half of the stripline with vacuum as the dielectric and the bottom half with sapphire as the dielectric ($\epsilon_r \approx 10$) was only handled in the waveguide portion. Two methods to approach this problem is to make further approximations to the previous sections to introduce asymmetries to see what effect asymmetries have on the coupling. The second option is to fully assume the worst case scenario–that the stripline resonator couples exclusively through the lowest mode of the rectangular waveguide. If the stripline were to couple exclusively through the lowest mode which is the TE_{01} (1 for the longest side of the rectangular cross section), then $2\beta = 5.2mm^{-1}$. In figure 3.7 (b) the green line is the trend one would expect if the coupling to the stripline was exclusively through the lowest mode. As one can see this still does not fit the data. If one fits the

data the extracted value is $2\beta_{meas} = 2.7mm^{-1}$. From this we conclude that evanescent coupling through a rectangular waveguide cavity cannot faithfully describe what is observed. The suspected culprit for the broken symmetry is the longitudinal cut. In section 3.9.3 two different paths to remedying the pervasive coupling are described. In hindsight, one could be suspicious about a longitudinal cut for a rectangular waveguide since it is typical for rectangular waveguides to be joined transverse to the direction of propagation rather than longitudinally.

3.7 Quality Factor Measurements

In general the total quality factor of a resonator will be an inverse sum to all methods of dissipation:

$$\frac{1}{Q_{tot}} = \sum_{k}^{\infty} \frac{p_k}{Q_k} \tag{3.43}$$

This means that the simple measurement of a quality factor is an inverse some of many different forms of dissipation. A necessary form of dissipation is coupling to the external environment. For the striplines measured we elected to design and measure them for transmission measurements. The major reason being that transmission measurements allow one to easily observe a broad frequency response to the sample. Furthermore, to simplify the problem we elect to perform measurements on symmetrically coupled striplines. Using symmetric coupling we can separate equation 3.43 into intended dissipation, coupling to the 50 Ω line, and unintended dissipation which we will call the internal quality factor,

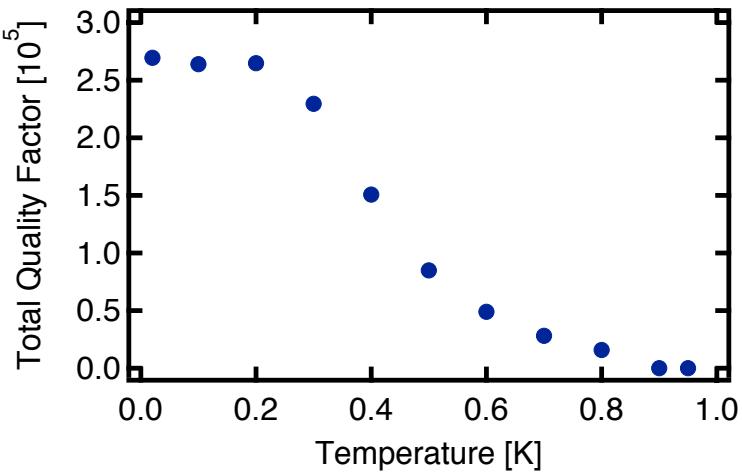

Figure 3.8: Total Quality Factor versus Temperature. Plotted above is the total quality factor of a stripline resonator with a 1200 μm gap on either side of the resonator. At low temperatures the quality factor saturates to about $265,000$. At room temperature the coupling quality factor was measured to be of order $500,000$ which suggests that the stripline resonator's internal quality factor is in excess of 1million. These measurements were done in transmission which without a reliable "through" calibration makes it difficult to determine the coupling quality factor at cryogenic temperatures.

Q_i :

$$\frac{1}{Q_{tot}} = \frac{2}{Q_c} + \frac{1}{Q_i} \tag{3.44}$$

Solving for Q_i we get:

$$Q_i = \left(\frac{2}{Q_c} - \frac{1}{Q_{tot}}\right)^{-1} \tag{3.45}$$

The internal quality factor contains all the information desired related to loss mechanisms and it is this quality factor multiplied by the participation ratio which sets the bound one can place on the quality factor of an individual constituent. From equation 3.45 it should be apparent that knowing ones coupling quality factor is essential for determining the internal quality factor. Figure 3.10, shows the total quality factor of a stripline structure as a function of temperature at the base plate of the dilution refrigerator. The total quality factor is nearly half the coupling quality factor measured at room temperature making it difficult to precisely state the internal quality factor of this device. In fact, the inability to make the coupling arbitrarily small hampered our ability to state definitively the coupling quality factor. Several other devices with similar coupling quality factors were measured and all roughly had $\frac{2}{Q_c} \approx \frac{1}{Q_{tot}}$. However, since the total quality factor seems to be predominately limited by the coupling quality factor that gives us reason to suspect that the stripline structures are relatively low loss and that internal quality factors in excess of a million are possible.

3.8 Kinetic Inductance Ratio Measurements

In this section we describe measurements done to determine the kinetic inductance ratio of our enclosed stripline resonators. The inverse quality factor and fractional frequency shift can be related to the surface resistance, R_s and surface admittance X_s as follows [58, 66]:

$$\frac{1}{Q_{tot}} + 2j\frac{df}{f} = \frac{\alpha}{\omega\mu\lambda_0}(R_s + j\delta \mathrm{X}_s) \tag{3.46}$$

Although a great deal of literature exists that investigates the AC conductivity of superconductors a full and exhaustive treatment is beyond the scope of this dissertation [67, 68, 69, 70, 71, 72]. In equation 3.46, α is the kinetic inductance ratio, ω is the angular frequency, λ_0 is the London penetration length, and δ is the anomalous skin depth which in the superconducting case becomes the London length. In figure 3.9, the fractional frequency change of the stripline resonator is tracked as the dilution refrigerator temperature is changed. This data is fitted to determine α and T_c from a numerical integration of Mattis and Bardeen's formulas for the full AC conductivity of a BCS superconductor [66]. We are able to extract the total kinetic inductance ratio for the stripline which includes the deposited film (center conductor) and the aluminum housing (ground). Since we would like to separately discuss the quality factors of the deposited films as well as the bulk aluminum ground in figure 3.9 b we separately measure the kinetic inductance fraction of the bulk aluminum ground. Simply by subtracting the bulk aluminum kinetic inductance fraction from the total ki-

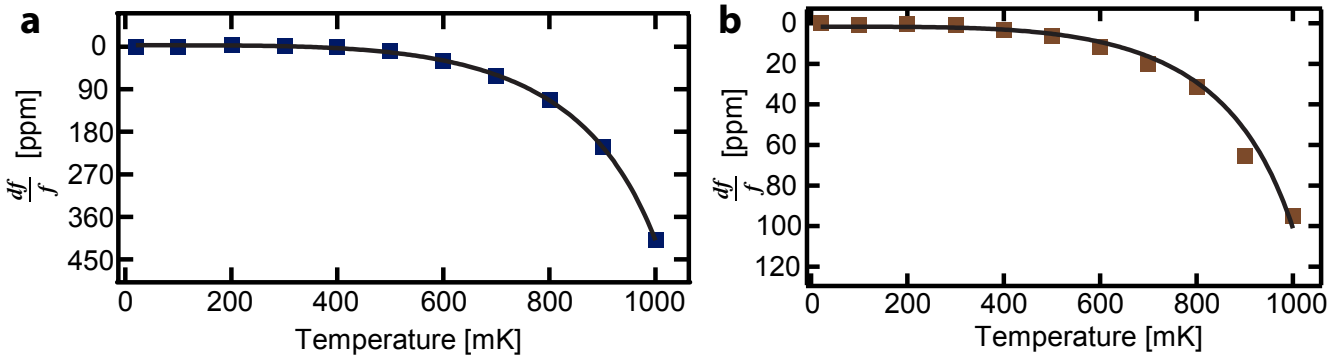

Figure 3.9: Measured Kinetic Inductance of Stripline Resonator and Holder. a) The fractional frequency change of a stripline resonator whose center conductor is aluminum as well as the outer holder being aluminum. The measured kinetic inductance fraction, $\alpha_{total} = 1.06 \cdot 10^{-3}$, encompasses the kinetic inductance not only for the center conductor but also the outer conductor. In b) we replace the center conductor with niobium, which should not vary much over this temperature range, to measure the outer conductor kinetic inductance ratio, $\alpha_{outer} = 2.4 \cdot 10^{-4}$. This gives a kinetic inductance fraction of $\alpha_{center} = .82 \cdot 10^{-4}$ for the center conductor when its width is 300 μm which is very close to the simulated value of $.8 \cdot 10^{-3}$ and the predicted value of $.6 \cdot 10^{-3}$.

netic inductance fraction we readily get the kinetic inductance fraction of the deposited film. For the 300 μm wide deposited aluminum center conductor we find its kinetic inductance fraction to be $\alpha_c \approx .8 \cdot 10^{-3}$.

3.9 Limitations

In the first few designs of the striplines there were worrisome issues holding back the development of this architecture. In the following sections we will describe issues with persistent coupling to the environment that cannot be turned off and the frequency stability issues.

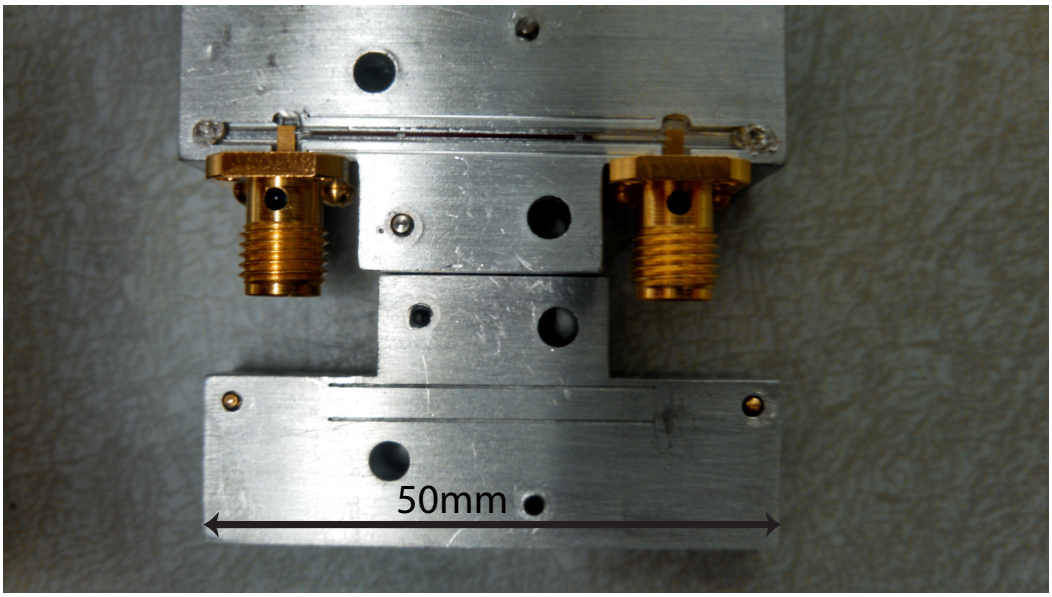

Figure 3.10: Second generation stripline design. In the second generation of the stripline holders the major issues to address were the coupling to the resonators as well as the frequency stability of the resonators. To address the coupling indium grooves were added to improve contact between the two halves. Also, the cut was now place at the top of the rectangular structure rather than at the middle. To address frequency stability the microwave launchers were designed to be over the chip so that indium as well as pogo pins (beryllium-copper center) could clamp the edges of the chip. Unfortunately, all of these changes did not improve the coupling nor the frequency stability. From this we conclude that having a true RF short is necessary for high quality factor resonators in this design as well as other designs that drive a current across an interface similarly to what is found by others [73].

3.9.1 Coupling

As described in section 3.6 the coupling to the stripline should be in principle able to made as arbitrarily small as desired. Yet in Fig. 3.7 b, room temperature measurements that extract coupling quality factors according to section 5.4.1 strongly contradict this claim. As can be seen the room temperature measurements disagree both with theoretical calculations and from simulation. What is even more troubling is that it does not seem that there exists a gap distance that can even reliably produce a coupling quality factor in excess of a million. This issue with persistent coupling to the environment around a coupling quality factor of a million is quite suspicious. At the very least, a take home message should be that to achieve quality factors in excess of a million the RF environment of the structures must be not only well designed but also well implemented.

The primary explanation for the persistent coupling in the stripline geometry is attributed to the two halves of the ground plane not making perfect RF contact. This is despite using an indium seal around all edges. By not having a perfect RF contact at all frequencies a parallel plate waveguide between the external shielding allows transmission regardless of the gap between the leads and the center pin of the resonator.

3.9.2 Frequency Stability

Aside from issues in coupling there are also issues with frequency stability of the higher quality factor striplines. The striplines are sensitive to vibrations causing

changes of order the linewidth or larger. By shutting off the pulse tube of the dilution refrigerator the vibrations decrease and allow a higher quality factor measurement. Furthermore, the vibrations can easily be made worse by knocking on the support structure of the dilution refrigerator causing the resonance to change frequency substantially.

3.9.3 Issue Resolution

The explanation for the uncontrolled weak coupling is that our ground is really two different grounds that are not well connected. The two options for fixing this are to either find a way to weld the two grounds together to make a great RF short or machining everything so that the ground truly is one continuous piece of metal. Both of these options have been pursued with encouraging results. Since I personally have not carried out the measurements I will only give highlights on material that has been presented. By making a single continuous structure for the ground of the stripline has allowed not only carefully controlled coupling but also high quality factor striplines. In the enclosed, single ground geometry quality factors routinely above five million are measured up to nearly nine million [74]. Additionally, indium welding of the ground enclosures seems to improve the coupling as well though more work is needed [75, 73]. The methods used to stabilize the striplines in this geometry make it seem that producing qubits with lifetimes in excess of 100 μs should be possible.

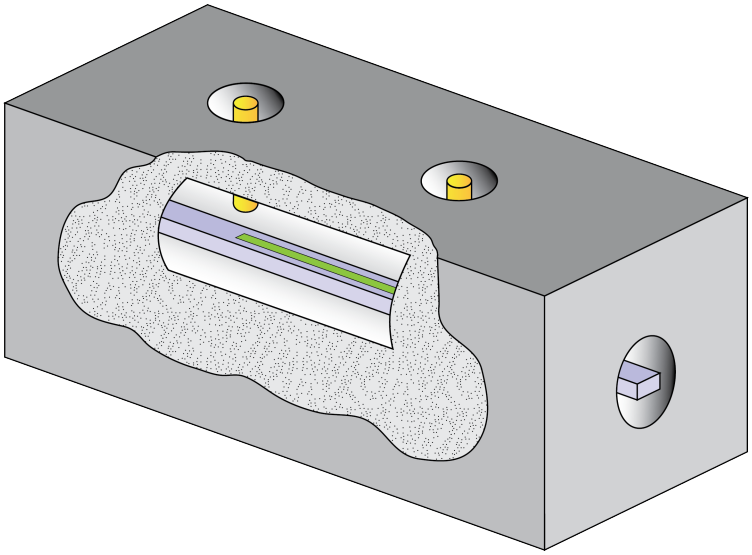

Figure 3.11: Above is a cartoon schematic of an architecture that has resolved many of the issues that plagued the original stripline. In purple is a substrate that supports the deposited superconductor (blue). In yellow are center pins from an SMA connector that allow evanescent coupling to the stripline resonator similarly to the standard coupling to a rectangular waveguide resonator. A hole is machined into an aluminum block which allows the stripline chip to be slide inside the holder. The drilled hole gives a uniform, single ground plane for the stripline. In this design coupling quality factors in excess for 3 billion have been measured repeatably whereas in previous devices the largest coupling quality factor measured was of order one million. In this design the placement of the stripline affects the coupling quality factor and a misplacement can result in coupling quality factors too large to make single photon measurements plausible.

3.10 Future Outlook

In this chapter the ground work for using enclosed striplines in quantum information science was laid. The issues that plagued the development of the stripline are issues that must be addressed by all groups going forward. In scaling up for a logical qubit or a quantum computer dense circuitry must be made to allow sufficient control of these quantum devices. Integration of complex circuitry will require the ability to make high quality RF shorts to tie together different ground planes. Truly single ground planes will allow for better electromagnetic isolation as well as well controlled coupling. Furthermore, having a single ground conductor improves the frequency performance of devices that rely on external geometry. Going forward all of these issues need be addressed. Fortuitously, the Yale group has been working on this explicitly through micromachining and indium welding [76].

4

Circuit Quantum Electrodynamics

In this chapter we describe the light-matter interactions between superconducting circuits and microwave photons. Quantum optics is the general field of physics devoted to the study of light-matter interactions. A full and comprehensive description of quantum optics is beyond the scope of this thesis; however, many references exist and is covered wonderfully as an advanced undergraduate

text book in reference [77] and given further treatment in the standard graduate references [78, 79]. Cavity Quantum Electrodynamics (CQED) [80] is a regime of quantum optics where the coupling between atoms and cavities occur much faster than dissipative channels, unveiling beautiful physics that shared the 2012 Nobel prize in physics. Inspired by CQED, circuit Quantum Electrodynamics (cQED) is a similar conceptual framework that makes use of mesoscopic, microwave circuits to play the analogous role of atoms coupled to microwave cavities.

A starting point for CQED is a single two level system (atom) coupled to a cavity which can affectively be modeled by the Jaynes-Cummings Hamiltonian[81, 82]:

$$\mathbf{H_{JC}} = \hbar\omega_c \mathbf{a}^\dagger \mathbf{a} + \hbar\omega_a \frac{\sigma_\mathbf{z}}{2} + \hbar g(\mathbf{a}\sigma_+ + \mathbf{a}^\dagger \sigma_-) \tag{4.1}$$

In equation 4.1 ω_c is the angular frequency of the cavity mode, and $\mathbf{a}^\dagger$, $\mathbf{a}$ are the raising and lowering operators of the cavity. Also in 4.1, the idealized two level system has an angular resonance frequency ω_a, and inversion operator $\sigma_\mathbf{z}$ (eq.4.2), and raising and lowering operators of the two level system σ_+ (eq.4.3) or σ_- (eq.4.4) respectively. We define the two level system operators in terms of its two states, $|g\rangle$, $|e\rangle$, as:

$$\sigma_\mathbf{z} = |e\rangle\langle e| - |g\rangle\langle g| \tag{4.2}$$

$$\sigma_+ = |e\rangle\langle g| \tag{4.3}$$

$$\sigma_- = |g\rangle\langle e| \tag{4.4}$$

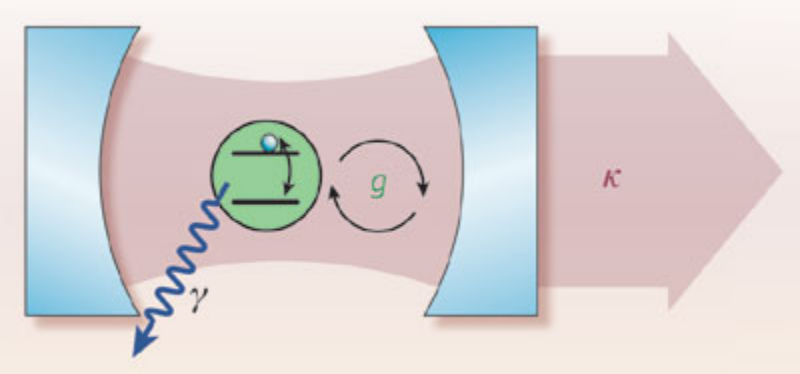

Figure 4.1: Jaynes-Cummings Model. Figure from Ref. [83]. Mirrors (blue) form a resonant photon mode (pink) that interacts with a two level system, atom (green), at a rate g. The cavity mode dissipates at a rate κ and the atom dissipates energy at a rate γ. The strong coupling regime is reached when the interaction strengths are larger than the dissipation rates specifically when $g \gg \kappa,\ \gamma$.

In the Jaynes-Cummings Hamiltonian, when the two level system is brought onto resonance with the cavity the avoided crossing of the energy splitting is $2g$ [84]. However, the splitting will be dependent on the number of photons in cavity ($\sqrt{n}$ dependence). The photon number dependent splitting was beautifully observed in Ref. [85].

4.1 Cavity Quantum Electrodynamics

In a letter to Robert Hooke, Sir Isaac Newton humbly writes, "If I have seen further, it is by standing on the shoulders of giants." Similarly, it is hard to discuss circuit QED without paying homage to CQED. The pioneering work by Nobel Laureate Serge Haroche and Jean-Michel Raimond is a textbook unto itself [86]. In CQED, Rydberg atoms are sent through a high quality factor mi-

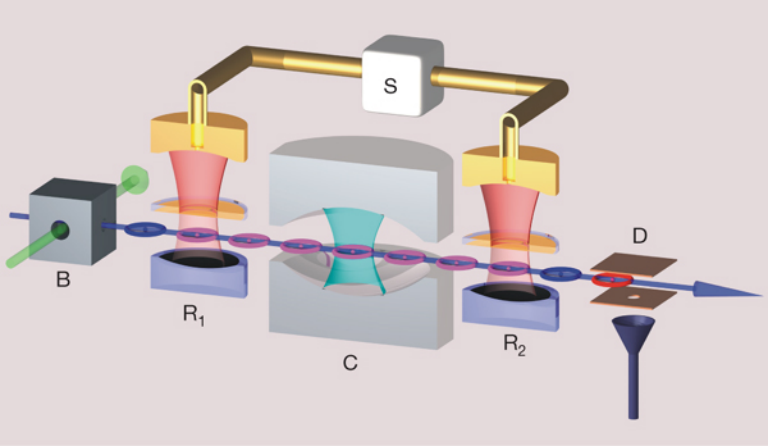

Figure 4.2: CQED Realization. Figure from Ref. [89]. Velocity-selected by laser optical pumping, Rydberg atoms are prepared in box B, out of a thermal beam of rubidium atoms. The atoms then enter the first Ramsey cavity R_1, cross the cavity C, followed by the second Ramsey cavity R_2 (both Ramsey cavities are excited by the classical microwave source S), and finally detected in the state selective field ionization detector D. The three cavities are enclosed in a box at 0.8 K that shields them from thermal radiation and magnetic fields.

crowave cavity and couple off resonantly to the cavity [87] (Fig. 4.2). By observing the quantum state change of the incoming and out going Rydberg atoms one can make, monitor, and manipulate the quantum state of the high quality factor cavity. A fun video to show those unfamiliar with physics was made by Minute Physics after the 2012 Nobel Prize in physics announcement and can be found here [88]. A distinguishing feature of CQED is that the device under study is the cavity rather than the atoms used. To reveal the rich, quantum features of a cavity one needs an atom or atomic like structure [59]. Haroche's work is very well complemented by Dave Wineland, the other recipient of the 2012 Nobel Prize in physics, who also used cavities and atoms but instead focused on the quantum nature of atoms.

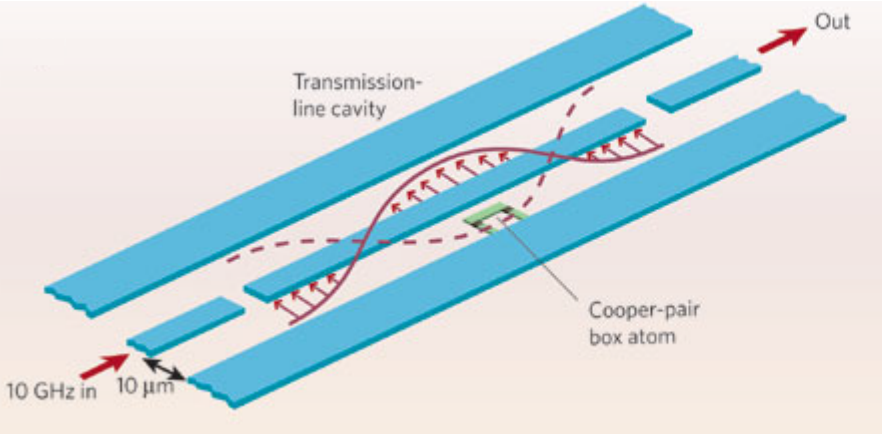

Figure 4.3: Circuit QED. Figure from Ref. [83]. Circuit analogue of a cavity QED system. In blue, a transmission line cavity is formed by lithographically defining breaks in the center conductor which results in a half wavelength resonator in the transmission line. An artificial atoms comprised of a Josephson junction and other lithographically defined features dipole couples to the transmission line resonator through the electric field of the resonator (red arrows).

4.2 Circuit Quantum Electrodynamics

We begin by asserting that one can make a circuit analogue to cavity QED [90]. In the following sections we will show how this is possible but a brief introductory summary will help one understand the organization. As can be seen in Fig. 4.3 a lithographically defined resonator is formed from a 1D transmission line by inserting breaks in the center pin. The length of the resonator determines the fundamental mode of the resonant cavity with wavelength being twice the length. An artificial atom (cooper-pair box in this case Ref. [91]), dipole couples to the transmission line resonator. This dipole coupling can be quite larger, of order a few percent of the frequency of the artificial atom transition frequency, and allows strong coupling between the microwave cavity and the artificial atom

to occur. This strong coupling allows one to reproduce any experiment performed in cavity QED as well as allowing new experiments to be performed.

Lithographically defined resonators are not a unique development for instance chapter 3 describes one such resonator. The unique development of circuit QED is the strong coupling provided by the dense Electric field and an artificial atom. The artificial atom is a nonlinear LC oscillator. The nonlinearity arises from a Josephson junction being apart of the LC oscillator. In section 4.3 we will describe how a Josephson junction can be described in circuit terms. The following section demonstrates the quantization of an LC oscillator (cavity). Using the LC oscillator as the guiding point we alter the quantization to show how an LC oscillator with a Josephson junction realizes an anharmonic oscillator. Finally in section 4.5 we show how an LC oscillator coupled to a Josephson junction based circuit can realize a Jaynes-Cummings Hamiltonian and consequently a circuit QED environment.

4.3 Josephson Junction as a Circuit Element

We begin by looking at the Josephson equations for the current through, I_J, and voltage across, V_J, a superconducting-insulating-superconducting barrier:

$$I_J = I_0 \sin \delta(t) \tag{4.5}$$

$$V_J = \frac{\hbar}{2e}\dot{\delta}(t) \tag{4.6}$$

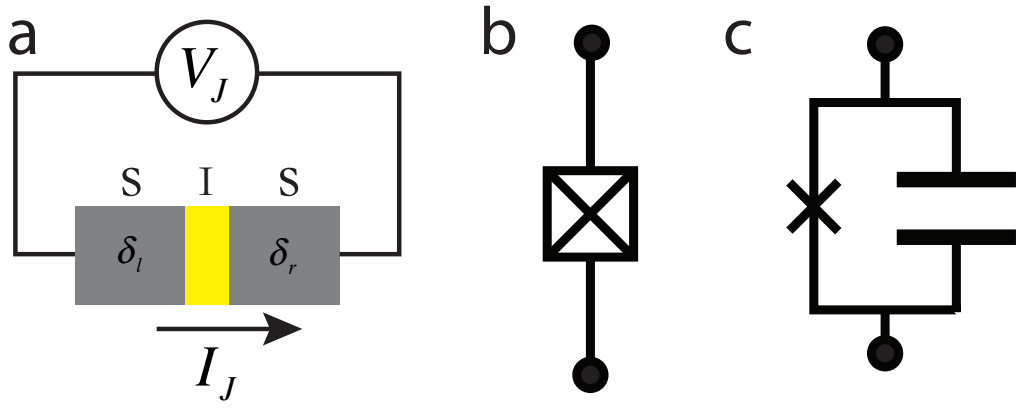

Figure 4.4: Josephson junction schematic and circuit equivalent. a) A superconductor (grey) insulator (yellow) superconductor (grey) Josephson junction. In this thesis the superconductor used is aluminum and the insulator is aluminum oxide typically 1.5nm thick. A Josephson current, I_J, flows from one island to the other while the voltage across the Josephson junction is V_J. We define $\delta = \delta_l - \delta_r$ as the superconducting phase difference between the two islands. b) Microwave circuit symbol which is shown explicitly in c) as a nonlinear inductor shunted by a capacitor. Typically the capacitance of the junction is negligible in transmons and the physics is dominated by the Josephson inductance, L_J.

In equation 4.5, I_0 is the critical current of the Josephson junction and $\delta(t) = \delta_l - \delta_r$ is the time dependent phase difference between the two superconducting sides of the junction. The voltage across the junction, Eq. 4.6, is expressed in terms of the reduced Planck constant, $\hbar$, the electron charge, e, and the time derivative of the phase difference between the two superconducting leads $\dot{\delta}(t)$. By taking the time derivative of equation 4.5 we express $\dot{\delta}(t)$ as:

$$\dot{I}_J = I_0 \cos\delta(t)\dot{\delta}(t) \Rightarrow \dot{\delta}(t) = \frac{\dot{I}_J}{I_0 \cos\delta(t)} \tag{4.7}$$

Using the result for $\dot{\delta}(t)$ the voltage across the junction is:

$$V_J = \frac{\hbar}{2e}\dot{\delta}(t) = \frac{\hbar}{2eI_0 \cos\delta(t)}\dot{I}_J \tag{4.8}$$

We now recognize that equation 4.8 is in the form of an inductance relationship ($V_J \propto \dot{I}_J$). We will describe the proportionality as the Josephson inductance, L_J, and define this nonlinear inductance as:

$$L_J = \frac{\hbar}{2eI_0 \cos\delta(t)} \tag{4.9}$$

A nonlinear inductor is exciting because this could potentially have an anharmonic spectrum. Furthermore we note that this inductance is not associated with a magnetic field. The inductance is due to the kinetic energy of the Cooper pairs tunneling through the junction. Explicitly this means that the Josephson junction's inductance is purely kinetic inductance. For this reason, typical

transmon qubits have kinetic inductance fraction of order unity since the inductance of the transmon is primarily due to the Josephson junction.

It is fair to ask at what frequency the Josephson junction self resonates. For Al-AlOx-Al junctions that have an overlap area of 100nm by 100nm, typical Josephson inductance values are of order 10nH and from a simple parallel plate calculation a capacitance of roughly 1fF. This order of magnitude for Josephson inductance and capacitance sets the self resonance of the junction at nearly 50 GHz. To lower the fundamental frequency to the 5-10 GHz range a simple solution would be to either inductively or capacitively shunt the Josephson junction. A shunting capacitance of 50 fF or shunting inductance of 1.5 μH would bring the resonance of the combined circuit to frequencies in the 5-10 GHz range. Designing a microwave circuit with 50 fF of shunting capacitance is easy to achieve; however, 1.5 μH of inductance is a challenging task. Conceptually, a single junction shunted by a large capacitor is described as a transmon [92, 93, 94], and a single junction shunted by a so called super-inductance is described as a fluxonium [95, 96]. Also, it is worth noting that the transmon and the fluxonium are both descendants of the original charge qubit–the cooper pair box [91].

4.4 Circuit Quantization

4.4.1 LC Oscillator

The rules of circuit quantization are treated fantastically well in references [97, 94, 98, 99] and will not be reproduced in full here. For an LC oscillator we can

write its Hamiltonian in terms of the charge on the capacitor, q, and flux through the inductor, ϕ, as:

$$H_{LC} = \frac{q^2}{2C} + \frac{\phi^2}{2L} \tag{4.10}$$

From equation 4.10, the angular frequency, ω, and impedance, Z, are computed to be:

$$\omega = \frac{1}{\sqrt{LC}} \tag{4.11}$$

$$Z = \sqrt{\frac{L}{C}} \tag{4.12}$$

To quantize equation 4.10 the charge now becomes the charge operator, $\mathbf{q}$, and similarly the flux becomes the flux operator, ϕ which allows one to define creation, $\mathbf{a}^\dagger$, and annihilation, $\mathbf{a}$, operators to realize a quantum harmonic oscillator:

$$H_{LC} = \hbar\omega(\mathbf{a}^\dagger\mathbf{a} + 1/2) \tag{4.13}$$

Where we define the creation, $\mathbf{a}^\dagger$, and annihilation, $\mathbf{a}$, of the LC oscillator as:

$$[\mathbf{a}, \mathbf{a}^\dagger] = 1 \tag{4.14}$$

$$\phi = \Phi_{ZPF}(\mathbf{a} + \mathbf{a}^\dagger) \tag{4.15}$$

$$\mathbf{q} = -iQ_{ZPF}(\mathbf{a} - \mathbf{a}^\dagger) \tag{4.16}$$

And the zero point fluctuations of the flux and charge are:

$$\Phi_{ZPF} = \sqrt{\frac{\hbar Z}{2}} \tag{4.17}$$

$$Q_{ZPF} = \sqrt{\frac{\hbar}{2\ Z}} \tag{4.18}$$

4.4.2 Anharmonic Oscillator: The Transmon

To treat the case of a single Josephson junction shunted by a capacitor we will modify equation 4.13 by including the Josephson energy and removing the linear inductance:

$$H_T = \hbar\omega_a\ (\mathbf{a}^\dagger\mathbf{a} + 1/2) - E_J\left(\cos(\phi) + \frac{\phi^2}{2}\right) \tag{4.19}$$

Where we have defined $E_J = \dfrac{I_0\Phi_0}{2\pi}$ as the Josephson energy where I_0 is the critical current of the junction and $\Phi_0 = \dfrac{h}{2e}$ is the flux quantum. Expanding $\cos\phi$ and only keeping terms related to energy differences gives:

$$H_T = \hbar\omega_a\ \mathbf{a}^\dagger\mathbf{a} - \frac{E_J}{24}\phi^4 + O(\phi^6) \tag{4.20}$$

Using the definition for ϕ as in equation 4.15 with the caveat that $L \rightarrow L_J$ equation 4.20 becomes:

$$H_T \approx \hbar\omega_a\ \mathbf{a}^\dagger\mathbf{a} - \frac{E_J}{24}\Phi_{ZPF}^4(\mathbf{a} + \mathbf{a}^\dagger)^4 \tag{4.21}$$

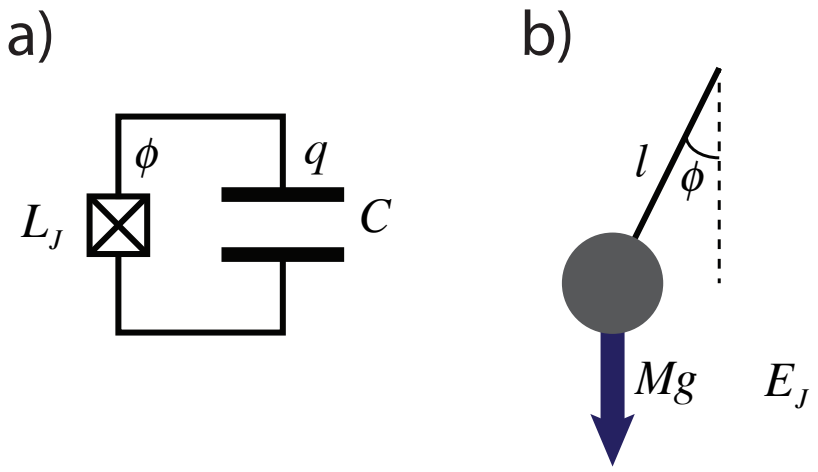

Figure 4.5: Circuit representation of a transmon. a) The transmon consists of a Josephson junction (square with x) with nonlinear inductance L_J shunted by a capacitor, C. b.)Analogy can be made between a transmon and a quantum rotator [92] and for $\phi \ll 1$ this system realizes an anharmonic oscillator.

Finally by taking only counter rotating terms we realize the simplest form of the transmon Hamiltonian:

$$H_T \approx \hbar\widetilde{\omega}_a \, \mathbf{a}^\dagger\mathbf{a} - \frac{\hbar\alpha}{2}\mathbf{a}^{\dagger\mathbf{2}}\mathbf{a}^{\mathbf{2}} \tag{4.22}$$

In equation 4.22 we have defined $\widetilde{\omega}_a = \omega_a - \alpha$ and $\alpha = \frac{E_J}{12}\Phi^4_{ZPF}$. The coefficient α is commonly referred to as the anharmonicity of the transmon with typical values in the hundreds of MHz. The most faithful description of the anharmonicity is that it is proportional to the energy difference of the ground state of the anharmonic oscillator and its first excitation, $\hbar\alpha = E_0 - E_1$. The approximation we made in expanding the cosine term of the Josephson junction is most accurate for a small number of excitations of the transmon. Equation

4.22 can be thought of in terms of a mass spring system with ϕ playing the role of position and $\mathbf{q}$ the role of momentum. The choice of which electrical variable corresponds to which mechanical variable is arbitrary. However, chosen as such, the nonlinearity of the junction can be thought of as altering the potential energy of the system (nonlinear spring constant) rather than the nonlinearity of the junction serving as a relativistic correction to the mass. In cQED, typically only the first two energy levels of the transmon are used so equation 4.22 can be rewritten as a two level system with energy levels $|g\rangle, |e\rangle$ as:

$$H_{Tr} = \hbar\widetilde{\omega}_a |e\rangle \langle e| \tag{4.23}$$

Written as a two level system, equation 4.23 suggests that a capacitively shunted Josephson junction could fulfill the role of a two level system in a Jaynes-Cummings Hamiltonian.

4.5 Transmon Coupled to Harmonic Oscillator

The previous two sections individually arrived at the quantum Hamiltonians for electrical circuits. The culmination of that effort is this section where a quantum LC oscillator is coupled to an anharmonic LC oscillator allowing one to create a CQED system with purely electrical circuit elements [90, 100]. For the case of a transmon coupled to an LC oscillator we can say the total Hamiltonian will be a combination of the transmon Hamiltonian, H_T, the LC oscillator

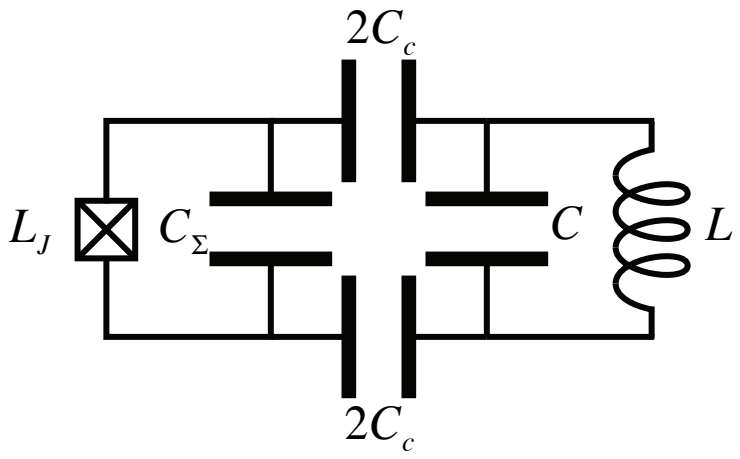

Figure 4.6: Circuit representation of transmon coupled to LC oscillator. The transmon consists of a Josephson junction (square with x) with nonlinear inductance L_J shunted by a capacitor, C_Σ is capacitively coupled,C_C, to an LC oscillator.

Hamiltonian, H_{LC}, and an interaction Hamiltonian, H_O:

$$H_{tot} = H_T + H_{LC} + H_O \tag{4.24}$$

To remind the reader, H_T is:

$$H_T \approx \hbar\omega_T \ \mathbf{a}^\dagger\mathbf{a} - \frac{\hbar\alpha}{2}\mathbf{a}^{\dagger\mathbf{2}}\mathbf{a}^{\mathbf{2}} \tag{4.25}$$

Likewise, H_{LC} is:

$$H_{LC} = \hbar\omega_r(\mathbf{b}^\dagger\mathbf{b} + 1/2) \tag{4.26}$$

The major work of this section is determining the interaction Hamiltonian which we will initially write in terms of the charge operators for the transmons,

$\mathbf{q}_T$, and the charge operator for the LC oscillator, $\mathbf{q}_{LC}$:

$$H_O = \frac{\mathbf{q}_T \mathbf{q}_{LC}}{C_{net}} \tag{4.27}$$

Where the net coupling capacitance, C_{net} is:

$$C_{net} = \frac{CC_\Sigma + C_\Sigma C_C + C_C C}{C_C} \tag{4.28}$$

We now rewrite the interaction Hamiltonian in terms of the quantum zero point fluctuations and raising and lowering operators of each charge operator as:

$$\begin{aligned} H_O &= \left(-iQ_{T,ZPF}(\mathbf{a} - \mathbf{a}^\dagger)\right)\left(-iQ_{r,ZPF}(\mathbf{b} - \mathbf{b}^\dagger)\right)\frac{1}{C_{net}} \\ H_O &= \frac{Q_{T,ZPF}Q_{r,ZPF}}{C_{net}}(\mathbf{a}^\dagger\mathbf{b} + \mathbf{a}\mathbf{b}^\dagger - (\mathbf{a}\mathbf{b} + \mathbf{a}^\dagger\mathbf{b}^\dagger)) \\ H_{O,rwa} &= \frac{Q_{T,ZPF}Q_{r,ZPF}}{C_{net}}(\mathbf{a}^\dagger\mathbf{b} + \mathbf{a}\mathbf{b}^\dagger) \end{aligned} \tag{4.29}$$

To arrive at equation 4.29 we have taken the rotating wave approximation. We can rewrite equation 4.29 in an even more suggestive form:

$$H_{O,rwa} = \hbar g(\mathbf{a}^\dagger\mathbf{b} + \mathbf{a}\mathbf{b}^\dagger) \tag{4.30}$$

With g defined as:

$$g = \frac{1}{2\sqrt{Z_T Z_{LC}}C_{net}} \tag{4.31}$$

We could also use equation 4.31 to estimate the dimensionless coupling ratio $\frac{g}{\omega}$:

$$\frac{g}{\omega} \approx \frac{C_c}{2\sqrt{C_\Sigma C}} \tag{4.32}$$

Using we can see for nominal values of $C = 320$ fF, $C_\Sigma = 70$ fF, and $C_c = 5$ fF that the coupling ratio is about 1.5%–which is quite large compared to atomic systems!

Now the full Hamiltonian of the coupled transmon and resonator system is:

$$H_{tot} \approx \hbar\omega_r(\mathbf{b}^\dagger\mathbf{b} + 1/2) + \hbar\widetilde{\omega}_T\ \mathbf{a}^\dagger\mathbf{a} - \frac{\hbar\alpha}{2}\mathbf{a}^{\dagger\mathbf{2}}\mathbf{a}^{\mathbf{2}} + \hbar g(\mathbf{a}^\dagger\mathbf{b} + \mathbf{a}\mathbf{b}^\dagger) \tag{4.33}$$

The above Hamiltonian is a Jaynes-Cummings Hamiltonian provided that we restrict the transmon to only single photon excitations which is a requirement routinely met in quantum superconducting circuits. We see all the characteristics necessary. A Hamiltonian term corresponding to cavity excitations, terms corresponding to an anharmonic oscillator (the most anharmonic oscillator is a two level system) and finally an interaction term that lets excitations in the cavity or transmon under go a unitary evolution at rate g (nominal values in circuit QED systems range from 10-100 MHz) where the excitation is created in one and destroyed in the other. The 'strong coupling' regime is entered when interaction strengths are larger than decoherence mechanisms. Explicitly when $g \gg \gamma_T, \kappa_r$ where γ_T is the decay rate of the artificial atom and κ_r is the decay rate of the cavity. For instance, in the case of a 3D transmon values such as $g \approx 100$ MHz, $\gamma_T \approx 3$ kHz, and $\kappa_r \approx 24$ kHz as in Ref. [62] are typical.

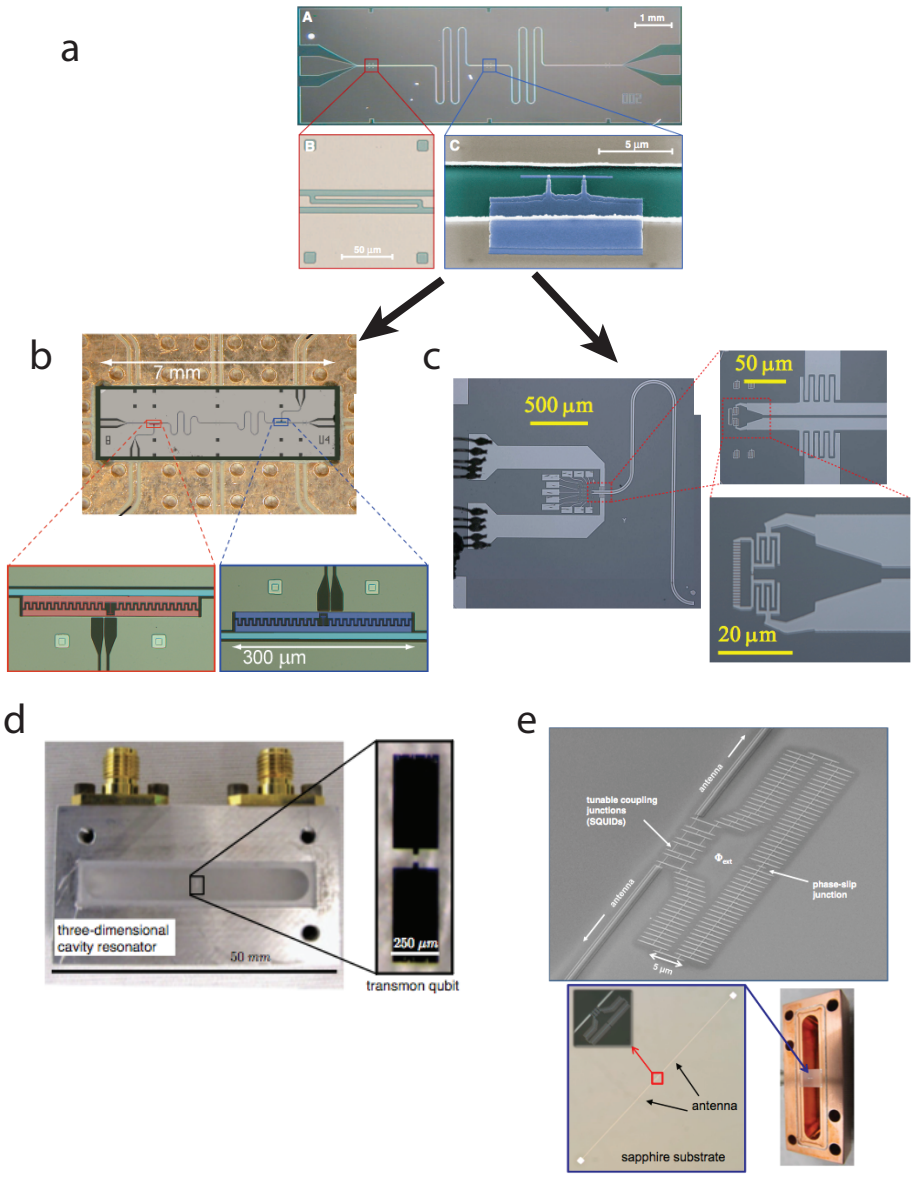

Figure 4.7: Small Junction ($E_J/E_C \approx 1$) Superconducting Qubits. a) The original small junction superconducting qubit: the Cooper pair box. b) The offspring of the Cooper pair box are the capacitively shunted Josephson junction, transmon, and c) the inductively shunted Josephson junction, fluxonium. d) and e) are the 3D versions of the transmon and fluxonium which due to their well defined electromagnetic environment have, at the writing of this thesis, the best coherence and energy relaxation times of any superconducting qubit.

4.5.1 Strong Dispersive Regime

The Jaynes-Cummings like Hamiltonian derived in equation 4.33 can be rewritten when the detuning between the resonator and the transmon is large compared to the interaction strength ($\Delta = |\omega_r - \omega_T| \gg g$) as (full details of derivation see Ref. [101]):

$$H_{tot} \approx \hbar\omega_T' \ (\mathbf{A}^\dagger\mathbf{A} + 1/2) + \hbar\omega_r'(\mathbf{B}^\dagger\mathbf{B} + 1/2) - \frac{\hbar\alpha_T}{2}\mathbf{A}^{\dagger\mathbf{2}}\mathbf{A}^{\mathbf{2}} - \frac{\hbar\alpha_r}{2}\mathbf{B}^{\dagger\mathbf{2}}\mathbf{B}^{\mathbf{2}} - \hbar\chi\mathbf{A}^\dagger\mathbf{A}\mathbf{B}^\dagger\mathbf{B} \tag{4.34}$$

In the dispersive limit $\chi \to \dfrac{2g^2}{\Delta},\ \alpha_T \to E_c,\ \alpha_r \to 0$. Equation 4.34 has become a frequent form to represent the coupled resonator and transmon system which treats the transmon's modest anharmonicity as a perturbation. Reliably coherent single junction transmons such as those in a rectangular waveguide cavity (Ref. [62]) are a reason for equation 4.34 being a common form for the Hamiltonian of a transmon coupled to a cavity. Equation 4.34 can be generalized for an arbitrary number of modes and to fourth order in the junction flux, ϕ, the general Hamiltonian is:

$$H_4 = \hbar\sum_i(\omega_i\mathbf{a}^\dagger\mathbf{a} - \frac{\alpha_i}{2}\mathbf{a}^{\dagger\mathbf{2}}\mathbf{a}^{\mathbf{2}}) - \hbar\sum_{i,j\neq i}\chi_{ij}\mathbf{a}^\dagger\mathbf{a}\mathbf{b}^\dagger\mathbf{b} \tag{4.35}$$

Where ω_i is the dressed frequency of the mode, α_i is the mode anharmonicity, and χ_{ij} is the state dependent shift between mode i and mode j.

4.6 Black box quantization

In this final section we will go over a major advancement for single junction devices, the so called black-box quantization (BBQ) [102] method. Where the BBQ theory and general approach truly shine is not relying on lumped element approximations to predict Hamiltonian parameters such as the anharmonicities of modes, their state dependent shift, and higher order corrections to those terms. In general one must have the full admittance matrix seen by the junction; however, for a single junction system in BBQ this simplifies to a single port measurement of $Y(\omega)$ allowing one to fully determine the Hamiltonian parameters from a single frequency dependent simulation. The information needed are the poles, $Y(\omega_i) = 0$, which correspond to undressed frequencies and the characteristic impedance at the resonance frequency, $Z_{c,i} = \sqrt{\frac{L_i}{C_i}}$. The characteristic impedance of the modes can be determined by using the admittance for a parallel LCR circuit:

$$Y(\omega) = j\omega C_i + \frac{1}{j\omega L_i} + \frac{1}{R_i} \tag{4.36}$$

Taking the derivative of the admittance with respect to angular frequency yields:

$$Y\,'(\omega) = j(C_i + \frac{1}{\omega^2 L_i}) \tag{4.37}$$

We are concerned with the characteristic impedance of the mode on resonance so we can use $\omega_i^2 = \frac{1}{L_i C_i}$:

$$Y'(\omega) = 2jC \tag{4.38}$$

Using $L_i = \frac{1}{\omega_i^2 C_i}$ the characteristic impedance of the mode on resonance is:

$$Z_{c,i} = \frac{1}{\omega_i C_i} \tag{4.39}$$

Realizing that from equation 4.38 we can write the capacitance C_i on resonance as:

$$C = \frac{\mathbf{Im}[Y'(\omega)]}{2} \tag{4.40}$$

Finally the characteristic impedance of the mode on resonance in terms of the poles of the admittance and the slopes of the poles is:

$$Z_{c,i} = \frac{2}{\omega_i \mathbf{Im}[Y'(\omega_i)]} \tag{4.41}$$

Which is fantastic because now by knowing the admittance across the junction as a function of frequency the Hamiltonian parameters can be fully determined. In practice, one obtains $Y(\omega)$ through an electromagnetic simulation (ANSYS' HFSS was used in this thesis). By using a 2D drawing of the deposited superconductor, the junction can be simulated as an imposed boundary condition with a series inductance of L_J (and if one desires a C_j or R_j). In parallel with the junction is a port that allows one to measure the imaginary part of the admittance as a function of frequency as seen by the junction. By knowing the

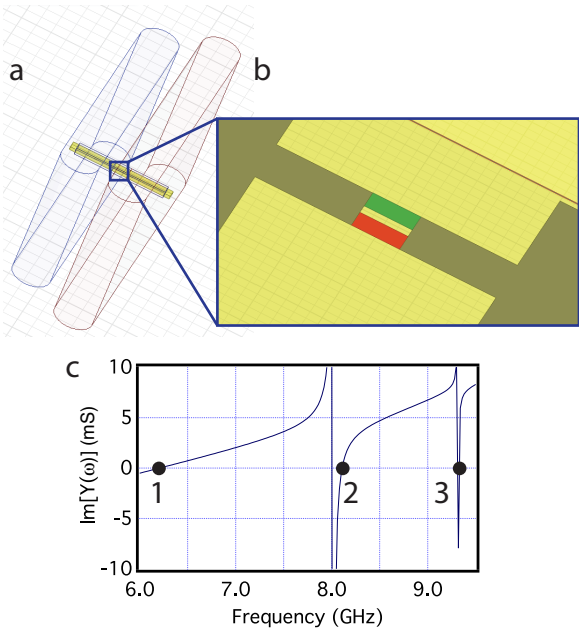

Figure 4.8: Black-box quantization HFSS simulation. a) CAD drawing of two 3D rectangular cavities coupled to a 'vertical' transmon [103]. b) Zoom in on faux junction area. In red is a lumped element set to be L_j. In green is the wave port that allows us to produce c) which is the frequency dependent imaginary part of the admittance seen by the junction. Points 1, 2, and 3 correspond to the different modes in our system corresponding to the transmon, the low frequency cavity, and the high frequency cavity. By inspection one can clearly see that the high frequency cavity will be more linear than the lower frequency cavity and correspondingly have a smaller state dependent shift to the transmon.

location of the poles in frequency, the slopes at the poles, and the junction inductance one can readily obtain the Hamiltonian parameters to arbitrary order. As coherence increases for qubits and cavities, knowing their anharmonicities, state dependent shifts, and higher order corrections will be crucial for successful implementations. For each mode we can write its contribution to fourth order in ϕ as:

$$H_m = \hbar\omega_m \mathbf{a}^\dagger \mathbf{a} - \hbar\alpha_m \mathbf{a}^{\dagger\mathbf{2}} \mathbf{a}^{\mathbf{2}} \tag{4.42}$$

Where ω_m and α_m are:

$$\omega_m = \omega_0 - \alpha_m \tag{4.43}$$

$$\alpha_m = \frac{e^2 Z_c^2}{\hbar L_j} \tag{4.44}$$

The above equations are only approximations as found in Ref. [102]. A common practice is to use QuTIP [104] to diagonalize the full system Hamiltonian. The circuit designer need only provide the zero crossings of the admittance, the slope at the zero crossings, and the junction inductance to extract Hamiltonian parameters from the electromagnetic simulation. Since QuTIP is open source it is quite conceivable that in the near future a function can be added to the existing database much in the same way there are built in functions for Wigner functions or Husimi Q functions. The advantage here is it would allow BBQ to become the industry standard for simulating quantum systems much as the transmon has become ubiquitous.

A nice observation is that anharmonic modes such as the transmon will have

much smaller slopes than cavity like modes with a very large slope. By knowing this coupled with the fact that the state dependent shift between modes is $\chi_{ij} \approx 2\sqrt{\alpha_i \alpha_j}$, one can quickly look at a plot and have a good sense for what the order of strength the Hamiltonian parameters are as well as when changing physical dimensions how that affects Hamiltonian parameters.

5

Experimental Techniques

This chapter is devoted to the details of the materials, equipment and procedures used in all the experiments in this dissertation. The general framework for experimental pursuits in the Schoelkopf group is circuit quantum electrodynamics (cQED). In this thesis a cQED experiment is realized with two rectangular waveguide cavities which have "box" mode resonances coupled to a transmon

qubit. These modes are pervasive even in planar structures where these modes are ignored and hopefully avoided as they potentially serve as another mechanism for decoherence. As the size and complexity of the quantum circuits used increases so to will the care and design required to preserve coherence.

5.1 Fabrication

5.1.1 Substrates

All fabrication in this thesis is performed on 50mm diameter, c-plane sapphire substrates. Sapphire is an anisotropic material and the c-plane version specifies the plane in which wafers are cut from the sapphire ingot. C-plane sapphire has a uniform dielectric constant along the large surface of the wafer ($\epsilon_{r,\parallel} \approx 9.3$) and a larger dielectric constant perpendicular to the the large surface ($\epsilon_{r,\perp} \approx 11.5$). The early work with stripline resonators was predominately on single side polished, 480 μm thick sapphire. Eventually, the Schoelkopf group began to only purchase double side polished, 430 μm sapphire and the stripline experiments migrated over accordingly. No appreciable changes in device performance were observed. All transmon fabrication performed in this dissertation was on 50mm diameter, 430 μm thick, c-plane, double side polished sapphire.

5.1.2 Lithography

Striplines

For the fabrication of the stripline resonators a bilayer resist is used for optical lithography. The bilayer of resist consists of a bottom layer of MicroChem LOR 5A ($\sim$ 480nm thick) and a top layer of MicroChem photoresist S1805 ($\sim$ 500nm thick). Details on the full procedure are available in appendix A. One thing to explicitly point out is that adhesion between the sapphire substrate and the first resist, LOR5A, was found to be inconsistent. After exposing and developing, the bilayer resist a common occurrence was for the the entire bilayer to be removed by the development process. To remedy the adhesion issue in subsequent experiments, the sapphire substrate was pretreated with HMDS and adhesion was no longer an issue. All the optical processing was done using the Heidelberg direct writer. This tool enabled fast turn around of devices and designs since the "mask" was a file produced by the experimentalist. For the standard configuration, the direct writer can reliably make feature sizes down to a few microns which is not an issue considering the smallest feature size for the stripline was of order a few hundred microns. By changing the laser head on the direct writer features down to $\sim$ .5 μm can be written but this project did not evolve to the point of requiring such small features.

Transmons

The transmon fabrication in this dissertation makes use of the Niemeyer-Dolan resist bridge technique [105, 106] to manufacture the required small Josephson junctions. The transmons fabricated in this dissertation used a bilayer of resist consisting of a 550 nm layer MMA EL-13 and a top layer of 120 nm of PMMA A3 both from MicroChem. The bottom layer of resist, MMA, must develop faster than the top layer of resist, PMMA, to produce an appreciable undercut for liftoff as well as producing a "bridge" of resist (Fig. 5.1 **A**). To aid in clearing out underneath the resist bridge, a "shadow" dose is applied at the bridge location that is about 3.5 times smaller than the dose used for areas that one intends to clear. A full and complete description of this process is given in appendix A. Electron beam lithography was accomplished in a Vistec EBPG 5000+, 100kV system. Sapphire substrates do not conduct and therefore it is necessary to deposit an anti-charging layer on top of the bilayer of resist to prevent beam deflection during writing. The anti-charging layer used in all the lithography in chapter 6 was a 13nm layer of aluminum. It is worth noting that others in RSL and QuLab have used gold as the anti-charging layer and fabrication results are comparable; however, the conductor used for the anti-charging layer affects the required dose used for not only clearing structures but also the "shadow" dose.

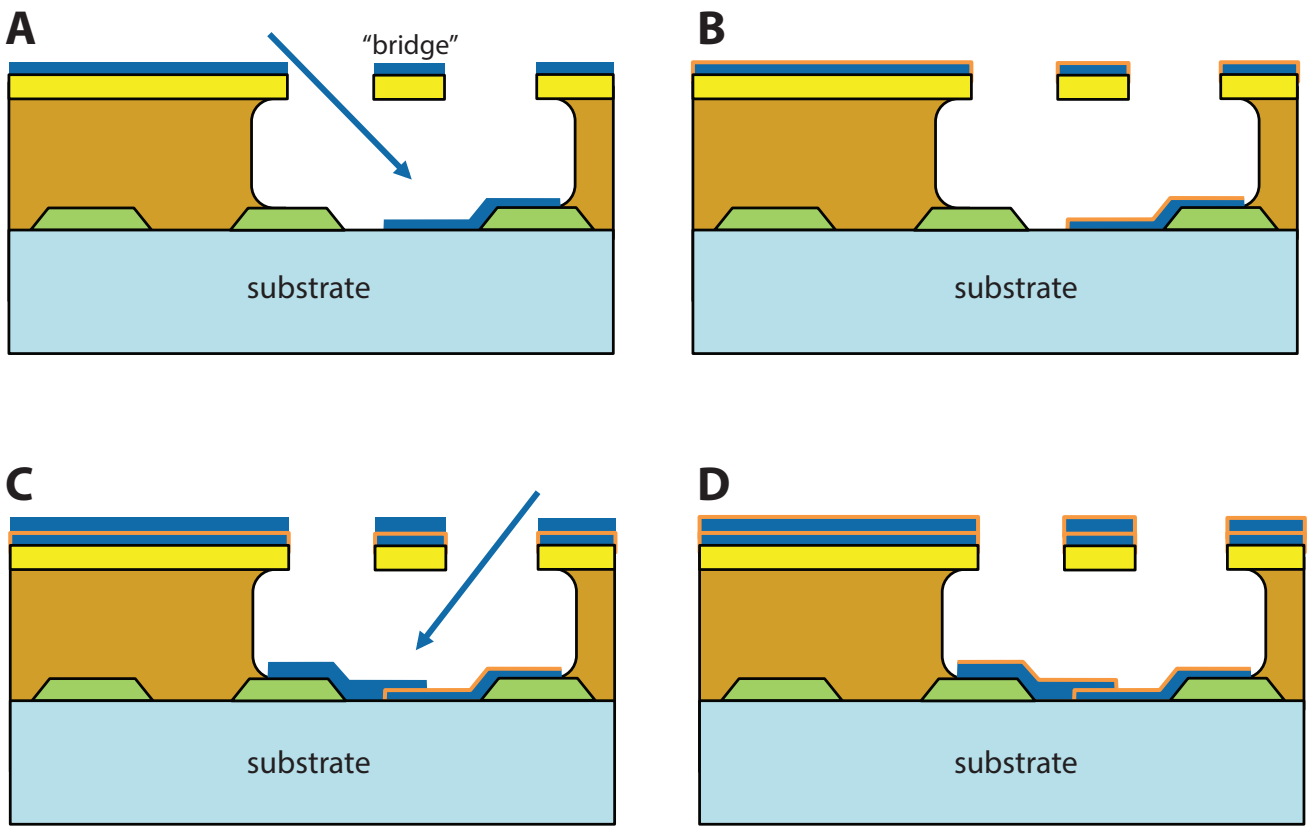

Figure 5.1: Double Angle Dolan Bridge Deposition. In all cartoons, green trapezoids are previously deposited superconducting material that forms the planar resonator or capacitive pads of the transmon. In brown is the MMA resist while the top yellow layer is the PMMA that forms the "bridge". **A** Aluminum, navy, deposition at first angle. **B** Oxidation, orange, of deposited aluminum. **C** Aluminum, navy, deposition at a second angle producing an overlap which forms the Josephson junction. **D** Final oxidation of the Josephson junction in a controlled environment.

5.1.3 Deposition and Dicing

Striplines

All deposition for aluminum stripline resonators were done in the Plassys electron beam evaporator. Depositions were done at a 0° degree angle with respect to the normal at a rate of 1 nm/s for a thickness of roughly 200nm. Full wafer liftoff was done with the sample side facing down in acetone at 75 C for at least an hour (covered), or in NMP at 90 C for at least an hour (covered). Once complete the wafer was coated with S1827 as a protective layer for dicing. It was found, that chips diced to a width of 1 mm were not robust and prone to breaking. However, chips were substantially more robust when diced to widths of 1.2 mm or larger. This minimum width was the driving force behind the stripline chip widths used in chapter 3.

Transmons

All Josephson junction depositions done in this dissertation were in the Plassys electron beam evaporator. For the shadow evaporation process two angles are used and for electrodes of different widths the layering order will alter the Josephson inductance of the device. That is why it is necessary to align the wafer to the deposition system as well as possible before beginning deposition. Once fully setup the Plassys will pump down to the 10^{-8} Torr range before deposition. The first step is a brief titanium sweep to further lower the pressure. A critical first step for depositions done on sapphire is an ion- beam cleaning step

with an Anatech argon ion gun operating at 250 V for 30 s. The first angle deposited is 25 nm of aluminum at a 0° angle with respect to the normal, followed by an oxidation step of 15 Torr of oxygen for 12 minutes (aluminum has a self limiting oxide layer so the time duration need not be exact to 12 minutes), a second deposition of 60nm of aluminum at an angle of 35°, and finally another oxidation at 3 Torr for ten minutes so the final aluminum oxide can be grown under controlled conditions.

Once finished all handling of the wafer and future devices must be done when fully grounded and all wafers and devices in a static dissipative container. Josephson junctions are susceptible to static shock which will ruin the junction and undermine all the work done in creating it. The next step is to lift off the junctions in either acetone at 75 C (covered) for at least an hour or in NMP at 90 C for at least an hour. Once fully lifted off and cleaned, the wafer must be coated with S1827 as a protective layer for dicing.

5.2 Sample Holders

5.2.1 Striplines

The first generation stripline holder in chapter 3 were machined in 6061 aluminum which is roughly 95% aluminum. However, the second generation stripline holders were machined from extruded bars (ingots tend to have air pockets that ruin mill bits and cause the machine shop to be unhappy) of 4N aluminum (99.99% aluminum) purchased through Laurand Associates. The holders were etched according to the process described in appendix A which in Ref. [58] was

shown to improve the internal quality factor of aluminum waveguide cavities.

5.2.2 Cavities

In chapter 6 a two rectangular waveguide cavity sample, which was antenna coupled to a transmon, was machined from high purity (4N) aluminum. The cavities were then etched following the procedure in appendix A which was shown in Ref. [58] to improve internal dissipation of aluminum cavities.

5.3 Experimental Setup

5.3.1 Dilution Refrigerator

The heart of the experiments done in quantum computing and information with superconducting circuits is the dilution refrigerator. All experiments done in chapter 3 and chapter 6 were performed in cryogen free dilution refrigerators which trade the expensive recurring cost of liquid helium for the more reasonable costs of liquid nitrogen, electricity, cooling water, and compressed air for normal operation. In chapter 3 all experiments were performed in an Oxford Triton 200 with a base temperature of 20 mK. All experiments performed in chapter 6 were performed in a Vericold (acquired by Oxford) dilution refrigerator with a base temperature of 20 mK. The Vericold is a bit unusual in that its helium 3 and 4 mixture injection pressure is over 1 bar where as Oxford systems typically have their injection pressure in the .6-.7 bar range.

5.3.2 Vericold Wiring and Filtering

This section is devoted to the description and explanation of the experimental setup used in chapter 6.

5.3.3 Power

Before discussing cavity filtering it is worth briefly what is meant by power in this context. For instance we can define the circulating power inside a cavity in terms of the average number of photons in the cavity $< \overline{n} >$, the energy per photon $\hbar\omega$, and the bandwidth of the cavity, κ as:

$$P =< \overline{n} > \hbar\omega\kappa \tag{5.1}$$

For a cavity with on average one photon at 10 GHz and a linewidth of 1 MHz this corresponds to a power of about -140 dBm. This small amount of power means we must heavily attenuate incoming signals to prevent inadvertent excitation of a cavity (or qubit). In the following sections we will discuss how that is achieved.

5.3.4 Cavity Filtering

The general goal with our filtering is to prevent unwanted and unintended photons from entering in our device and ruining performance. On the input side we attenuate at the "4 K" stage with -20 dB cryogenic safe attenuators and at the base plate with -30 dB attenuators. For most applications we only need

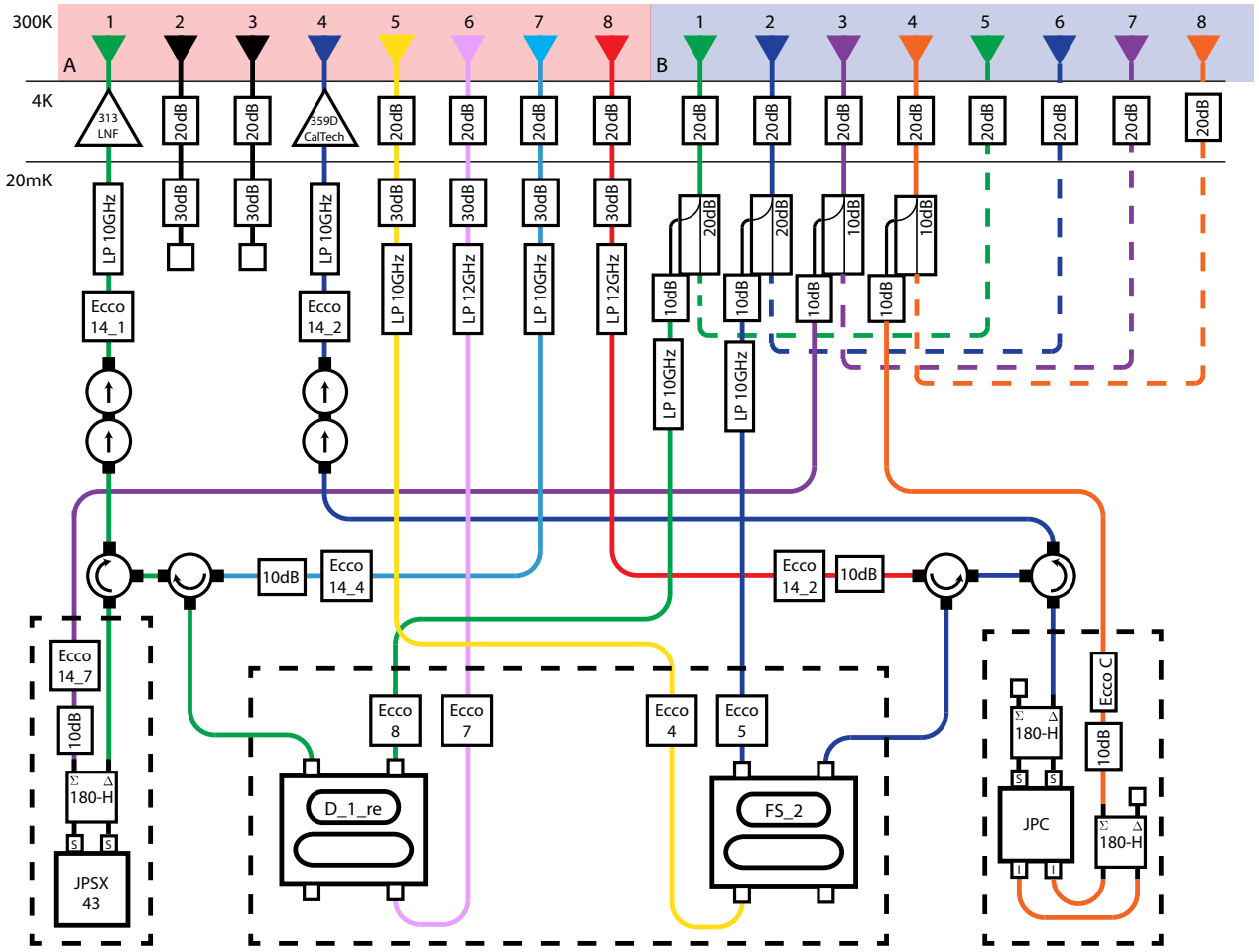

Figure 5.2: Vericold Dilution Refrigerator Wiring. The rectangular two cavity sample labeled FS_2 is the sample used in chapter 6. The other sample, D_1_re, was Reinier Heeres' sample which resulted in Ref. [53]. Following line 5A (yellow) from room temperature, this input line goes through 50 dB of attenuation, a 10 GHz low pass K&L filter, an ecosorb filter and finally to the input port of the storage cavity. The dashed box around the two samples and the ecosorb filters represents the magnetic shield that all reside inside. All parts placed in the shield are measured to be no more magnetic than the baseline of the RSL magnetometer (1mG). The input line for the readout cavity, 2B (dark blue), follows a similar trajectory except for one place that has a directional coupler to lessen the thermal load put on the base plate of the DR when performing the high power Jaynes-Cummings readout (section 5.5.2). The signal from the readout cavity is sent through two microwave circulators, is reflected off of the JPC (which may or may not be operated to produce gain to the signal), sent through two isolators (-20dB of isolation each), travels up niobium inner and outer conducting SMA lines to minimize loss before the Caltech 1-12 GHz HEMT amplifier, and finally up to the room temperature electronics for data acquisition.

a few photons in the 5-10 GHz range— a noteworthy exception is the Jaynes-Cummings high power readout discussed in section 5.5.2 — so the attenuation on the input side is fine as long as the dilution refrigerator has enough cooling power to handle the microwave power dissipated by the attenuators on the base plate. Where things are a bit trickier is on the output side because the signal carrying precious quantum information will also only be a few photons for a dispersive readout (section 5.5.1).

Circulators and Isolators

On the output side between the HEMT at "4 K" and the sample are two PAMTECH/Quinstar 3-12 GHz isolators. These isolators provide -20 dB of directionality to our microwave signals, so two isolators in series, as in figure 5.2 gives -40 dB of isolation from the HEMT at the "4 K" stage. It has been postulated that -40 dB of isolation is inadequate and one of the newer Schoelkopf lab fridges was outfitted with three isolators in series for -60 dB of isolation. No definitive answer exists for whether or not -60 dB of isolation is necessary though an argument can be made in its favor.

In figure 5.2 two PAMTECH/Quinstar 8-12 GHz circulators are used with a Josephson parametric converter (JPC). The two circulators allow for reflection to occur off of the JPC (with or without gain). One port on the first circulator isn't essential and this circulator could be replaced with an isolator. However, the superfluous port is diagnostically useful for measuring and characterizing the JPC independent of the sample. For a circulator to operate effectively,

all incoming ports must be matched. In figure 5.2, the -10 dB attenuator is attached to one circulator to fix the mismatch in impedance between the ecosorb filter and the circulator. Without the attenuator the circulator does not maintain its reverse isolation.

Ecosorb Filters

The ecosorb filters in this thesis serve the purpose of attenuating signals above 20 GHz. The idea behind these filters is to make a transmission line that is filled with a dielectric that is not very lossy in the 5-10 GHz range but whose loss increases as a function of frequency and is very lossy at high frequencies. In this thesis ecosorb filters filled with CR-110 were used to produce the microstrip version of ecosorb filters. A thorough investigation into the different types of ecosorb was undertaken by Geerlings and is available in his thesis [107]. It would seem that the coaxial version of the ecosorb filters is preferable due to its ability to better impedance match to the SMA lines.

K&L Cavity Filters

The K&L cavity filters serve the purpose of rejecting signals from roughly 10-20 GHz. Any resonator will have multiple higher modes especially 3D rectangular waveguide cavities. Typically the fundamental mode of the readout cavity is designed to be around 9 GHz and any higher mode is above 10 GHz. K&L filters prevent noise at the higher mode frequencies from entering the cavity and hopefully minimize the amount of photon shot noise dephasing experienced by the

qubit [63].

Nonmagnetic Components

A more recent point of emphasis in the Schoelkopf group is using measurably nonmagnetic components. The room temperature magnetometer used for all measurements is a 3 axis Bartington Mag-03 (basic model) that can reliably measure down to $\lesssim 1$ mG. Copper inner and copper outer SMA cables are used on the input and output of the sample with hand formable cables being reserved for room temperature setup. All wiring, SMA connectors, and other components are nonmagnetic to the level that can be measured. All components are measured in the Bartington Mag-03 magnetometer at room temperature and only microwave connectors and other components are used inside the sample magnetic shield if the component is not measurably magnetic. Although somewhat tedious to spend an afternoon measuring everything that will be used near the sample the payoff was that devices in the Vericold seemed to have a substantially smaller excited state population after this change as well as longer coherence times.

Magnetic Shielding and Infrared

The magnetic shielding used in the experiments of chapter 6 was initially design by Gerhard Kirchmair. The design is a cylinder made of cryoperm shielding that is then capped with another cryoperm shield. The shield and cap lock into one another and both are thermally heat sunk. Slight variations in size have

progressed over the years. The Vericold dilution refrigerator has the smallest usable sample space and its magnetic shield is small compared to what is used in other Triton systems especially the newer Triton systems which have a large volume that can be connected to the base plate. In the Vericold, both samples were at the very bottom of the magnetic shield and the space above the samples was used for ecosorb filters. Also, inside the magnetic shield is a copper sheet that has been covered with ecosorb and is thermally heat sunk to the baseplate. The copper sheet is to be an absorber of any stray infrared photons that make it into the magnetic shield.

5.3.5 Heterodyne Measurement Setup

All of the quantum measurements performed in chapter 6 used a microwave, heterodyne interferometer (Fig. 5.3). By expanding previous implementations of heterodyne detection in the Schoelkopf group the microwave interferometer is less susceptible to drifts in the experimental setup.

The pulse generation was accomplished with a Tektronix AWG 5014C with a 1 GS/s digital to analogue converter. The signal, typically modulated at 50 or 100 MHz, is then fed into a microwave mixer along with a 5-10 GHz local oscillator tone which is single sideband modulated to achieve the desired pulse shape at the desired frequency. The typical local oscillator used in chapter 6 was a Vaunix LMS-802 generator. For frequency sweeps an Agilent MSG series microwave generator was used. Measurements are recorded with an analog-to-digital converter using the AlazarTech. A full schematic of the setup used in

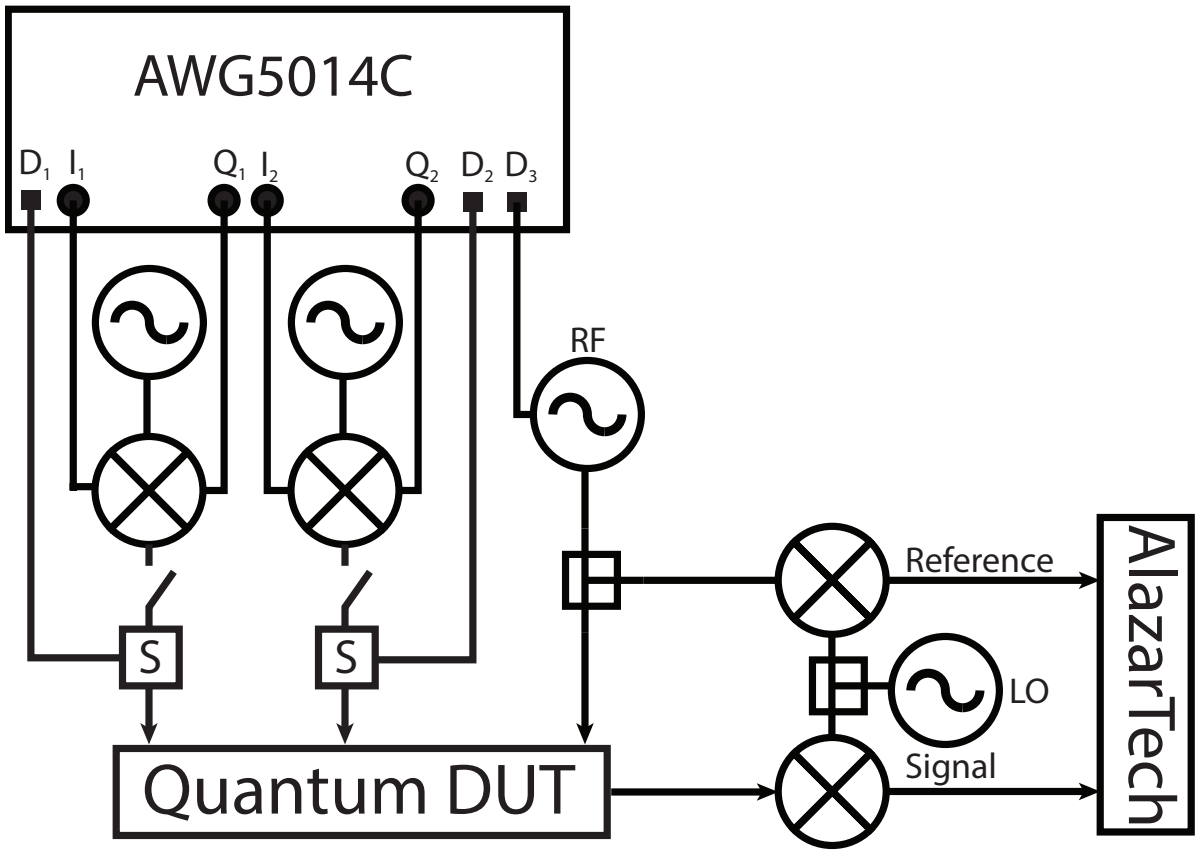

Figure 5.3: Room Temperature Microwave Control and Data Acquisition. Pulse sequences are played along the I and Q DAC channels of the AWG5014C that are then single side band modulated with a local oscillator tone that is 50 or 100 MHz detuned from the desired frequency. Switches, S, are after the mixers and are controlled by the digital channels of the AWG. These switches serve the purpose of preventing leakages from entering the system. The signals controlling the qubit or cavity are sent into the quantum device under test along with the readout, RF, tone. After leaving the QDUT, the signal is then sent into the AlazarTech analog to digital converter along with an earlier reference signal that was broken off before being sent into the fridge. This microwave, heterodyne interferometer robustly protects the measurement apparatus from phase drifts.

chapter 6 is in figure 5.3.

5.4 Cavity Measurement Techniques

5.4.1 Transmission

All cavity measurements performed in chapter 3 measured the magnitude squared of S_{21} in transmission with a vector network analyzer (VNA) where ports 1 and 2 are the input and output ports of the cavity. For the stripline measurements the two ports were designed to be symmetric so it is arbitrary which port is labeled 1 versus 2. A key relation used in chapter 3 was the extraction of the coupling quality factor based on room temperature measurements of the stripline resonators. The following is a derivation that relates the coupling quality factor to the total quality factor assuming symmetric coupling. Another assumption is that the coupling quality factor is much larger than the internal quality factor. For room temperature measurements of aluminum stripline resonators the internal quality factors were ~ 20 whereas coupling quality factors were investigated all above 10^3.

Transmission Coupling Quality Factor–Symmetric

We define the power applied to port 1 as compared to the powered received to port 2 in terms of the scattering matrix element as:

$$|S_{21}|^2 = \frac{P_2}{P_1} \tag{5.2}$$

On resonance $|S_{21}|^2$ is defined as the insertion loss of the device. We will say that the the resonator will have the standard voltage and current relation:

$$I = VG_{tot} \tag{5.3}$$

We can calculate the input power as:

$$P_1 = \frac{I^2}{4G_1} \tag{5.4}$$

The output power will likewise be:

$$P_2 = \frac{I^2}{G_{tot}^2} G_2 \tag{5.5}$$

Using equations 5.4 and 5.5 in equation 5.2 yields:

$$\begin{aligned}
|S_{21}|^2 &= \frac{\frac{I^2}{4G_1}}{\frac{I^2}{G_{tot}^2}G_2} \\
|S_{21}|^2 &= \frac{G_{tot}^2}{4G_1G_2} \\
|S_{21}|^2 &= \frac{Q_1Q_2}{4Q_{tot}^2} \\
|S_{21}|^2 &= \frac{Q_C^2}{4Q_{tot}^2} \\
Q_C &= 2Q_{tot}|S_{21}|
\end{aligned} \tag{5.6}$$

Equation 5.6 gives a simple relation between the coupling quality factor, the total quality factor, and the insertion loss. We assumed in equation 5.6 that the

coupling into and out of the resonator was done symmetrically.

5.5 Qubit Measurement Techniques

Vector network analyzers (VNAs) are terrific for cavity measurements because they have all the necessary microwave electronics in one nice, convenient, user friendly box. An analogous commercially available piece of equipment does not exist yet for measuring qubits. Qubits are trickier in that they require a more flexible input pulse than a continuous wave drive. Also, generally speaking more than one input tone is required for qubit measurements. I will now discuss the two types of readout techniques used in chapter 6.

5.5.1 Dispersive Readout

The first type of readout used in chapter 6 was theoretically developed around the same time of cQED. Initial theoretical work [90] was shortly followed by experimental demonstrations [100] and shown to be quantum non-demolition (QND), even with only a HEMT, in reference [108]. The dispersive readout relies on the qubit and cavity being strongly coupled (Fig. 5.4) albeit well detuned, $\frac{g}{\Delta} < 1$, from each other so that one mode is 'qubit-like' and the other mode is 'cavity-like'. The dispersive interaction in the Hamiltonian can be written in terms of the state dependent shift, χ, between the qubit and cavity, and in terms of the raising $(\mathbf{a}^\dagger, \mathbf{b}^\dagger)$ and lowering operators $(\mathbf{a}, \mathbf{b})$ of the qubit and cavity is:

$$\mathbf{H}_{disp} = -\hbar\chi\mathbf{a}^\dagger\mathbf{a}\mathbf{b}^\dagger\mathbf{b} \tag{5.7}$$

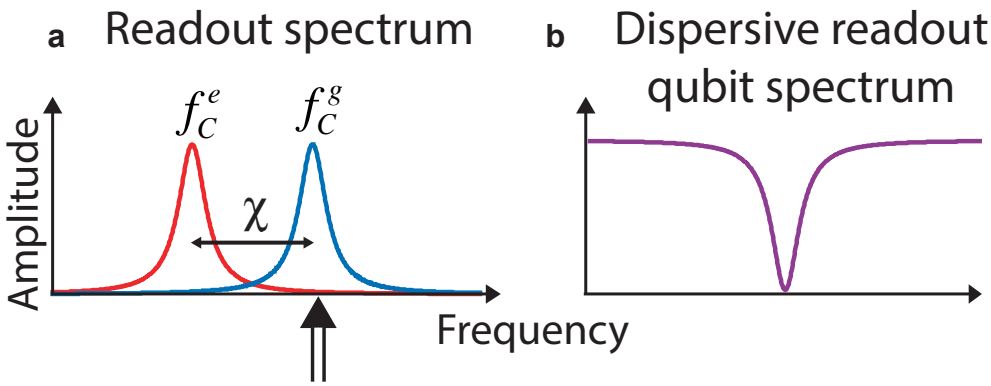

Figure 5.4: Dispersive Readout. A conceptual cartoon depiction of the underlying principles of the dispersive readout. By having a strong, dispersive interaction between the qubit and cavity the frequency of the cavity is dependent on the state of the qubit. **a** The frequency of the cavity is resolvablely different when the qubit is in the ground state, blue, or in the excited state, red. **b** Having the readout tone applied to the cavity frequency corresponding to the qubit in the ground state, double arrow in **a**, allows transmission through the cavity when the spectroscopic tone is not resonant with the qubit. When the spectroscopic tone is applied on resonance with the qubit, the cavity frequency changes and the observed transmitted signal drops.

Due to the qubit-cavity coupling, χ, the resonance frequency of the cavity (or qubit) will be dependent on the state of the qubit (or cavity). By recording the transmission through the cavity one can observe when a second drive is on resonance with the qubit. When the qubit is driven on resonance it will shift the resonance frequency of the cavity and thus lower the transmission through the cavity (Fig. 5.4 **b**). As shown in Fig. 5.4 **a**), the cavity is driven at the peak corresponding to the qubit in the ground state and likewise transmission is observed for that case. However, one could just as well drive at the cavity peak corresponding to the qubit in the excited state. It is up to the experimentalist to decide which cavity peak to drive at and choose accordingly to maximize the signal to noise ratio. Since the dispersive interaction is QND its use with nearly quantum limited amplifiers have demonstrated a variety of novel quantum phenomena [109, 110, 46, 111, 112, 113, 114, 115, 116, 117].

5.5.2 Jaynes-Cummings Readout

An alternative mechanism to readout the state of a qubit was discovered in 2010 using the Jaynes-Cummings interaction between an anharmonic oscillator and a cavity [118]. The unique observation is as follows, by driving very hard at the bare cavity frequency the cavity can fully decouple from the qubit and its high power peak can be resolved. The unique observation is that by having the qubit excited less power is required to drive the cavity to its bright state. This gives a very non-QND method to measure the state of the qubit. The trade off for non-QND measurements is the robust, high fidelity single shot readout for this

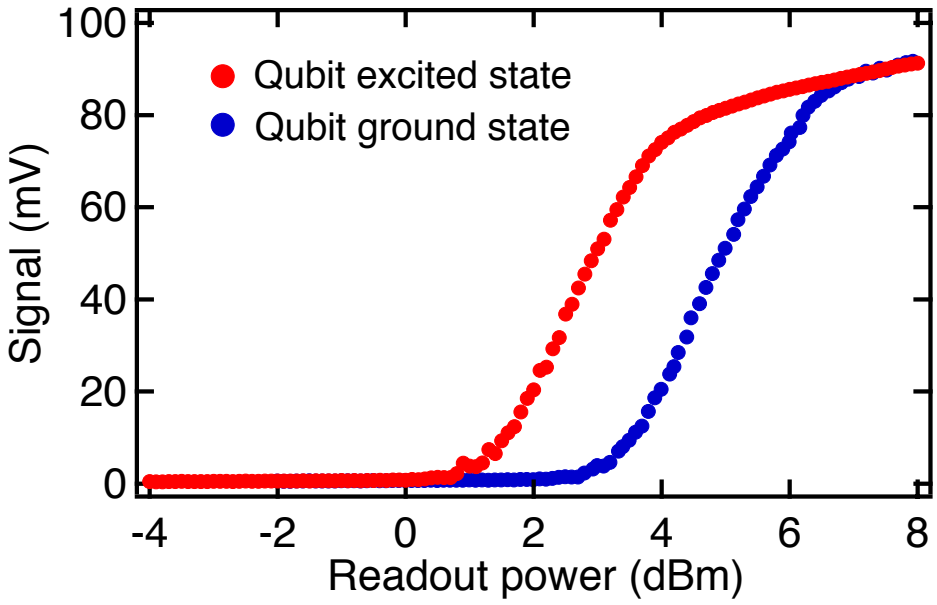

Figure 5.5: Jaynes-Cummings Readout. The observation of Ref. [118] was that for different qubit states, when the readout cavity is driven at its undressed resonance the cavity will decouple from the qubit at different drive powers. In blue is the digitized readout signal as a function of drive power applied to the readout cavity at a fixed frequency when the qubit is in the ground state. In red is the digitized signal for the case when the qubit is in the excited state. When in the excited state the qubit requires less power to make the readout cavity "go bright". By using a power between 1 and 3 dBm a relatively large signal will result from the measurement.

method.

We begin by describing the observed cavity frequency as a function of power. At low powers which correspond to $\overline{n} \approx 1$ one would observe the cavity at its dressed frequency due to the quantum coupling to the qubit as is described in chapter 4. However, as the drive power applied to the readout cavity is increased the frequency of the cavity will begin to lower due to the inherited Kerr nonlinearity from the qubit. At some point when the applied power to the cavity is large enough no longer will one have a cavity response. To put things colloquially the cavity spectroscopically disappears. The innovation by Reed was to not be dismayed by the lost cavity response and to continue to increase the applied power to the cavity. At some very high power the cavity resonance will reappear. This frequency can be thought of as the uncoupled cavity frequency and it occurs much lower in frequency that the low power resonance. The cavity response at high powers is very strong and is why it is occasionally referred to as a bright state.

A further unique observation by Reed, was that one can use this unique bright state as a readout mechanism. By projecting a quantum state onto a classical output this readout scheme has a robust, high single shot fidelity for a wide array of parameters. To readout the qubit state as in Fig. 5.5, one finds that the power required to cause the cavity to go bright when the qubit is in the excited state is less than the power required to make the cavity go bright when the qubit is in the ground state. The disadvantages to this readout mechanism is that it is not QND and requires a longer reset time to repeat a measurement

sequence than a dispersive measurement. For instance, a cavity with a lifetime of order a few hundred nanoseconds would require with the high power readout of order a millisecond or more for the experimental repetition rate where as in a dispersive setup one could use tens of microseconds. The optimal choice for a repetition rate is one that does not negatively impact the coherence nor the performance of the quantum device under test.

6

Cavity State Reservoir Engineering

6.1 Introduction

In this chapter, we undertake the challenge of taming active quantum systems. In the absence of drives, a quantum system will naturally decay to thermal equilibrium with its environment. Regardless of the physical system, the thermal equilibrium state is singular and, at best, serves to initialize the quantum

system to its ground state. A major obstacle for quantum information and quantum computation is that the quantum states used are non-equilibrium states. Non-equilibrium states persistently dissipate entropy to the environment, losing their information. Two well developed methods in combating entropy loss from a quantum system are measurement with external feedback and autonomous protocols with dissipative feedback.

6.1.1 Measurement with External Feedback

This section serves to acknowledge and mention a well studied method for controlling active systems–measurement with external feedback. Theoretical ideas for sequential unitary operations to control open quantum systems predate quantum computing [119]; however, quantum information did inspire further development [120, 121]. Early experimental work lacked the ability for real-time external feedback [122, 123, 124, 125] yet still showed great promise. Proposals for cavity QED protocols that stabilize photon number states, Fock states, required external feedback [126, 127]. Advances in technology allowed a series of experiments by the ENS group [128, 129, 130] to stabilize Fock states in a microwave cavity through repeated measurement and real-time feedback.

The focus of this chapter is the stabilization of Fock states in a microwave cavity through an autonomous protocol with dissipative feedback. Consequently, this chapter will not be an exhaustive review of measurement based feedback. However, it is worth mentioning a few of the advances in the superconducting quantum circuit community made possible by nearly quantum limited am-

plifiers [131, 132, 133, 134, 46]. Noteworthy demonstrations are the realtime monitoring of quantum state decay of either an artificial atom [109] or the cat state of a microwave cavity [111]. Realtime QND observation of quantum state decay opened the possibility of feedback based on the outcome of a measurement. Since several quantum error correction protocols require realtime feedback [135, 136, 137, 138, 139, 140] experimental work demonstrating feedback on a small number of quantum devices exist [114, 115, 112, 116].

6.1.2 Quantum Reservoir Engineering

An alternative approach to active quantum systems is quantum-reservoir engineering (QRE) [141, 142, 143, 144, 145], also refereed to as autonomous state preservation with dissipative feedback, dissipative state production and quantum bath engineering. QRE harnesses persistent, intentional coupling to the environment as a resource. Although it is common for QRE proposals to involve continuous wave drives, proposals [146] as well as experimental implementations [147] using pulsed or stroboscopic drives exist. Both measurement with external real-time feedback as well as QRE require entropy removal. However, only QRE employs environmental losses as a necessary part of its protocols. An advantage to QRE is that it does not require an external feedback with calculation since the Hamiltonian interactions are designed *a priori* to stabilize the subset of a Hilbert space avoiding uncertainty in the quantum-classical interface. Additionally, QRE is less susceptible to experimental noise, such as generator drifts (phase and amplitude), [148] and in some cases thrives in a noisy

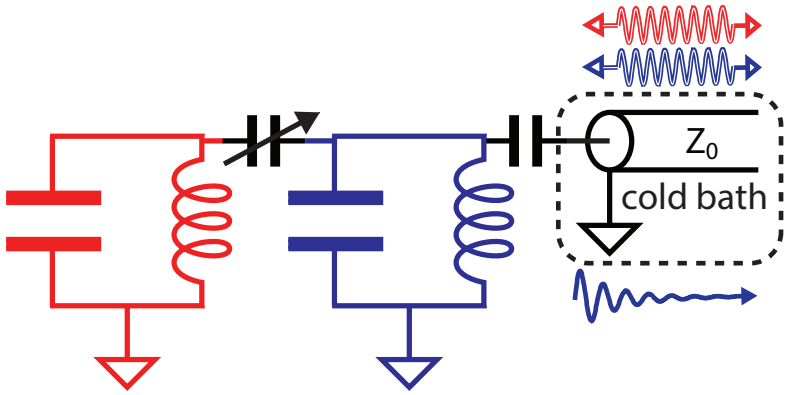

Figure 6.1: In red, a storage cavity is nonlinearly coupled to a cooling cavity, blue, which is strongly coupled to a cold bath (transmission line). Drives applied to the circuit, blue and red double arrows, combined with dissapation, decaying blue arrow, stabilize Fock states in the storage cavity.

environment [149]. QRE is less studied than measurement based protocols with external feedback; however, a few notable examples exist in superconducting circuits. One such example that is relevant to this chapter was performed by collaborators at Yale University in the group of Michel Devoret, who demonstrated a QRE protocol in a cQED environment using a single qubit coupled to a fast cavity [101]. The protocol of choice was the double drive reset of population (DDROP). DDROP was used to cool a qubit that initially had a residual excited state population of $\sim$10% to an excited state population of $\lesssim$ 1%. DDROP is conceptually similar to the protocol shown in figure 6.2 which is used in section 6.7 to stabilize Fock states of a microwave cavity. Other theoretical QRE proposals exist in superconducting circuits [150, 151, 152, 153, 154, 155] and optomechanical systems [153] as well as experimental demonstrations of QRE in both superconducting circuits [156, 157, 158] and trapped atomic ion

systems [159].

6.2 Fock State Stabilization Protocol

We now introduce the major focus of this chapter–stabilizing Fock states of a microwave cavity through quantum reservoir engineering. We intend to have this investigation in QRE be a fruitful endeavor in understanding driven dissipative systems, specifically as applied to cavity modes since the quantum computing paradigm of the Yale group is the cavity centric Cat Code architecture [140]. Stabilizing Fock states appears to be conceptually, theoretically, as well as less resource intensive than the stabilization of a superposition states in a cavity or the stabilization of entangled cavity modes such as entangled cat states.

Shown in Fig. 6.2(b) is a QRE protocol that stabilizes Fock states in a microwave, storage, cavity. Fig 6.2 is drawn with the drives applied so as to stabilize a one photon Fock state in the storage cavity. This protocol which we will refer to as the Fock State Stabilization Protocol (FSSP) is conceptually similar to DDROP [101]. Later in the chapter we will present results demonstrating the stabilization of the vacuum state of the storage cavity, which is analogous to stabilizing the ground state of a qubit, and present a comparisons to DDROP in table 6.2.

Due to the anharmonicity of the storage cavity, a CW drive, ω_{ds} with drive strength Ω_{S}, can be applied to the $f_{\mathrm{s},0\to1}$ transition (Fig. 6.2(a) left). This drive is an induced Rabi rate between vacuum and a one photon Fock state. Concurrently, with ω_{ds}, a drive applied to the cooling cavity at ω_{dc} with strength Ω_{C}

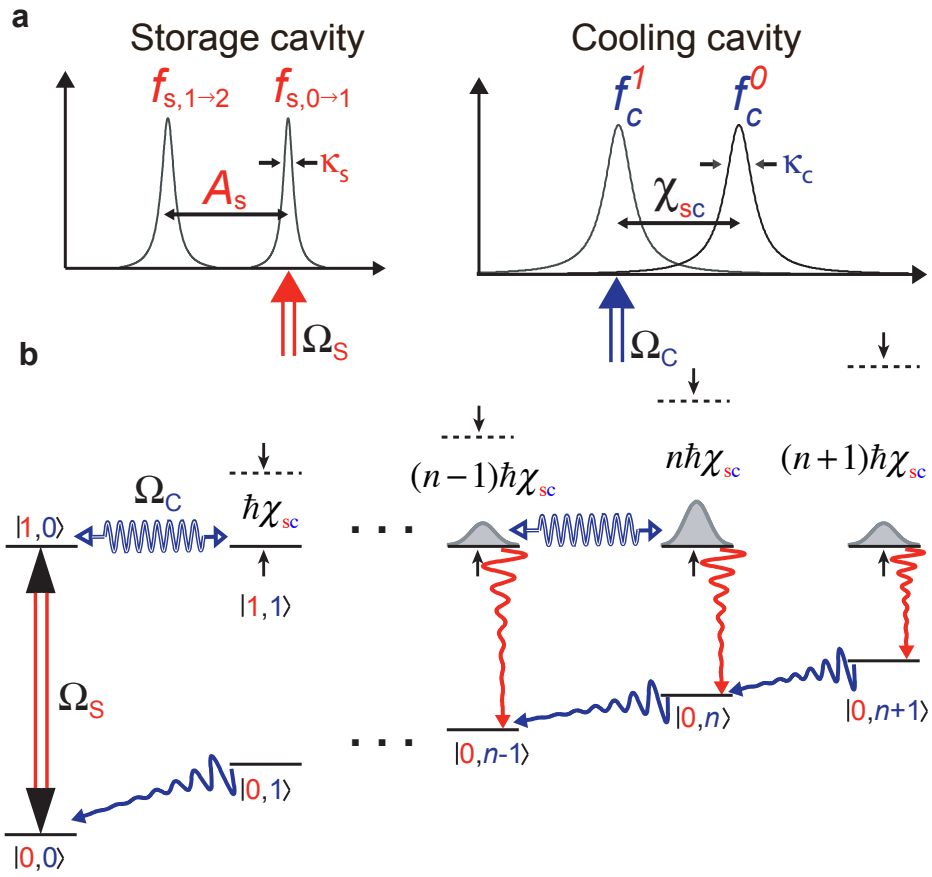

Figure 6.2: Ideal cavity spectrum and Fock state stabilization protocol. (a) Left: sketch of idealized storage cavity spectrum. The storage cavity must have unequal energy levels spacing ($\hbar A_s$), inherited from the coupled qubit, to selectively drive storage cavity transitions. On the right is the idealized cooling cavity spectrum. The frequency shift of the cooling cavity due to photons in the storage cavity, the cross-Kerr (χ_{sc}), must be larger than either cavity linewidth to selectively drive this transition. (b) Energy level diagram for the coupled cavity-cavity system tracing over the qubit state. Ascending vertically are excitations in the storage cavity while to the right is increasing number of excitations in the cooling cavity. A microwave drive, $\Omega_\mathbf{S}$, is applied on the storage cavity so that population only oscillates between vacuum and the first Fock state of the storage cavity. Simultaneously a drive, $\Omega_\mathbf{C}$, is applied on the cooling cavity such that it is resonant provided there is exactly one excitation in the storage cavity. Once resonant, the cooling cavity is pumped to a mean photon number set by the strength of the drive. The autonomous loop of this protocol is closed by cavity decays, decaying arrows, returning the population to $|0,0\rangle$ allowing the preparation to be repeated.

is applied detuned by a cross-Kerr from the cooling cavity, $\omega_{dc} = \omega_c^0 - \chi_{sc}$, (Fig. 6.2 (a) right). This drive is resonant provided that there is exactly one photon in the storage cavity (Fig. 6.2(b)). Once resonant, the conditional drive displaces the cooling cavity to a coherent state determined by the amplitude of the drive. When a photon decays from the storage cavity, Ω_{C} is no longer resonant and the cooling cavity quickly decays to vacuum. Once back to the ground state, the storage cavity is resonant with the drive Ω_{S} and can then be pumped to the target state. This protocol reaches its steady state solution in a time governed by the decay rate of the cooling cavity. The steady state population in the one photon Fock state of the storage cavity will be determined by the storage cavity decay rate, κ_s, and the stabilization rate, $\kappa_\uparrow$. The stabilization rate is defined as the rate at which the system is returned to the target state when a photon decays from the storage cavity. To gain a qualitative understanding of the FSSP potential performance we will investigate a simple four state system to develop physical intuition.

6.2.1 Four State Model

To develop intuition for the expected fidelity of a Fock state produced by the FSSP we investigate a simplified case: a four state system. Figure 6.3 depicts the simplified energy level diagram that will be used to model the FSSP. Starting with the state in the bottom left which is the state with zero photons in the storage and cooling cavity we will label states clockwise as 1 photon in the storage cavity and zero photons in the cooling cavity, 1 photon in the storage cavity

and a coherent state α in the cooling cavity, and zero photons in the storage cavity and a coherent state α in the cooling cavity. Our intention is to stabilize the target state with one photon in the storage cavity and a coherent state of α in the cooling cavity. To determine how well the target state is stabilized an important rate to consider is the rate at which photons decay from the storage cavity ($\kappa_\downarrow$). We will treat $\kappa_\downarrow$ as an external parameter of this system. Specifically $\kappa_\downarrow$ will be an independent variable over which to analyze the FSSP. The other rate that must be determined is the rate at which our system returns to the target state after a photon decays from the storage cavity which we will call the stabilization rate $\kappa_\uparrow$. The stabilization rate will be a combination of the decay rate of the coherent state in the cooling cavity, κ_{DA}, the Rabi rate that the vacuum and first Fock state of the storage cavity is driven at Ω_{AB}, and the rate at which a coherent state in the cooling cavity grows, κ_{BC}. To simplify this model we will call the rate at which the oscillator decays κ and eliminate the subscript "CD". For an oscillator, κ_{BC} is the rate at which a coherent state will grow when driven from vacuum in steady state with $\overline{n} \approx 1$ and consequently this rate is also κ. To recap:

$$\kappa_{\mathrm{DA}} = \kappa_{\mathrm{BC}} = \kappa \tag{6.1}$$

Now we must determine how κ and Ω_{AB} combine to produce $\kappa_\uparrow$. We identify that if either κ or Ω_{AB} are zero then $\kappa_\uparrow$ should also be zero regardless of the

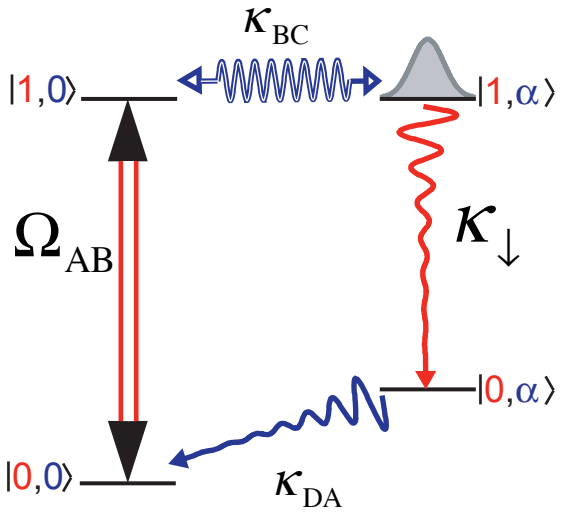

Figure 6.3: Four state system with drives and decay rates.

value of the other rate. For this reason we add the rates in inverse:

$$\kappa_{\uparrow} = \left(\frac{1}{\kappa} + \frac{1}{\kappa} + \frac{1}{\Omega_{\mathrm{AB}}}\right)^{-1} \tag{6.2}$$

The optimal choice is for $\Omega_{\mathrm{AB}} \approx \kappa$ found through an eigenvalue calculation of the matrix modeling for the four state model. With this simplification we find:

$$\kappa_{\uparrow} \approx \frac{\kappa}{3} \tag{6.3}$$

It is at this point that we realize that the decay of our fast cavity (κ) is proportional to the rate at which the system returns to the target state after decaying ($\kappa_{\uparrow}$):

$$\kappa_{\uparrow} \approx \frac{\kappa}{n} \tag{6.4}$$

In steady state we have:

$$\kappa_{\downarrow} P(1) = \kappa_{\uparrow} P(0) \tag{6.5}$$

Solving for $P(1)$ using that $P(1) + P(0) = 1$ we get:

$$P(1) = \left(1 + \frac{\kappa_{\downarrow}}{\kappa_{\uparrow}}\right)^{-1} \tag{6.6}$$

Using equation 6.4 we rewrite $P(1)$ as:

$$P(1) = \left(1 + \frac{\kappa_{\downarrow} n}{\kappa}\right)^{-1} \tag{6.7}$$

In the case of $n = 3$ using equation 6.7, to have a fidelity of 0.99 to the target state a ratio of 300 is required ratio between the decay rate of the cooling cavity, κ, and the decay rate of the target state, $\kappa_{\downarrow}$. With the actual experimental ratio of 25 (section 6.7) from the four state model we expect $P(1) \approx 0.9$ assuming perfect tomography.

6.3 Linblad Master Equation and Simulation

To improve upon the four state model we can use the Linblad equation for our driven, dissipative system. The experimentally realized FSSP Hamiltonian including only cavity terms is:

$$\mathbf{H}/\hbar = \omega_s \mathbf{b}^{\dagger}\mathbf{b} + \omega_c \mathbf{c}^{\dagger}\mathbf{c} - \frac{A_s}{2}\mathbf{b}^{\dagger\mathbf{2}}\mathbf{b}^{\mathbf{2}} - \frac{A_c}{2}\mathbf{c}^{\dagger\mathbf{2}}\mathbf{c}^{\mathbf{2}} - \chi_{sc}\mathbf{b}^{\dagger}\mathbf{b}\mathbf{c}^{\dagger}\mathbf{c} \tag{6.8}$$

Where $\mathbf{b}^\dagger, \mathbf{c}^\dagger$ are the creation operators for the storage and cooling cavity and $\mathbf{b}, \mathbf{c}$ are the annihilation operators for the storage and cooling cavity. In terms of these Hamiltonian parameters the FSSP will work best for $\chi_{sc} > \kappa_c \gg \kappa_s$ and $A_s \gg \kappa_s$ (Fig. 6.2 **a**) . To incorporate continuous wave drives into our Hamiltonian we begin by adding stiff drives of the form $\Omega_{\mathrm{S}}(\mathbf{b}^\dagger + \mathbf{b})$ for the storage cavity drive and $\Omega_{\mathrm{C}}(\mathbf{c}^\dagger + \mathbf{c})$ for the cooling cavity drive. Where Ω_{S} and Ω_{C} are complex drive amplitudes. By including these drives and entering the rotating frame of both cavities ($\mathbf{U_s} = \exp(i\mathbf{b}^\dagger\mathbf{b}\omega_{ds}t)$ and $\mathbf{U_s} = \exp(i\mathbf{c}^\dagger\mathbf{c}\omega_{dc}t)$) the result is detunings of $\Delta_s = \omega_s - \omega_{ds}$ for the storage cavity and $\Delta_c = \omega_c - \omega_{dc}$ for the cooling cavity. We note that ω_{ds} and ω_{dc} are the frequencies of the drives on the storage and cooling cavity respectively. The driven FSSP Hamiltonian is now:

$$\begin{aligned} \mathbf{H}/\hbar = \Delta_s\mathbf{b}^\dagger\mathbf{b} + \Delta_c\mathbf{c}^\dagger\mathbf{c} - \frac{A_s}{2}\mathbf{b}^{\dagger\mathbf{2}}\mathbf{b}^{\mathbf{2}} - \frac{A_c}{2}\mathbf{c}^{\dagger\mathbf{2}}\mathbf{c}^{\mathbf{2}} \\ -\chi_{sc}\mathbf{b}^\dagger\mathbf{b}\mathbf{c}^\dagger\mathbf{c} + \Omega_{\mathrm{S}}(\mathbf{b}^\dagger + \mathbf{b}) + \Omega_{\mathrm{C}}(\mathbf{c}^\dagger + \mathbf{c}) \end{aligned} \tag{6.9}$$

With this driven Hamiltonian the master equation for the open quantum system (with storage and cooling decays of κ_s and κ_c) is:

$$\dot{\rho} = -i[\mathbf{H}, \rho] + \kappa_s D[\mathbf{b}]\rho + \kappa_c D[\mathbf{c}]\rho \tag{6.10}$$

The above master equation is used in QuTIP 2.2 [104] with the steady state solver and the time dependent solver to produce the simulation results that appear in Fig. 6.12(b),(c),(d) and Fig. 6.11(b),(c). The code used for the simulations is found in appendix B. From simulation we find the stabilization rate to

be $\kappa_\uparrow \approx \kappa/9$.

6.4 Measurement Induced Dephasing: Photon Number Calibration

In this section we develop a method for determining the average photon number in a fast cavity. Fast cavities, relative to the quantum object they are measuring, are crucial for repeated quantum measurements [109, 111]. The goal in this procedure is to use the AC stark effect on the qubit as a method of determining the average photon number in a cavity given a room temperature drive strength or in the actual experimental setup the drive power. If the drive is placed at $\omega_d = (\omega_c^g + \omega_c^e)/2$ then our measurement efficiency which is the average I quadrature value, $\overline{I_m}$, divided by its standard deviation, σ, is:

$$\frac{\overline{I_m}}{\sigma} = \frac{1}{T_m}\int_0^{T_m} \sqrt{\eta\kappa T_m |\alpha_g(t) - \alpha_e(t)|^2}dt \approx \sqrt{2\eta\kappa T_m \overline{n}}\sin\left(\frac{\theta}{2}\right) \tag{6.11}$$

Where T_m is the measurement time , η is the quantum efficiency, κ is the decay rate of the cavity, and $\alpha_{e,g}(t)$ is the amplitude of our cavity displacement for either the excited or ground state of the qubit. This integral can be approximately evaluated to give the right hand side which has the average photon number in the fast cavity, $\overline{n}$, as well as the sine of half the angular separation between the cavity coherent states corresponding to the qubit being in the ground or excited state. Since the actual measurement will be average photon number

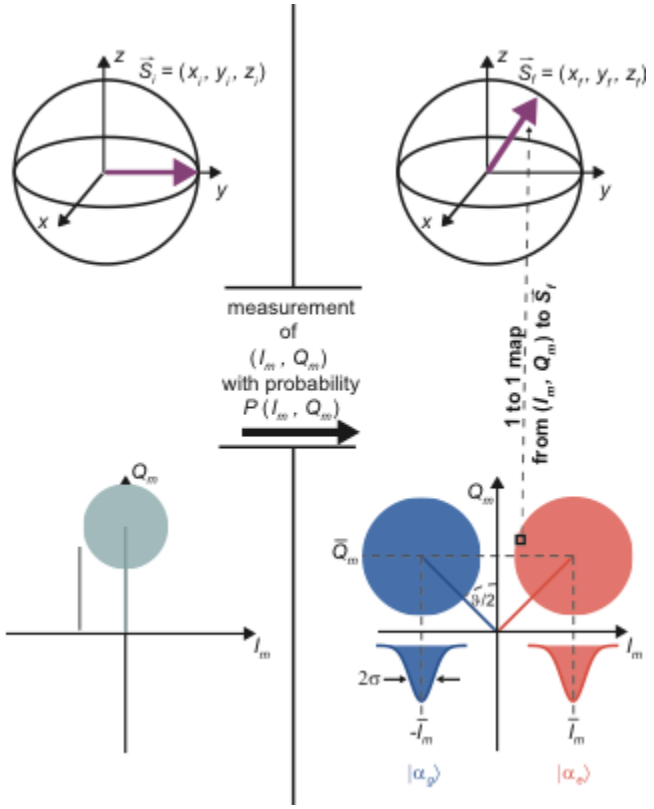

Figure 6.4: Photon Number Calibration via Measurement Induced Dephasing. From Ref. [46], (top) Different qubit states represented on the Bloch sphere. An arbitrary qubit state can be measured with projections along the I and Q quadratures. Each 'g' or 'e' distribution has an associated cavity displacement of $\alpha_g,\ \alpha_e$. The full angular separation between the two distributions is θ and each distribution has a width of 2σ.

we square the above result to get:

$$\left(\frac{\overline{I_m}}{\sigma}\right)^2 \approx 2\eta\kappa T_m \overline{n} \sin^2\left(\frac{\theta}{2}\right) \equiv \Gamma_\phi \tag{6.12}$$

In equation 6.12 we define this quantity as our dephasing rate. We can now use equation 6.12 to express the amplitude of our AC stark measurement, where T is the time between our qubit rotations, as:

$$\begin{aligned} A &= \exp\left(\Gamma_\phi T\right) \\ A &= \exp\left(-2\eta\kappa T_m \overline{n} \sin^2\left(\frac{\theta}{2}\right) T\right) \\ A &= \exp\left(\Gamma T\right) \exp\left(-2\kappa T_m \overline{n} \sin^2\left(\frac{\theta}{2}\right)\right) \end{aligned} \tag{6.13}$$

Since we will be operating in the regime that $\chi \approx \kappa$ we can take the simplification of:

$$\sin^2\left(\frac{\theta}{2}\right) \approx \frac{\chi^2}{\chi^2 + \kappa^2} \tag{6.14}$$

We recognize that equation 6.13 is written in the form of $Ae^{-B\overline{n}}$ with $B = 2\kappa T_m \sin^2\left(\frac{\theta}{2}\right)$. Furthermore the average photon number in the cavity will be proportional to the drive power, P_d, applied to the cavity. So we analogously expect that the amplitude of our response in terms of the drive power, P_d, will be of the form De^{-CP_d}. By relating the arguments of the exponentials ($B = C$) the average photon number in the cavity can be related to the room temperature drive power as:

$$\overline{n} = \left(2\kappa T_m \frac{\chi^2}{\chi^2 + \kappa^2}\right)^{-1} CP_d \tag{6.15}$$

From this expression the only unknown is the constant, C. This constant, along with other measurement parameters, converts room temperature drive power to the average photon number in the cavity. It is quite remarkable that one constant can take into account all the attenuation, intended or otherwise, as well as reflections in the lines. To determine this constant, we perform the procedure in Fig. 6.5a. The first step is a $\frac{\pi}{2}$ qubit rotation around the x axis, a drive on the cavity at ω_d that is long enough so that steady state is reached in the cavity, a wait time which is five times the cavity decay time allowing the cavity to be fully evacuated, and finally a second $\frac{\pi}{2}$ qubit rotation at various angles around the x axis creating oscillations in the measured signal. Fitting the measured oscillation to a sine wave allows the amplitude to be extracted (Fig. 6.5b). Repeating this protocol for different drive powers applied to the cavity allows the amplitude to be plotted as a function of cavity drive power (Fig. 6.6). Figure 6.6 shows the results from several measurements can be fit to an exponential to extract the decay constant (C). By driving at $\omega_d = (\omega_c^g + \omega_c^e)/2$ all of the dephasing information is in the amplitude and not the phase of the oscillation. In our particular setup we found that roughly .24 mW of room temperature drive power was required per average photon in the cooling cavity.

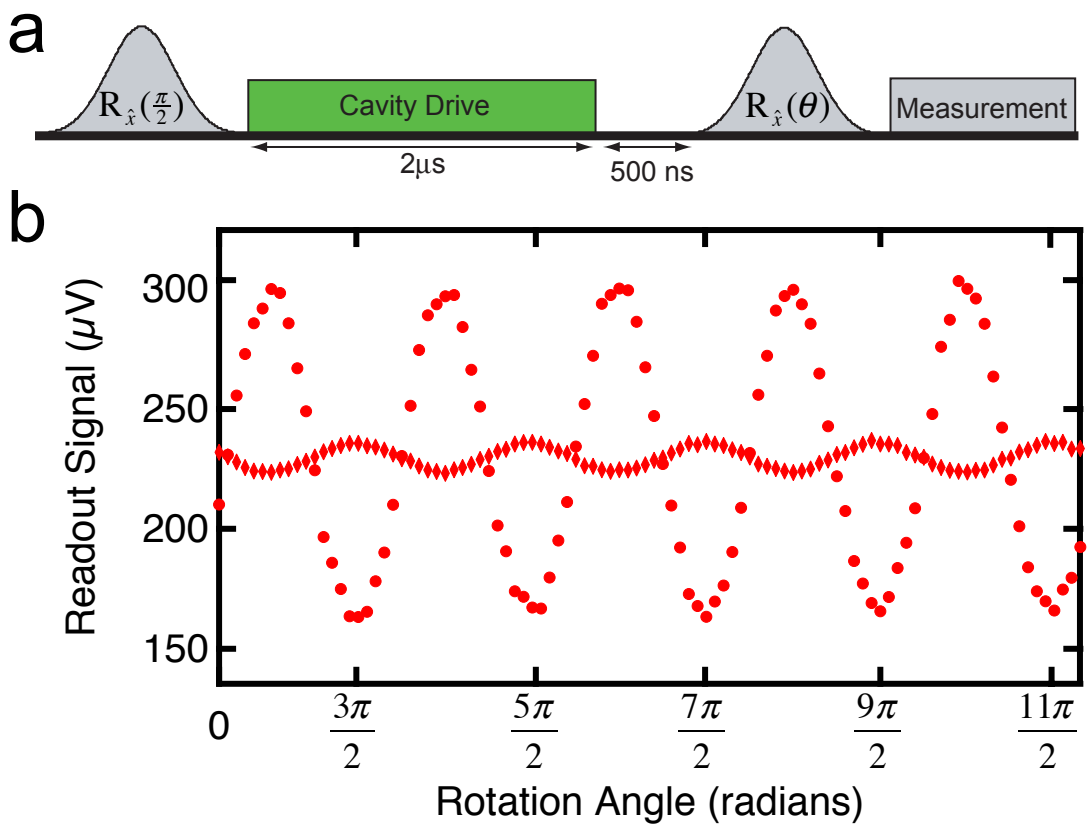

Figure 6.5: Photon Number Calibration Protocol by Measurement Induced Dephasing. (a) A rotation of $\pi/2$ is performed around the x axis of the qubit's Bloch sphere. A cavity drive at $(\omega_c^g + \omega_c^e)/2$ is applied for a duration of two microseconds ($\kappa_c^{-1} \approx 100$ ns) allowing the cavity to reach steady state. The drive is then turned off, the cavity fully evacuates and a final $\pi/2$ is performed at various angles with respect to the x axis. Varying the angle of the pulse creates oscillations of the qubit state between 'g' and 'e'. (b) Representative data showing oscillations due to variations in the second qubit rotation. In red circles are the result of a measurement with a weak drive strength and in red diamonds are the result of a measurement with larger drive strength. The full plot of amplitude versus applied power is in Fig. 6.6.

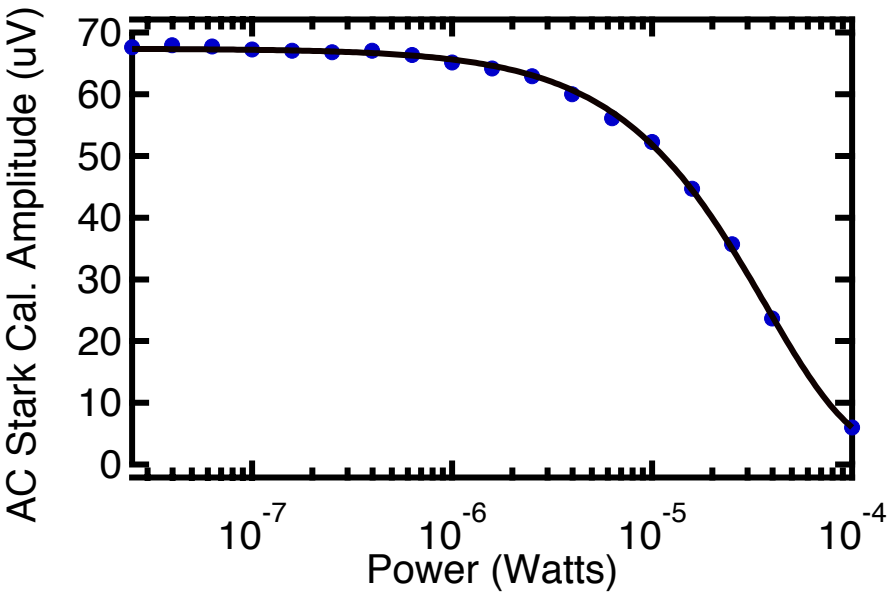

Figure 6.6: Photon Number Calibration by Measurement Induced Dephasing. The protocol from Fig. 6.6 (a) is performed to extract the amplitude of the observed oscillation. Several experiments are performed with varying cavity tone drive powers and the extracted amplitude is plotted as a function of that drive power. By fitting the data to an exponential the constant C is found and used in equation 6.15 to determine the drive power corresponding to on average one photon being in the readout cavity.

6.5 Determining the Parameters of the FSSP Hamiltonian

In this section we will describe in detail the measurement of the two most important Hamiltonian for the FSSP- the storage cavity anharmonicity, A_s, and the cavity-cavity cross-Kerr, χ_{sc}. From the previous sections we gained the insight that the requirements for the FSSP are: that the ratio of lifetimes between the cooling cavity and storage cavity must be large, that the storage cavity must be anharmonic enough such that individual transitions can be selectively driven, and that the cooling cavity be reasonably linear to avoid photon blockade. The cooling cavity will inevitably have a non-negligible inherited nonlinearity because it is necessary for the cross-Kerr term to be larger than the linewidth of the cooling cavity.

The full Hamiltonian of the qubit (transmon) coupled to two cavities includes frequencies (ω_i), anharmonicities (A_i), and state dependent shifts (χ_{ij}) for all the discrete modes involved as:

$$\begin{aligned} \mathbf{H}/\hbar &= \omega_q \mathbf{a}^\dagger \mathbf{a} + \omega_s \mathbf{b}^\dagger \mathbf{b} + \omega_c \mathbf{c}^\dagger \mathbf{c} \\ &\quad - \frac{A_q}{2} \mathbf{a}^{\dagger 2} \mathbf{a}^2 - \frac{A_s}{2} \mathbf{b}^{\dagger 2} \mathbf{b}^2 - \frac{A_c}{2} \mathbf{c}^{\dagger 2} \mathbf{c}^2 \\ &\quad - \chi_{qs} \mathbf{a}^\dagger \mathbf{a} \mathbf{b}^\dagger \mathbf{b} - \chi_{qc} \mathbf{a}^\dagger \mathbf{a} \mathbf{c}^\dagger \mathbf{c} - \chi_{sc} \mathbf{b}^\dagger \mathbf{b} \mathbf{c}^\dagger \mathbf{c} \end{aligned} \tag{6.16}$$

6.5.1 Measuring Inherited Anharmonicities

In cQED systems the cavity anharmonicity is not an innate feature of the cavities but rather is an inherited nonlinearity from the qubit [102]. A large, inher-

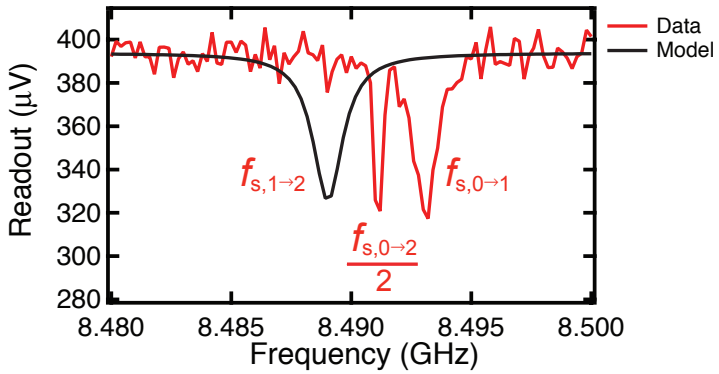

Figure 6.7: Storage cavity spectra. Spectroscopy is performed on the storage cavity with a single CW drive. With a large amplitude drive, we observe the two photon transition, $\frac{f_{s,0\to2}}{2}$. From this measurement we infer the location of the $f_{s,1\to2}$ transition (black line) and determine its detuning from the $f_{s,0\to1}$ transition as 4.0 MHz which we define as the anharmonicity of the storage cavity.

ited nonlinearity was necessary for the observation of coherent revivals due to the self-Kerr (anharmonicity) of a cavity [160]. For the FSSP, the anharmonicity must be much larger than the cavity linewidth ($A_s \gg \kappa_s$) so that the applied microwave drives can selectively address individual transitions of the storage cavity. Large anharmonicities are not universally desirable. To combat undesired inherited nonlinearities discrete as well as CW protocols have been demonstrated [53, 51, 50].

To measure the storage cavity anharmonicity, a single CW drive is used for spectroscopy (Fig. 6.7) with a dispersive measurement (measurement tone applied at the cooling cavity peak corresponding to zero excitations in the storage cavity). A large amplitude drive applied to the storage cavity power broadens the $f_{s,0\to1}$ transition ($f_i = \omega_i/2\pi$), and we observe the two photon transition at

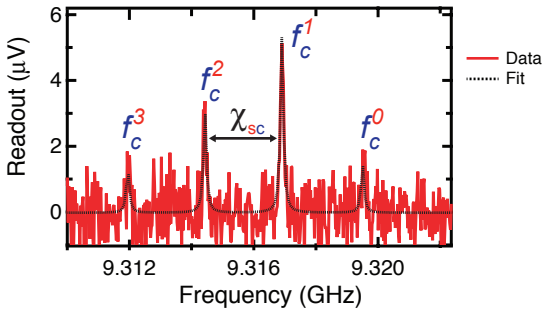

Figure 6.8: Cooling cavity spectra. A 5 ns displacement pulse, whose amplitude gives $\overline{n} \approx 1.5$ in the storage cavity, enables the observation of a single photon resolved cross-Kerr between the two cavities, $\chi_{sc}(2\pi)^{-1} = 2.59 \pm .06$ MHz.

a frequency of $\frac{f_{s,0\to2}}{2}$. The detuning between the two photon transition and the $f_{s,0\to1}$ corresponds to half the anharmonicity, $A_i = A_i/2\pi$, of the storage cavity and we infer an inherited cavity anharmonicity $A_s = 4.0$ MHz. Following the same method, we determine $A_c = 300$ kHz (cooling cavity anharmonicity) and $A_q = 26.1$ MHz (qubit anharmonicity). The cooling cavity anharmonicity was measured in this fashion when it was weakly coupled to the 50 Ω environment and had a linewidth of 33 kHz. During the FSSP when the cooling cavity linewidth was large (1.7 MHz) its anharmonicity was verified by performing the AC stark calibration of section 6.4 so that the single photon power was known and then extracting the cooling cavity anharmonicity by tracking its resonance frequency as a function of drive power applied to the cooling cavity.

6.5.2 Single Photon Resolved Cavity-Cavity Cross-Kerr

In this section, measurements of the state dependent shift between the storage, cooling, and qubit modes are undertaken. The state dependent shift between

two coupled cavities was predicted to be be measurable [161] and the observation of this state dependent shift is a new results. Each mode is excited sequentially, rather than concurrently since off resonant drives result in larger than actual state dependent shifts [162]. To measure the state dependent shift between the two cavities, we first perform a 5 ns square pulse which displaces the state of the storage cavity, then a 2 μs square pulse on the cooling cavity, and finally high-power readout on the cooling cavity which relies on the anharmonicity of the cooling cavity for discernible signal based on the state of the storage cavity [118]. Shown in Fig. 6.8 is a spectroscopic measurement of the cooling cavity for a storage cavity displacement of $\overline{n} \approx 1.5$. Discrete spectral peaks for up to three photons in the storage cavity are visible. From this we infer a state dependent shift $\chi_{sc}/2\pi = 2.59 \pm .06$ MHz and observe the first single photon resolved cavity-cavity cross-Kerr.

A similar method is used to measure the state dependent shift, χ_{qs} between the qubit and the storage cavity. We apply a 5 ns square pulse which displaces the state of the storage cavity, a 2 μs square pulse on the qubit, and perform high-power readout on the cooling cavity which relies on the anharmonicity of the transmon for a readout signal. To measure the state dependent shift, χ_{qc}, between the qubit and the cooling cavity we use a slightly different approach because of the short lifetime of the cooling cavity. Instead we perform a $\pi/2$ pulse on the qubit, then a 2 μs square pulse on the cooling cavity, and finally high power readout on the cooling cavity. In summary we find our Hamiltonian parameters ($\widetilde{\chi}_{ij} = \chi_{ij}/2\pi$, $\mathrm{A}_i = A_i/2\pi$) to be:

Term	Measured Value	Simulation Prediction	Units
f_q	$7249.46 \pm .01$	7221	MHz
f_s	$8493.73 \pm .02$	8564	MHz
f_c	$9320.11 \pm .02$	9346	MHz
A_q	$26.1 \pm .3$	25.9	MHz
A_s	$4.0 \pm .1$	3.7	MHz
A_c	300 ± 80	240	kHz
$\widetilde{\chi}_{qs}$	$21.1 \pm .1$	19.8	MHz
$\widetilde{\chi}_{qc}$	$4.9 \pm .1$	4.2	MHz
$\widetilde{\chi}_{sc}$	$2.59 \pm .06$	2.2	MHz
κ_s	65 ± 5	—	kHz
κ_c	$1.7 \pm .1$	—	MHz

Table 6.1: FSSP Hamiltonian parameters as well as the predicted parameters from a BBQ simulation. The initial CAD drawings in HFSS were from the designs sent to the machine shop that manufactured the aluminum cavities. The HFSS drawings of the 3D cavities were then adjusted to match up with room temperature measurements of the bare 3D cavities with a vector network analyzer. The same design file used for the lithography of the qubit was imported into HFSS and only a small ($\sim$1 μm) section was removed to insert a port to measure the impedance seen by the junction as well as a linear inductor boundary condition that was a few nanohenries. The predicted values are quite close to the measured values and the major sources of error are machining tolerances, thermal contractions, and alignment of the vertical transmon to the machined structures.

6.6 Photon Number Selective π Pulse Calibration

From table 6.1 we see that the necessary relations for the FSSP are satisfied ($\chi_{sc} > \kappa_c \gg \kappa_s$ and $A_s \gg \kappa_s$). However, we must develop the tools necessary for cavity state tomography to measure the target state of the FSSP. First we require photon number selective π pulses on the different resonance frequencies of the qubit which are dependent on the number of excitations in the storage cavity (${f_q}^n \approx {f_q}^0 - n\chi_{qs}$). To calibrate these π pulses multiple cavity displacements are performed allowing the measurement of Rabi oscillations for each of the different photon number peaks of the qubit. Due to the large state dependent shift between peaks (21 MHz), each qubit transition will require a different drive amplitude for a full π pulse due to mixer nonlinearities as well as increased filtering due to detuning further from the cooling cavity (all qubit excitations are driven through the cooling cavity). We find that each subsequent transition requires roughly 10% larger amplitude than the previous transition. Once the π pulses for each photon number peak are calibrated a good check is to perform cavity displacements on the storage cavity and measure the photon number distribution (Fig. 6.9). For each displacement, the photon number distribution should be Poissonian. From this set of measurements we have a collection of background subtracted raw data that in Fig. 6.9 is plotted versus AWG DAC amplitude for the 5 ns displacement pulse. With these five traces we perform a global fit on the traces which gives not only the y scaling, photon number probability, but also x scaling, root photon number. We can see from Fig. 6.9 that for

larger cavity displacements ($\overline{n} \gtrsim 2$) there will be non-negligible uncertainty in the results. However, for smaller average photon numbers ($\overline{n} \lesssim 2$) in the storage cavity we can reliably measure the photon number distribution. The difficulty in measuring the Poissonian photon distribution for larger average photon numbers is due to the large cross-Kerr saturating the readout mechanism.

6.6.1 Estimating π Pulse Selectivity

In this section we seek to estimate the selectivity of the π pulses used on the qubit. In this context selectivity is used to describe how well only the intend transition is excited. To estimate the selectivity, S, of our π pulse we use the following [163]:

$$S = \left(1 + \frac{\pi}{8} \exp\left(-(\chi_{qs}/\sigma_w)^2\right)\right)^{-1} \tag{6.17}$$

Here we assume a gaussian pulse with spectral width σ_w and spectral peak spacing of χ_{qs}. In our particular case, χ_{qs} is the state dependent shift between the qubit and the storage cavity but in general this is just the spacing between the different photon number peaks. From eq. 6.17 the estimated selectivity of our π pulses ($\chi_{qs} = 21.1$ MHz and $\sigma_w = 4$ MHz) for the different photon number peaks is no worse than .999. We experimentally investigate the contribution to π pulse selectivity by applying a gaussian π pulse on the $N = 0$ and measuring the population in the $N = 1$ photon peak and find that our induced transition is no worse than .3%, a bound limited by averaging.

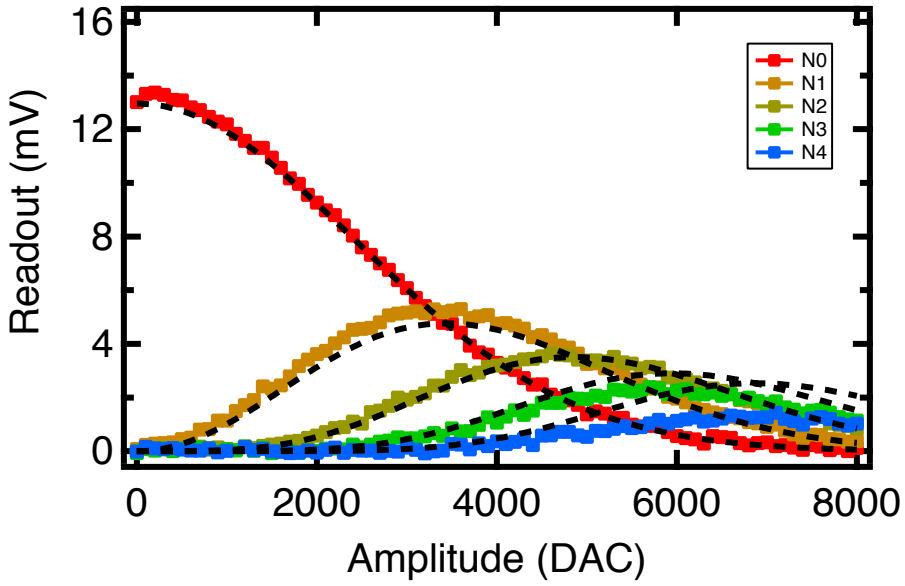

Figure 6.9: Photon number selective π pulse response versus room temperature displacement amplitude. Measurement of the different photon number peaks of the qubit as a function of displacement amplitude. Photon number peaks of the transmon qubit due to the storage cavity are measured up to N=4. The data is background subtracted (a sequence that is a cavity displacement with no π pulse) and plotted as a function of AWG DAC value for the amplitude of the 5 ns displacement pulse. A global fit is performed on the entire set of measurements determining the x scaling, root photon number, and y scaling, probability. We attribute the difficulty in measuring higher photon numbers to the saturation of our readout mechanism due to the large, direct cross-Kerr interaction.

6.7 Fock State Stabilization Protocol

Shown in Fig. 6.2(b) is the QRE protocol we will use to stabilize Fock states in the storage cavity. This protocol is conceptually similar to the protocol used in Ref. [101] which stabilized the ground state of a qubit tensor product with a coherent state of a cavity. The FSSP in some sense generalizes DDROP allowing the physicist to not only stabilize the vacuum state but also any exact excitation number for a small number of excitations. In this section we will present results stabilizing not only the zero photon Fock state of the storage cavity but also the first Fock state of the storage cavity.

To implement the FSSP the frequencies of the two microwave drives and their amplitudes must be chosen judiciously. For the drive applied to the storage cavity we find optimum performance both experimentally and in simulation for a drive strength of $\Omega_{\mathrm{S}} \approx \kappa_{\mathrm{c}}$. In figure 6.10, the storage cavity drive is resonant with the $f_{s,0\to1}$ transition with drive strength $\Omega_{\mathrm{S}} \approx \kappa_{\mathrm{c}}$. Since the cooling cavity is weakly anharmonic we expect that its frequency will change dependent on its average photon number.

In figure 6.10 (a) is the pulse scheme used to implement and characterize the FSSP. Continuous wave drives are applied to the storage cavity and the cooling cavity for a duration that is two hundred times longer than κ_c which is the rate at which steady state will be reached. Furthermore, this pulse duration is roughly ten times longer than the decay time of the storage cavity meaning that any steady state achieved through the FSSP has overcome the internal decays

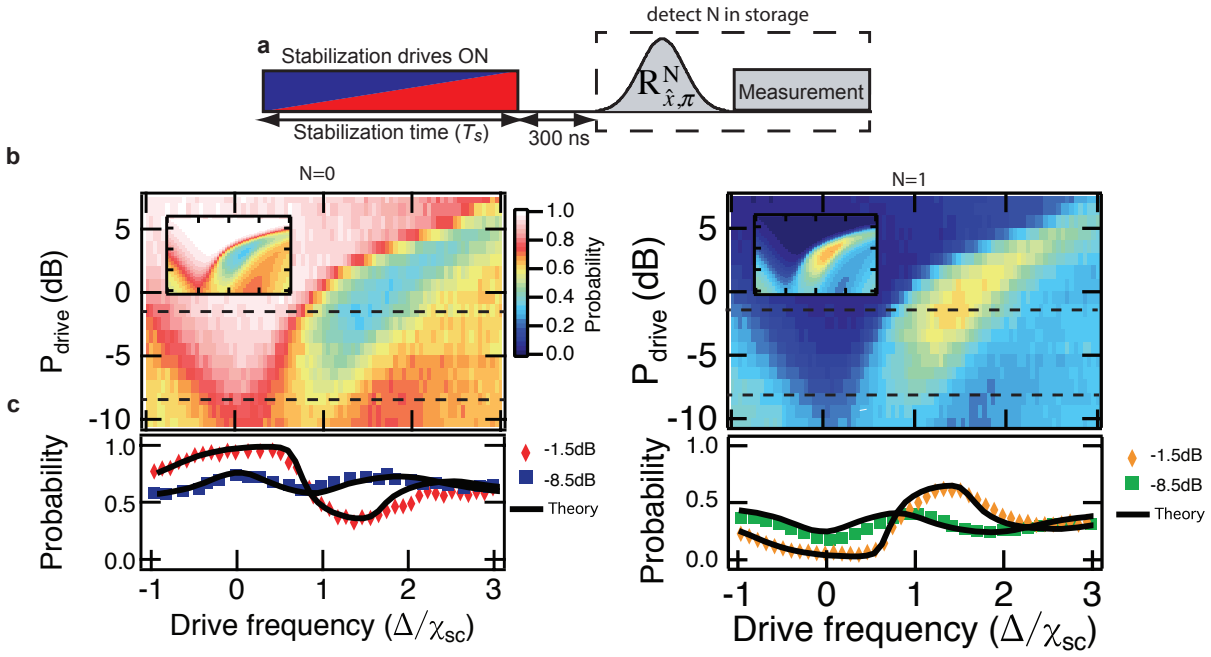

Figure 6.10: Photon number probabilities of the zero and one photon Fock states from the FSSP. (a) The Fock state stabilization protocol described in Fig. 6.2(b) is applied for a duration, T_s, followed by a 300 ns wait to evacuate excitations from the cooling cavity, a photon selective π pulse is then performed on the qubit determining the probability of each photon state of the storage cavity up to three photons. (b) Storage cavity photon number probability (N=0 left and N=1 right) as a function of drive amplitude and frequency. The frequency of the cooling cavity drive is plotted as $\Delta = \omega_c^0 - \omega_{\rm dc}$, and normalized by the cross-Kerr, $\chi_{\rm sc}$. As the frequency of the drive applied to the cooling cavity is brought in resonance with the first photon peak of the storage cavity $^{\Delta}/\chi_{\rm sc} \approx 1$ the protocol stabilizes the first Fock state of the storage cavity. The inset is a simulation plot with the same axis and color scale as the experimental result. (c) Linecuts (dashed lines in part b) for a weak drive power and a drive power resulting in stabilization.

of either cavities. Next a wait time of 300 ns wait time follows the long pulses so that fast photons can leak out of the cooling cavity. Finally photon number selective π pulses ($\sigma_t = 40$ ns) are applied to measure the photon number probability distribution. In figure 6.10(b,c) the frequency of the storage drive is held fixed at the $f_{\mathrm{s},0\to1}$ transition with a drive strength roughly equal to κ_c. The parameters swept in figure 6.10 are the drive strength of the cooling drive, which alters the size of the coherent state the cooling cavity is conditionally displaced to, as well as the drive frequency applied to the cooling cavity which determines whether the zero or one photon Fock state of the storage cavity is stabilized. The drive strength applied to the cooling cavity is calibrated via the AC Stark dephasing method described in section 6.4. The drive frequency is plotted as a detuning, $\Delta = \omega_{\mathrm{c}}^0 - \omega_{\mathrm{dc}}$, and normalized by the cross-Kerr, χ_{sc}. The drive frequency on the cooling cavity is normalized by the cross-Kerr to illustrate that at about one cross-Kerr, with a sufficiently strong drive, a one photon Fock state is stabilized. Since the cooling cavity is weakly anharmonic maximum stabilization of the first Fock state of the storage cavity will not happen for $\Delta = \chi_{sc}$ but will happen at a lower frequency and therefore a larger detuning. From simulation, we expect on average four photons will be in the cooling cavity for maximum stabilization of the first Fock state of the storage cavity. Four photons in the cooling cavity with an anharmonicity of 300 kHz corresponds to the extra half cross-Kerr observed in figure 6.10. This explains why maximum stabilization for the first Fock state occurs for $\Delta \approx 1.5\chi_{sc}$. From the linecuts in figure 6.10 we see that for a sufficiently strong drive strength on

	DDROP	**FSSP**
Vacuum Stabilization	0.993 ± 0.005	0.96 ± 0.03
$\kappa_c \big/ \kappa_{(q,s)}$	700	25
$A_{(q,s)} \big/ A_c$	3000	15
$\chi_{(q,s)c} \big/ \kappa_c$	2.3	1.5

Table 6.2: Comparison FSSP and DDROP. As can be seen from this table the implementation of DDROP produced a more pure system reset than the FSSP experiment. The difference in state preparation is due to in the DDROP experiment having an order of magnitude larger difference in decay rates than in the FSSP experiment. As expected, in simulation with a comparable ratio of lifetimes the FSSP would produce results nearly indistinguishable from DDROP.

the cooling cavity that we can either stabilize a zero or one photon Fock state of the storage cavity solely as a function on the placement of the cooling cavity drive. We define the probability of getting exactly N photons in the storage cavity as $P(N)$ and measure probabilities for $N = 0$ to $N = 3$. At the optimum parameter selection for the cooling cavity drive we stabilize vacuum of the storage cavity with $P(0) = 0.96 \pm 0.03$ and stabilize the one photon Fock state with $P(1) = 0.63 \pm 0.02$.

6.7.1 Comparison DDROP and FSSP

In table 6.2 a direct comparison is made between the results of DDROP and the FSSP when stabilizing the ground state of a qubit or in the case for the FSSP a microwave cavity. Although the FSSP did not outperform DDROP it is not a truly 'apples' to 'apples' comparison which is shown in the remaining lines

in table 6.2. The predominant reason for DDROP out performing the FSSP is due to the larger ratio of lifetimes in the DDROP experiment. Other parameters, such as the linearity of the cooling cavity as well as the separation of photon number peaks matter weakly in this comparison. Although if higher photon numbers were stabilized these parameters would matter more.

6.7.2 Steady State Wigner Function for Stabilized N=1 Fock State

In this section we characterize, through a measurement of the Wigner function, the larger than 2 bit Hilbert space of the stabilized system to confirm that the stabilized state is indeed a nonclassical cavity state. In Fig. 6.11 (a) we perform cavity tomography after the FSSP measuring generalized Husimi Q functions [160] defined as:

$$Q_N(\alpha) = \frac{1}{\pi} |\langle N| D_{-\alpha} |\Psi\rangle|^2 \tag{6.18}$$

$D_{-\alpha}$ is the displacement operator, and $|\Psi\rangle$ is the final state. In our case $|\Psi\rangle$ will be the steady state to the FSSP. Although the zeroth Husimi Q function entirely describes the state of the oscillator we measure generalized Husimi Q functions up to $N = 3$ Fock state of the storage cavity so that we can infer the Wigner function. By adding and subtracting the even and odd measured Q functions the Wigner function is:

$$W(\alpha) = \frac{2}{\pi} \sum_{n=0}^{\infty} (-1)^n Q_n(\alpha) \tag{6.19}$$

The Wigner function is measured in this manner because of the large state de-

pendent shift, χ_{qs}, between the qubit and the storage cavity. The preferred method to measure a Wigner function directly measures photon number parity. Measuring photon number parity directly requires π pulses which are not photon number selective. For instance, a π pulse with $\sigma_t = 5$ ns gives a spectral width of roughly 32 MHz which for a qubit-cavity state dependent shift of 21 MHz is insufficient. In cases with large state dependent shifts, it is necessary to measure the generalized Husimi Q functions. Since it is not practical to measure all the Husimi Q functions a truncation must be made. This truncation could result in a halo effect in the Wigner function. Although a small effect, one can see that in figure 6.11 (b) that on the corners of the Wigner function the measurements are skewed towards negativity (red). By comparing the measured Wigner function to a simulation of the steady state solution to the FSSP when stabilizing a one photon Fock state the negativity at the origin in our Wigner function is a real result and not due to the slight bias in our measurement from the last Fock state included in the truncated sum being an odd number (ending on an even Fock state would give a slight positive bias).

As can be seen in figure 6.11(b,c) the harmonic oscillator picture describes the steady state of the storage cavity as a statistical mixture of $P(0) = 0.37 \pm 0.03$ and $P(1) = 0.63 \pm 0.02$ with no statistically significant population in the $N = 2, 3$ states. In Fig. 6.11 c statistically significant negativity in the Wigner function is observed. With harmonic oscillators Wigner functions are often shown since negativity in the Wigner function indicates a quantum state. What is quite special here is that we observe negativity in the Wigner function

for arbitrarily long stabilization times. In this case the stabilization protocol was run for ten times the storage cavity lifetime. Without the FSSP the storage cavity would have fully decayed in that amount of time.

6.7.3 Interpreting Results as a Spin System

Since the results of the FSSP have the storage cavity limited to its first two Fock states, we can recast our results in a way analogous to a spin system. The figure of merit will be the polarization, p defined by $p = \frac{P(0)-P(1)}{P(0)+P(1)}$. As a thought experiment imagine a spin system with many spins in a magnetic field B that is in thermal equilibrium with a bath at temperature T. At zero Kelvin, we expect the spin system to overwhelmingly be aligned with the external magnetic field since the bath cannot provide the energy necessary to align against the magnetic field. However, as the temperature of the bath is increased thermal fluctuations provide individual spins with the necessary energy to align against the magnetic field. As infinite temperature is approached, the spin ensemble will not have a net polarization since the spin ensemble will have as many spins aligned with the magnetic field as those that are anti-aligned. In the case of a discrete, quantum system, adding even more energy to the bath paradoxically causes the spin system to predominately anti-aligned to the magnetic field and consequently decrease the spin system entropy. This process is how a polarization inversion can be created. With this in mind we may now define tempera-

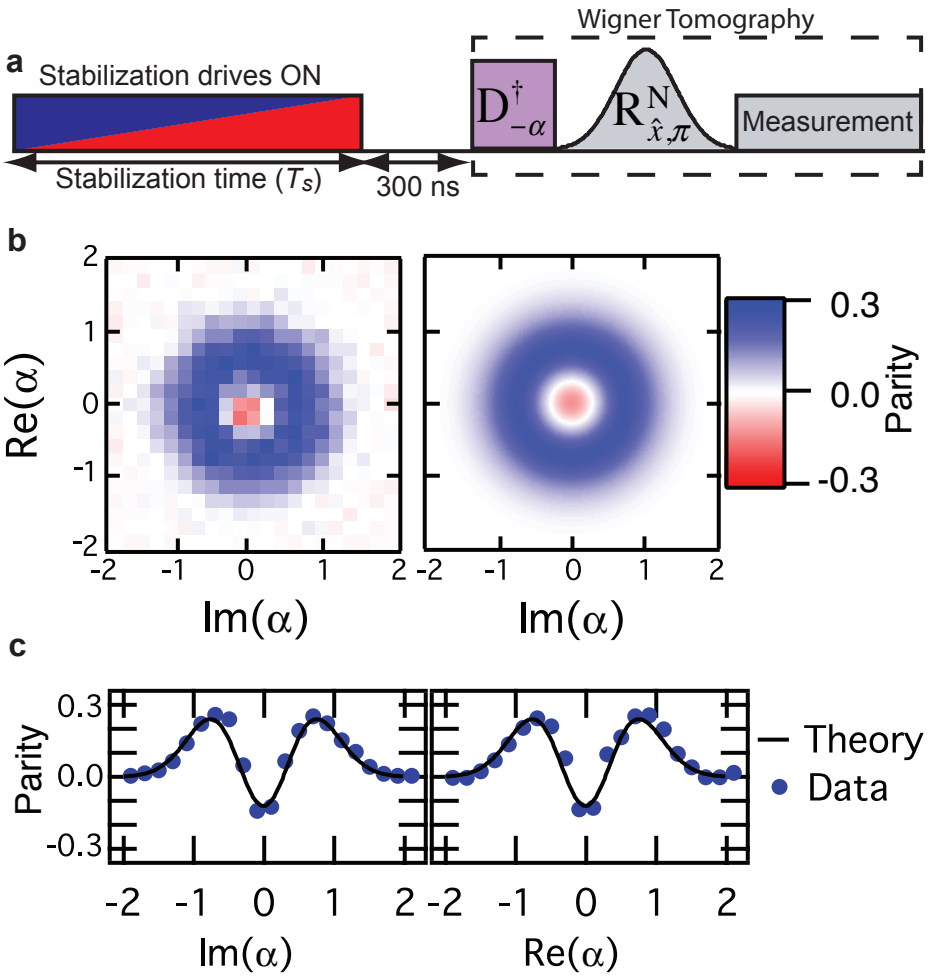

Figure 6.11: Wigner tomography of stabilized steady state of the storage cavity. (a) The previously described stabilization protocol is used to reach the desired steady state. Then Wigner tomography is performed on the state of the storage cavity. (b) Left: Measured Wigner function for the steady state of the storage cavity which is a statistical mixture of an $N = 1$ and $N = 0$ Fock state. Right: Simulated steady state of the protocol. (c) Linecuts along Im(α) and Re(α) for the measured Wigner function and the simulated steady state Wigner function. Although not a pure $N = 1$ Fock state of the storage cavity our long term solution does have negativity in the Wigner function indicative of a quantum state.

ture in terms of the polarization as [164]:

$$T = \frac{h f_{\mathrm{s},0\to1}}{2k_{\mathrm{B}} \tanh^{-1}(p)} \tag{6.20}$$

Where h is Planck's constant and k_{B} is Boltzmann's constant. Using equation 6.20 we determine that our steady state solution corresponds to an effective negative temperature of -0.77 ± 0.06 K in equilibrium with the storage cavity.

Fig. 6.12(b) is a plot of the steady state polarization of the storage cavity after implementing the FSSP. When Ω_{C} is driven at the zero photon peak of the cooling cavity we observe $p = 0.95 \pm .04$ demonstrating that storage cavity is overwhelming in the zero photon Fock state despite the induced Rabi drive on the storage cavity. However, as the drive power and frequency applied to the cooling cavity are varied, steady state stabilization of a polarization inversion occurs corresponding to a predominantly one photon Fock state in the storage cavity. The ability to realize a population inversion is a purely quantum effect.

In Fig. 6.12(d) we see the time dynamics of this protocol where the initial polarization is unity then changing as a function of time to its steady state value of $p = -0.26 \pm 0.04$. Plotted on top of the data is a full simulation of our driven dissipative system where we find excellent agreement in the time dynamics [104]. Through simulation of the full Linblad master equation we find that the limitation in polarization inversion is the finite ratio of lifetimes. Physically realized two cavity systems exist with a ratio of lifetimes being a factor of one thousand [111]. With that ratio we expect that in steady state $P(1) > 0.99$.

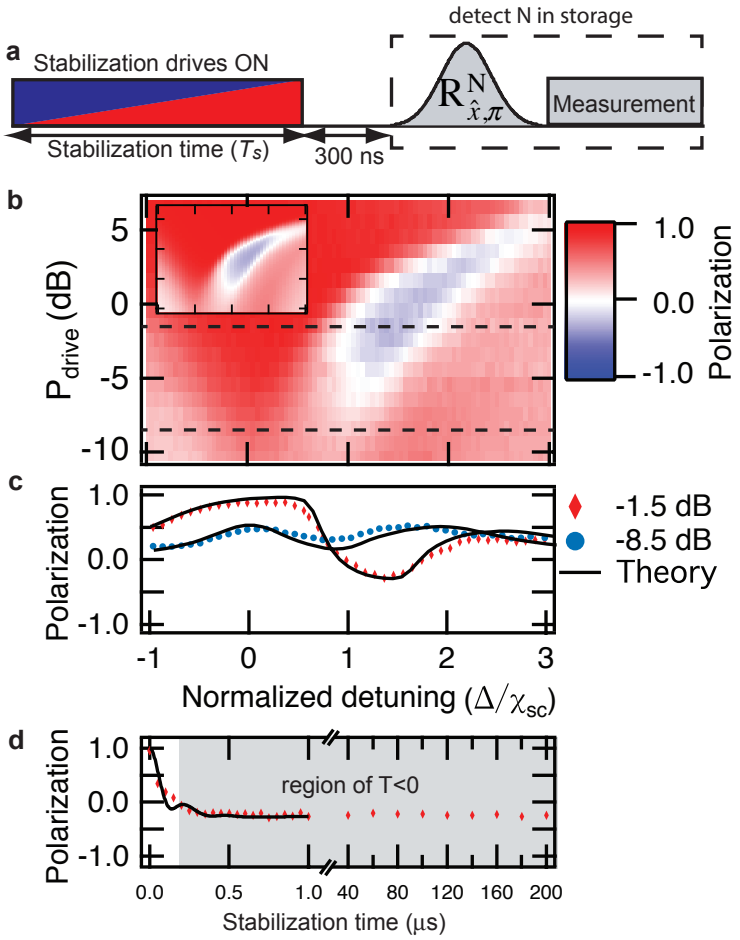

Figure 6.12: Storage cavity polarization. (a) The Fock state stabilization protocol described in Fig. 6.2(b) is applied for a duration, T_s, followed by a 300 ns wait to evacuate excitations from the cooling cavity, a photon selective π pulse is then performed on the qubit determining the probability of each photon state of the storage cavity up to three photons. (b) Storage cavity state polarization as a function of drive amplitude and frequency. The frequency of the cooling cavity drive is plotted as $\Delta = \omega_c^0 - \omega_{dc}$, and normalized by the cross-Kerr, χ_{sc}. As the frequency of the drive applied to the cooling cavity is brought in resonance with the first photon peak of the storage cavity $^{\Delta}/\chi_{sc} \approx 1$ the protocol stabilizes the first Fock state of the storage cavity. The inset is a simulation plot with the same axis and color scale as the experimental result. (c) Linecuts for a weak drive power and a drive power resulting in a polarization inversion. (d) As the duration of the stabilization protocol is varied the polarization of the storage cavity alters and for infinite time reaches its steady state solution.

6.8 Future Improvements

The major limitation of this implementation of the FSSP was our modest ratio of lifetimes between the storage cavity and the cooling cavity, $\kappa_c/\kappa_s \approx 25$. This ratio is most likely set by the Purcell effect between the two cavities. To mitigate the Purcell effect between the cavities, we could improve the design of the qubit and increase its anharmonicity. In this sample the transmon anharmonicity was 26 MHz. The small anharmonicity is in part a consequence of the geometrical capacitance overwhelming the qubit design which has a total length of 5 mm. In addition, the strong coupling between the transmon and the storage cavity has the storage cavity inherit a large fraction of the transmon's nonlinearity. To improve the anharmonicity of the qubit, a gap capacitor could be implemented on one or both sides of the junction to decrease the geometrical capacitance of the qubit. To get a sense for how an increased transmon anharmonicity would help the FSSP results we look at a simple Purcell calculation which gives:

$$\kappa_{\mathrm{S}} \approx \frac{{g_{\mathrm{S}}}^2}{\Delta_{\mathrm{S}}^2}\frac{{g_{\mathrm{C}}}^2}{\Delta_{\mathrm{C}}^2}\kappa_{\mathrm{C}} \approx \frac{\chi_{\mathrm{SC}}}{2\alpha_{\mathrm{q}}}\kappa_{\mathrm{C}} \tag{6.21}$$

For this simple estimation we would expected a ratio of lifetimes to be of order 20 and in experiment we see a ratio of 25. However, if our transmon anharmonicity were increased by a factor of ten then we would expect a simple Purcell limitation resulting in a ratio of lifetimes between the storage and cooling cavity in excess of 250. From this we would expect to stabilize a one photon Fock state with $P(1) > .87$ and a polarization of $p < -.74$. To further improve

the ratio of lifetimes between the storage cavity and cooling cavity a Purcell filter such as the waveguide Purcell filters made by collaborators at Yale University would be necessary. An outstanding issue in superconducting circuits is coupling long lived elements such as cavities to less coherent elements such as qubits or readout cavities. For successful integration, without comprising coherence, work must continue in developing novel approaches to merge highly coherent devices with intentionally short lived quantum objects.

6.8.1 Final Comment

In this chapter the first single photon cavity-cavity cross-Kerr is presented. This large cavity-cavity state dependent shift was developed so that we could implement the FSSP. Future applications of the cross-Kerr are in a QRE scheme that stabilizes an even two 'cat' state of a cavity [154], as well as, serving as a direct cavity-cavity entangling operation. A one photon Fock state, as well as, the vacuum state of the storage cavity were stabilized. To achieve this stabilization, we demonstrated a considerable level of mastery and conceptual understanding was required over a driven, dissipative cavity centric protocol adding to the general knowledge base of the cQED community. Going forward it is unclear what role QRE will play in the pursuit of a quantum computer. It may be the case that QRE protocols are most useful in stabilizing either a logical state, or a subset of logical states. The advantage of QRE is that the feedback loop is built into the Hamiltonian whose latency is most likely less than protocols that require measurements of ancillary systems with external feedback.

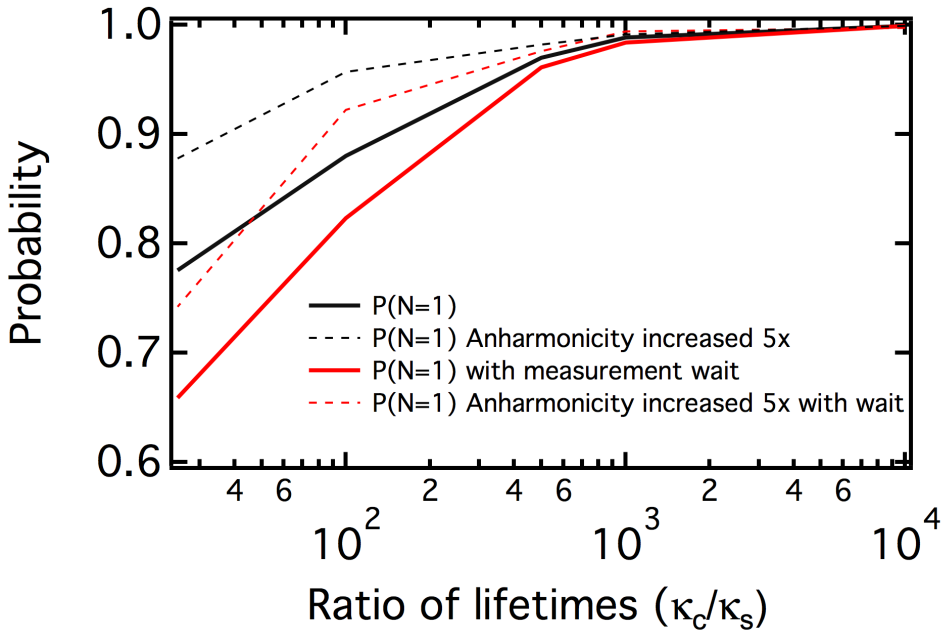

Figure 6.13: Simulation of driven dissipative system for stabilizing a one photon Fock state in the storage cavity. In solid lines are the results of the steady state population of a one photon Fock state in the storage cavity. In black is what would be measured with perfect tomography. In red is a more realistic expectation that includes decay during the tomography. As we would expect, as the lifetime of the storage cavity is increased we are less susceptible to photon loss during our measurement. By obtaining a ratio of one thousand between the two cavities we would stabilize a one photon Fock state with $P(1) > .99$. In dashed lines are if the storage cavities' anharmonicity was increased by a factor of five and if the state dependent shift was increased by a factor of root five. We see that for smaller ratios of lifetimes that this helps but as we approach truly long lived cavities the difference is negligible.

7

Conclusion & Outlook

7.1 Conclusion

In the past six years the progress and growth of the quantum superconducting circuit community has been to say the least impressive. Continual improvements in quantum device coherence times (Fig. 7.1) as well as an ever expanding field bodes well for quantum information with superconducting circuits.

Indicative of this growth is a long standing memory I will have from the 2014 APS March Meeting in Denver, CO where fire regulations prevented many physicists from attending talks and one person in particular was only able to enter for her presentation through polite and persistent discourse [75]. This thesis is part of the progress in the last six years. Some parts will pay large dividends in the future as quantum systems increase in size and complexity as 3D integration becomes necessary. Other parts are reflective of great advances in classical and quantum simulation capabilities. The ability to engineer a Hamiltonian with remarkable precision through classical electromagnetic simulation is an under appreciated development [102]. Furthermore, the ubiquity of open source quantum simulation capabilities such as QuTIP enable deeper synthesis between theory and experiment.

7.2 Future Experiments

In this section future work will be discussed based on accomplishments from previous chapters. This list is not exhaustive nor does it include applications for existing theoretical proposals. For instance, Ref. [154] relies on a large cavity-cavity state dependent shift, along with parametric processes, to stabilize the even two component Schrödinger cat state of a cavity.

7.2.1 Extension to Fock State Stabilization

The first possible experiment is applying the Fock state stabilization protocol discussed in chapter 6 to stabilize higher Fock states of a microwave cavity. The

setup would be very similar to chapter 6 where a storage cavity is strongly coupled to a cooling cavity. The decay rate of the cooling cavity must be fast compared to the storage cavity. To alter the protocol in chapter 6, it would require adding Rabi drives between adjacent Fock states of the storage cavity up to the desired Fock state for stabilization. In a sense this can be thought of creating a "Rabi ladder" between vacuum and the desired Fock state to be stabilized. The final drive needed would be applied at the cooling cavity but detuned by the number of cross-Kerrs ($\omega_C^N = \omega_C^0 - N\chi_{SC}$) corresponding to the N such Fock state to be stabilized.

On an experimental front, realizing a highly coherent cavity strongly coupled (enough to inherit ~ 1 MHz of anharmonicity) to a transmon stands as a formidable challenge. Ideally, one would use a cavity with coherence times of order 1 ms so that a variety of Fock states could be stabilized with high fidelity. Accomplishing this is nontrivial and requires a fair amount of development. However, the payoff could be realized in the next section.

7.2.2 N00N State Stabilization

References [157] and [159] both leveraged quantum reservoir engineering protocols to stabilize a Bell state of two qubits. One could recast these results as the stabilization of a N00N state where e $\rightarrow$ N $= 1,$ and g $\rightarrow$ N $= 0$. With this observation there are two possible options to stabilize N00N states with $N > 1$. One possibility would be to have two weakly anharmonic transmons coupled to a cooling cavity. The other possibility uses two storage cavities that

are strongly coupled to transmons to inherit nonlinearity as well as a cooling cavity which acts as an entropy dump. The second approach has the advantage of one being able to claim that the cavities have no innate nonlinearity at the expense of requiring more 'hardware'.

For the remainder of the discussion we will gloss over which exact hardware is chosen and simply refer to the entangled system we are stabilizing as two storage cavities that have a strong dispersive interaction to a cooling cavity and that the state dependent shifts between either storage cavity and the cooling cavity are equal. The first pair of drives are applied to the cooling cavity at ω_c^{00} and ω_c^{NN} which are only resonant, and therefore displace the state of the cooling cavity, provided that two storage cavity states are both in vacuum or maximally excited. The next type of drives applied are to the storage cavities and are Rabi drives—the same "Rabi ladders" discussed in the previous section. In total four "Rabi ladders" would need to be applied to the system. The first pair of "Rabi ladders" are applied to the storage cavities, coherently swapping excitations between vacuum and the N^{th} Fock state of that storage cavity provided that the cooling cavity is in its ground state. The second pair of Rabi ladders would be applied to the storage cavities in the same manner as previously described; however, for the case of the cooling cavity being in some optimal coherent state. The phase difference between the two pairs of "Rabi ladders" would set the phase of the observed N00N state. This experiment would be highly demanding of the coherence required, the coupling strengths needed between cavities as well as the microwave drives needed for the system.

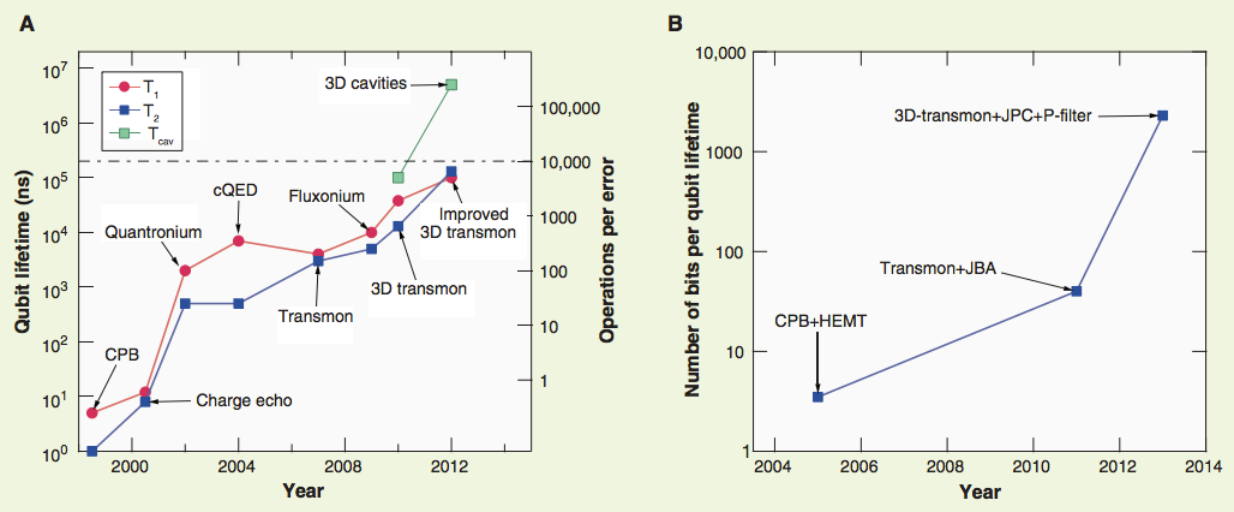

Figure 7.1: Historical Progress of Superconducting Circuits. From Ref. [44] as an illustrative figure showing the impressive progress of superconducting circuits.

7.3 Future Outlook

In some sense the outlook given in this thesis is not dramatically different than that given in other dissertations. Superconducting circuits continue to show great progress for the realization of a quantum computer as well as a test bed for quantum information and quantum optics experiments. However, at the writing of this thesis superconducting circuits are at a unique point in their history. Over the past twenty years superconducting circuits have grown from an academic curiosity to as serious of an option for a quantum computer as trapped ions. A novel feature of superconducting circuit is that the physicist has tremendous freedom in designing the Hamiltonian. Hopefully, in the coming years the ability to design a Hamiltonian is adequately leveraged because superconducting circuits are, as a community, positioned to become a trail blazing

testbed for new and innovative pursuits in quantum information science.

A

Recipes

A.1 Cavity Photolithography

A.1.1 Resist

To improve the LOR5A to sapphire adhesion the following is performed before the resist is spun:

1. 5 minute bake at 195 C
2. 1 minute cooling at room temperature on heat sink
3. O_2 Ash 3 minutes
4. Spin HMDS

Spin the bilayer resist:

1. LOR 5A @4000 RPM for 60 seconds.
2. Bake 195 C for 5 minutes.
3. Let cool for 2 minutes on aluminum block.
4. S1805 @4000 RPM for 60 seconds
5. 115 C for 1 minute.
6. Run in Heidelberg.

A.1.2 Development

1. MF-319 for 80 seconds.
2. Dunk in DI water for 15 seconds.
3. Hold under running DI water 10 seconds.
4. Blow dry.

A.2 Cavity Etching

This recipe was shown [58] to improve the quality factor of high purity aluminum microwave cavities. At Yale we do all etching in the cleanroom since this is an acid etch.

A.2.1 Tools Required

1. At a minimum two beakers. One beaker will hold the cavity being etched as well as the acid being poured in. Since the acid must fully cover the cavity one needs a beaker deep enough so that a cavity can be placed in the beaker and fully covered with acid we use a beaker which is roughly four times larger than the volume of the cavity we are etching. The second beaker must be larger than the first one and is there to catch any acid that overflows. Having two sets of beakers will make your life easier since the acid must be replaced half way through the etch.

2. Two petri dishes capable of covering the smaller nested beaker.

4. Teflon stirring bean

5. Protective gear suitable for working with acid. In the Yale cleanroom on top of the normal attire this includes: face shield, apron and green gloves suitable for handling acid.

6. Tweezers though if cleanroom approved tongs (possibly rubber ends) are found then these would be preferred.

A.2.2 Setting Up

The most important step in this process is checking that the external thermometer is NOT plugged into the hot plate. If you leave this in, you will cause open loop heating of a volatile acid. We begin with:

1. With protective gear on, place the nested beakers on the hot plate in the acid hood.

2. Add cavities with the critical surfaces (the inside of the cavity versus outside) facing each other and stirring bean.

3. Fill the inner beaker about 80% full with Aluminum Etch A - located in the bottom right cabinet of the acid hood. The maximum acid to aluminum volume ratio is 4:1

4. Cover with petri dish.

5. Set the hot plate to 50 C and the stirring rate at 175 RPM.

6. Leave a note with the description of the setup and your phone number.

A.2.3 Acid change at two hour mark

1. The red gas floating about your now green beaker is expected. If your acid is clear and boiling rapidly you ve likely passed the saturation point of the acid and your etch rate will have been much higher than typical.

2. With protective gear on, remove the nested beakers from the hot plate.

3. Move them to the back of the acid hood.

4. Tip the Petri dish to remove the Nitrogen Oxide (holding breath not required).

5. Clean the Petri dish with water and set on a wipe

6. Fill the second beaker with fresh Alum Etch A enough to cover your cavities.

7. With the tweezers, move the cavities and stirring bean to the fresh acid.

8. Remove the waste acid beaker from the nested configuration (somewhat tricky) and place on a wipe in the acid hood. Cover this beaker with a Petri dish, and slide to the back with a note describing the acid as Cooling from 50 deg C, Waste Alum Etch A with your contact info.

9. Put the fresh acid beaker into the larger beaker for spillage protection, cover and place on the hot plate.

A.2.4 Finish

1. Repeat steps (1-5) from the previous section. You should be wearing protective gear throughout this process.

2. Empty the now-cooled waste beaker into the acid waste bottle labeled for Alum Etch/Phosphoric and Nitric Acid, wash thoroughly with water, and fill with water.

3. Move the cavities and stirring bean from the acid into the water beaker, giving them a quick shake in the acid before moving.

4. In the solvent hood, open the unhalogenated waste bottle and mount a funnel in it.

5. Remove from the water with tweezers the first aluminum piece to be cleaned, run the water gun in the acid hood over the critical surfaces for 1 min with high pressure in the sink, follow with a quick rinse with methanol in the solvent hood, and blow dry with Nitrogen gas. Repeat for each piece.

6. Clean the stirring bean, water beaker, and tweezers in the acid sink.

7. If 30 min have passed you may dump the waste acid into the waste container. If not allow the acid to cool off or else it will react with the bottle comprising its integrity. Finally, clean the last few beakers and wipe down any water that may have accumulated on the acid hood.

A.3 Dolan Bridge Josephson Junction Recipe

A.3.1 Wafer Cleaning (15 minutes)

1. Later we will need the hot plate to have a surface temperature of 175C. Since the time response of the cleanroom thermometers are slow it is advised you check it now and make any adjustments necessary now.

2. 3min NMP ultrasonic

3. 3min Aceton ultrasonic

4. 3min Methanol ultrasonic

5. N2 blow dry

6. Optionally you could bake the wafer for a few minutes if you are concerned about moisture.

A.3.2 Resist spinning (45 minutes)

Check to make sure that all resist is not expired.

1. MMA EL13, 90 sec, 5000 rpm, acceleration code 17.

2. Bake for 1min @ 175 C surface temperature.

3. Let it cool off on Al block for 1min.

4. PMMA A3, 90 sec, 4000 rpm, acceleration code 17.

5. Bake for 30 min @ 175C surface temperature.

6. Let it cool off on aluminum block for 1min.

7. Put the sample in a vacuum container with desiccant.

A.3.3 Anti-charging Layer (1 hour)

If using the 'old' Plassys, put 13nm of aluminum on top of the bilayer resist. It is strongly recommended to use the electron beam to write your sample within 24 hours.

A.3.4 Electron beam writing (2-4 hours depending area to be written)

1. Before e-beam make sure temperature of MIBK:IPA bath is 25 C.
2. Transport sample to and from EBPG in vacuum container with desiccant.
3. Dose for big structures $680\mu\frac{\mathrm{C}}{\mathrm{cm}^2}$ @ 50 nA
4. Dose for small structures (junctions) $220\mu\frac{\mathrm{C}}{\mathrm{cm}^2}$ @ 5nA

A.3.5 Development (15 minutes)

1. Remove aluminum anti-charging layer with MF-312 for 90 seconds.
2. COMPLETELY blow dry the wafer, your tweezers and the holder for the wafer. The reason this must be completely blown dry is that MF-312 contains H_2O and H_2O combined with IPA is a developer of our resist. This means your sample will develop much faster than it is supposed to and lead to unreliable results.
3. Fill MIBK:IPA beaker after MF-312, Temperature: 25 C and fill up a second beaker with IPA.
4. Develop for 55 seconds in MIBK:IPA.
5. Immediately (1sec) put into IPA for 10 seconds.
6. Blow dry.

A.3.6 Deposition (4 hours)

1. Mount correctly so that the "hammer" is on the appropriate side. Older styles of vertical transmons (circa 2012/2013) have the flat of the wafer being perpendicular to the gun and as far as possible to the gun. Current styles have the wafer perpendicular to the gun with the flat as close as possible to the gun.

2. Line up sample with stage as precisely as possible.

3. Line up stage with arrow and screw.

4. Run deposition.

5. Remove wafer while being grounded with a wrist strap and put it in a conducting wafer carrier.

A.3.7 Liftoff (2+hours)

1. Always Handle wafer wearing a grounded wrist strap.

2. Either put the wafer into acetone @ 75C face down for 90 minutes with a lid on it because acetone evaporates. Or, put wafer into NMP @ 90 C face down for 90min with lid.

3. Use syringe or squirt bottle to remove left over aluminum.

4. Clean wafer by submersing in Acetone (unless lifted off in Acetone) and then Methanol. NMP can leave a residue unless properly cleaned off.

5. Blow dry.

6. Check resistances of the junctions to verify this process worked.

7. Put back into conducting wafer carrier.

A.3.8 Dicing (4 hours)

1. We need to spin photo resist on waver before dicing.

2. Always be grounded when handling wafer.

3. Spin SC1827 for 2min at 1500rpm.

4. Let it dry (!!no!! hot plate) for 5 min. It should be dry enough to pick up and put into the conductive wafer carrier.

5. Wait for 2h before dicing to completely dry it

6. Dicing (1-3h depending on number of cuts)

7. Always handle wafer with grounded wrist strap

8. For dicing you must be trained so ask the master.

A.3.9 After dicing (2 hours)

1. Clean the pieces in acetone for 30 seconds and then methanol for 30 seconds.

2. Blow dry.

3. Put in container

B

QuTiP Code

B.1 Fock State Stabilization

B.1.1 Time Dependent Solver

```
import numpy as np
import qutip as qutip
import pylab as pylab
```

import math

Define the number of excitations in the storage cavity, s, and cooling cavity, c. Also, define their decay rates.

Nc = 60

Ns=4

kappa_s = 2*math. pi*.072 *storage decay*

kappa_c = 2*math. pi*1.7 *cooling decay*

Define the Hamiltonian parameter

Kerr_s = -2*math.pi*4.4 *storage anharmonicity*

Kerr_c = -2*math.pi*.3 *cooling cavity anharmonicity*

x_sc = -2*math.pi*2.5 *cross kerr*

detune_s = .5*Kerr_s *detuning*

detune_c = -x_sr*1.45 *detune one cross kerr away*

E_d_s = 2*math.pi*1.85 *storage drive strength*

E_d_c = 2*math.pi*3.25 *cooling (conditional measurement) drive strength*

Define operators in Hamiltonian

a = qutip.tensor(qutip.destroy(Ns), qutip.qeye(Nc)) *destroy a photon in the storage cavity*

c = qutip.tensor(qutip.qeye(Ns), qutip.destroy(Nc)) *destroy a photon in the readout cavity*

Ncav_s = a.dag()*a *cavity number operator storage*

Ncav_c =c.dag()*c *cavity number operator cooling*

Define the Hamiltonian

H = detune_s*Ncav_s+detune_c*Ncav_c

+.5*Kerr_s*a.dag()*a.dag()*a*a+.5*Kerr_c*c.dag()*c.dag()*c*c

+x_sc*a.dag()*a*b.dag()*b+E_d_s*(a.dag()+a)+E_d_c*(c.dag()+c)

Define an initial state in this Hilbert space

psi0=qutip.tensor(qutip.basis(Ns,0),qutip.basis(Nr,0))

Define the collapse operator

c_ops = [] *collapse operator*

c_ops.append(math.sqrt(kappa_s)*a) *storage cavity decay*

c_ops.append(math.sqrt(kappa_c)*c) *cooling cavity decay*

Define the number of time steps as well as set the options on the ODE so that this will converge

tlist = np.linspace(0.0, 10.0, 1000.0)

opts=qutip.Odeoptions()

opts.nsteps=1000

Linblad equation

```
medata = qutip.mesolve(H, psi0, tlist, c_ops, [],options=opts)
expect = False
print medata.states
```

Time behavior of the 1 photon Fock state of the storage cavity

```
results1=[0]*1000;
for ix in range(1000):
print "We're on time %d" % (ix)
results1[ix]=qutip.expect(qutip.fock_dm(Ns,1),qutip.ptrace(medata.states[ix],0))
   print "Results N=1"
print results1
```

Time behavior of the 0 photon Fock state of the storage cavity

```
results0=[0]*1000;
for ix in range(1000):
print "We're on time %d" % (ix)
results0[ix]=qutip.expect(qutip.fock_dm(Ns,0),qutip.ptrace(medata.states[ix],0))
   print "Results N=0"
print results0
```

Plot results

```
pylab.plot(tlist,results1)
```

pylab.plot(tlist,results0)

pylab.xlabel("Time")

pylab.ylabel("Probability")

pylab.legend(("N1","N0"))

pylab.show()

B.1.2 Steady State Solver

import numpy as np

import qutip as qutip

import pylab as pylab

import math

Define the number of excitations in the storage cavity, s, and cooling cavity, c. Also, define their decay rates.

Nc = 60

Ns=4

kappa_s = 2*math. pi*.072 *storage decay*

kappa_c = 2*math. pi*1.7 *cooling decay*

Define the Hamiltonian parameter

Kerr_s = -2*math.pi*4.4 *storage anharmonicity*

Kerr_c = -2*math.pi*.3 *cooling cavity anharmonicity*

x_sc = -2*math.pi*2.5 *cross kerr*

E_d_s = 2*math.pi*1.85 *storage drive strength*

E_d_carray = np.array([2*.5*math.pi*t for t in np.linspace(0,30,num=30)]);

detune_carray = np.array([2*math.pi*t for t in np.linspace(-3,10,num=30)]);

print "Cooling drive"

edctemp=E_d_carray*pow(2*math.pi,-1)

print edrtemp

np.savetxt('DriveStrengthCooling',edctemp)

print "Storage detuning"

dctemp=detune_carray*pow(x_sc,-1)

print dctemp

np.savetxt('DetuningInUnitsOfCrossKerr',dctemp)

Define operators in Hamiltonian

a = qutip.tensor(qutip.destroy(Ns), qutip.qeye(Nc)) *destroy a photon in the storage cavity*

c = qutip.tensor(qutip.qeye(Ns), qutip.destroy(Nc)) *destroy a photon in the readout cavity*

Ncav_s = a.dag()*a *cavity number operator storage*

Ncav_c =c.dag()*c *cavity number operator cooling*

Define Empty Matrices for Saving Data

mat1 = np.zeros((len(E_d_carray),len(detune_carray)))

matns = np.zeros((len(E_d_carray),len(detune_carray)))

```
matnc = np.zeros((len(E_d_carray),len(detune_carray)))
mat0 = np.zeros((len(E_d_carray),len(detune_carray)))
mat2 = np.zeros((len(E_d_carray),len(detune_carray)))
mat3 = np.zeros((len(E_d_carray),len(detune_carray)))
for ix in range(len(E_d_carray)):
print 'ix = %d' % ix
for iy in range(len(detune_carray)):
H = detune_s*Ncav_s+detune_carray[iy]*Ncav_r+.5*Kerr_s*a.dag()*a.dag()*a*a+.5*Kerr_r*b.d
   +x_sr*a.dag()*a*b.dag()*b+E_d_s*(a.dag()+a)+E_d_carray[ix]*(b.dag()+b)
final_state = qutip.steadystate(H, c_ops)
val1 = qutip.expect(qutip.fock_dm(Ns,1),qutip.ptrace(final_state,0))
val0 = qutip.expect(qutip.fock_dm(Ns,0),qutip.ptrace(final_state,0))
val2 = qutip.expect(qutip.fock_dm(Ns,2),qutip.ptrace(final_state,0))
val3 = qutip.expect(qutip.fock_dm(Ns,3),qutip.ptrace(final_state,0))
valns = qutip.expect(Ncav_s,final_state)
valnc = qutip.expect(Ncav_c,final_state)
mat1[ix,iy] = round(val1,4)
mat0[ix,iy] = round(val0,4)
mat2[ix,iy] = round(val2,4)
mat3[ix,iy] = round(val3,4)
matns[ix,iy] = round(valns,4)
matnc[ix,iy] = round(valnc,4)
print "Probability 1fock"
```

```
print mat1
np.savetxt('PopN1',mat1)
print "Probability 0fock"
print mat0
np.savetxt('PopN0',mat0)
print "Probability 2fock"
print mat2
np.savetxt('PopN2',mat2)
print "Probability 3fock"
print mat3
np.savetxt('PopN3',mat3)
print "Nbar in storage"
print matns
np.savetxt('NbarStorage',matns)
print "Nbar in cooling"
print matnc
np.savetxt('NbarCooling',matnc)
```

Bibliography

[1] E. Schrödinger, Brit. J. Phil. Sci. **3**, 233 (1952).

[2] A. J. Leggett, Le Journal de Physique Colloques **39**, C6 (1978).

[3] A. J. Leggett, Prog. of Theor. Phys. (Suppl.) **69**, 80 (1980).

[4] A. O. Caldeira and A. J. Leggett, Ann. Phys. **149**, 374 (1983).

[5] M. H. Devoret, J. M. Martinis, D. Esteve, and J. Clarke, Phys. Rev. Lett. **53**, 1260 (1984).

[6] M. H. Devoret, J. M. Martinis, and J. Clarke, Phys. Rev. Lett. **55**, 1908 (1985).

[7] D. Esteve, M. H. Devoret, and J. M. Martinis, Phys. Rev. B **34**, 158 (1986).

[8] J. M. Martinis, M. H. Devoret, and J. Clarke, Phys. Rev. Lett. **55**, 1543 (1985).

[9] J. M. Martinis, M. H. Devoret, and J. Clarke, Phys. Rev. B **35**, 4682 (1987).

[10] Y. Nakamura, Y. A. Pashkin, and J. S. Tsai, Nature **398**, 786 (1999).

[11] J. E. Mooij, T. P. Orlando, L. Levitov, L. Tian, C. H. Van der Wal, and S. Lloyd, Science **285**, 1036 (1999).

[12] R. P. Feynman, International Journal of Theoretical Physics **21**, 467 (1982).

[13] D. Deutsch, in *Proceedings of the Royal Society of London A: Mathematical, Physical and Engineering Sciences*, Vol. 400 (The Royal Society, 1985) pp. 97–117.

[14] D. Deutsch and R. Jozsa, in *Proceedings of the Royal Society of London A: Mathematical, Physical and Engineering Sciences*, Vol. 439 (The Royal Society, 1992) pp. 553–558.

[15] P. W. Shor, in *Foundations of Computer Science, 1994 Proceedings., 35th Annual Symposium on* (IEEE, 1994) pp. 124–134.

[16] P. W. Shor, Phys. Rev. A **52**, R2493 (1995).

[17] P. W. Shor, in *Foundations of Computer Science, 1996. Proceedings., 37th Annual Symposium on* (IEEE, 1996) pp. 56–65.

[18] P. W. Shor, SIAM Journal on Computing **26**, 1484 (1997).

[19] A. Steane, in *Proceedings of the Royal Society of London A: Mathematical, Physical and Engineering Sciences*, Vol. 452 (The Royal Society, 1996) pp. 2551–2577.

[20] A. M. Steane, Phys. Rev. Lett. **78**, 2252 (1997).

[21] R. Laflamme, C. Miquel, J. P. Paz, and W. H. Zurek, Phys. Rev. Lett. **77**, 198 (1996).

[22] M. A. Nielsen and I. L. Chuang, *Quantum computation and quantum information* (Cambridge university press, 2010).

[23] I. L. Chuang, L. M. Vandersypen, X. Zhou, D. W. Leung, and S. Lloyd, Nature **393**, 143 (1998).

[24] I. L. Chuang, N. Gershenfeld, and M. Kubinec, Phys. Rev. Lett. **80**, 3408 (1998).

[25] J. A. Jones, M. Mosca, and R. H. Hansen, Nature **393**, 344 (1998).

[26] L. M. K. Vandersypen, M. Steffen, G. Breyta, C. S. Yannoni, M. H. Sherwood, and I. L. Chuang, Nature **414**, 883 (2001).

[27] W. S. Warren, Science **277**, 1688 (1997).

[28] J. I. Cirac and P. Zoller, Phys. Rev. Lett. **74**, 4091 (1995).

[29] D. Leibfried, R. Blatt, C. Monroe, and D. Wineland, Reviews of Modern Physics **75**, 281 (2003).

[30] D. Leibfried, B. DeMarco, V. Meyer, D. Lucas, M. Barrett, J. Britton, W. M. Itano, B. Jelenković, C. Langer, T. Rosenband, *et al.*, Nature **422**, 412 (2003).

[31] D. Kielpinski, C. Monroe, and D. J. Wineland, Nature **417**, 709 (2002).

[32] T. Monz, P. Schindler, J. T. Barreiro, M. Chwalla, D. Nigg, W. A. Coish, M. Harlander, W. Hänsel, M. Hennrich, and R. Blatt, Phys. Rev. Lett. **106**, 130506 (2011).

[33] H.-J. Briegel, T. Calarco, D. Jaksch, J. I. Cirac, and P. Zoller, Journal of modern optics **47**, 415 (2000).

[34] D. Loss and D. P. DiVincenzo, Physical Review A **57**, 120 (1998).

[35] R. Hanson, L. Kouwenhoven, J. Petta, S. Tarucha, and L. Vandersypen, Rev. Mod. Phys. **79**, 1217 (2007).

[36] B. M. Maune, M. G. Borselli, B. Huang, T. D. Ladd, P. W. Deelman, K. S. Holabird, A. A. Kiselev, I. Alvarado-Rodriguez, R. S. Ross, A. E. Schmitz, *et al.*, Nature **481**, 344 (2012).

[37] M. D. Shulman, O. E. Dial, S. P. Harvey, H. Bluhm, V. Umansky, and A. Yacoby, Science **336**, 202 (2012).

[38] D. D. Awschalom, L. C. Bassett, A. S. Dzurak, E. L. Hu, and J. R. Petta, Science **339**, 1174 (2013).

[39] F. Jelezko and J. Wrachtrup, PHYSICA STATUS SOLIDI A APPLICATIONS AND MATERIALS SCIENCE **203**, 3207 (2006).

[40] M. V. G. Dutt, L. Childress, L. Jiang, E. Togan, J. Maze, F. Jelezko, A. S. Zibrov, P. R. Hemmer, and M. D. Lukin, Science **316**, 1312 (2007).

[41] P. C. Maurer, G. Kucsko, C. Latta, L. Jiang, N. Y. Yao, S. D. Bennett, F. Pastawski, D. Hunger, N. Chisholm, M. Markham, *et al.*, Science **336**, 1283 (2012).

[42] W. Pfaff, T. H. Taminiau, L. Robledo, H. Bernien, M. Markham, D. J. Twitchen, and R. Hanson, Nature Physics **9**, 29 (2013).

[43] W. Pfaff, B. Hensen, H. Bernien, S. B. van Dam, M. S. Blok, T. H. Taminiau, M. J. Tiggelman, R. N. Schouten, M. Markham, D. J. Twitchen, *et al.*, Science **345**, 532 (2014).

[44] M. H. Devoret and R. J. Schoelkopf, Science **339**, 1169 (2013).

[45] B. R. Johnson, M. D. Reed, A. A. Houck, D. I. Schuster, L. S. Bishop, E. Ginossar, J. M. Gambetta, L. DiCarlo, L. Frunzio, S. M. Girvin, *et al.*, Nature Phys. **6**, 663 (2010).

[46] M. Hatridge, S. Shankar, M. Mirrahimi, F. Schackert, K. Geerlings, T. Brecht, K. M. Sliwa, B. Abdo, L. Frunzio, S. M. Girvin, *et al.*, Science **339**, 178 (2013).

[47] A. A. Houck, J. Koch, M. H. Devoret, S. M. Girvin, and R. J. Schoelkopf, Quantum Information Processing **8**, 105 (2009).

[48] D. M. Pozar, *Microwave Engineering*, 3rd ed. (John Wiley & Sons, Inc., 2005).

[49] R. P. Feynman, R. B. Leighton, and M. Sands, *The Feynman Lectures on Physics*, Vol. 2 (Basic Books, 2013).

[50] M. Reagor, W. Pfaff, R. Heeres, N. Ofek, K. Chou, J. Blumoff, Z. Leghtas, S. Touzard, K. Sliwa, E. T. Holland, *et al.*, Bulletin of the American Physical Society **60** (2015).

[51] W. Pfaff, M. Reagor, R. Heeres, N. Ofek, K. Chou, J. Blumoff, Z. Leghtas, S. Touzard, K. Sliwa, E. T. Holland, *et al.*, Bulletin of the American Physical Society **60** (2015).

[52] M. Reagor, W. Pfaff, C. Axline, R. W. Heeres, N. Ofek, K. Sliwa, E. T. Holland, C. Wang, J. Blumoff, K. Chou, M. J. Hatridge, L. Frunzio, M. H. Devoret, L. Jiang, and R. J. Schoelkopf, (2015), 1508.05882 .

[53] R. W. Heeres, B. Vlastakis, E. T. Holland, S. Krastanov, V. V. Albert, L. Frunzio, L. Jiang, and R. J. Schoelkopf, arXiv preprint arXiv:1503.01496 (2015).

[54] S. Krastanov, V. V. Albert, C. Shen, C.-L. Zou, R. W. Heeres, B. Vlastakis, R. J. Schoelkopf, and L. Jiang, arXiv preprint arXiv:1502.08015 (2015), 1502.08015 .

[55] R. Barends, N. Vercruyssen, A. Endo, P. J. de Visser, T. Zijlstra, T. M. Klapwijk, P. Diener, S. J. C. Yates, and J. J. A. Baselmans, Appl. Phys. Lett. **97**, 023508 (2010).

[56] M. R. Vissers, J. S. Kline, J. Gao, D. S. Wisbey, and D. P. Pappas, Appl. Phys. Lett. **100**, 082602 (2012).

[57] A. Bruno, G. de Lange, S. Asaad, K. L. van der Enden, N. K. Langford, and L. DiCarlo, Appl. Phys. Lett. **106**, 182601 (2015).

[58] M. J. Reagor, H. Paik, G. Catelani, L. Sun, C. Axline, E. T. Holland, I. M. Pop, N. A. Masluk, T. Brecht, L. Frunzio, *et al.*, Appl. Phys. Lett. **102**, 192604 (2013).

[59] J. M. Raimond, T. Meunier, P. Bertet, S. Gleyzes, P. Maioli, A. Auffeves, G. Nogues, M. Brune, and S. Haroche, J. Phys. B: At. Mol. Opt. Phys. **38**, S535 (2005).

[60] T. K. Sarkar, R. Mailloux, A. A. Oliner, M. Salazar-Palma, and D. L. Sengupta, *History of Wireless*, Vol. 177 (John Wiley & Sons, 2006).

[61] H. H. Howe, *Stripline Circuit Design* (Artech House Dedham, MA, 1974).

[62] H. Paik, D. I. Schuster, L. S. Bishop, G. Kirchmair, G. Catelani, A. P. Sears, B. R. Johnson, M. J. Reagor, L. Frunzio, L. I. Glazman, *et al.*, Phys. Rev. Lett. **107**, 240501 (2011).

[63] A. P. Sears, A. Petrenko, G. Catelani, L. Sun, H. Paik, G. Kirchmair, L. Frunzio, L. I. Glazman, S. M. Girvin, and R. J. Schoelkopf, Phys. Rev. B **86**, 180504 (2012).

[64] A. P. Sears, *Extending Coherence in Superconducting Qubits: From microseconds to milliseconds*, Ph.D. thesis, Yale University (2013).

[65] B. Bhat and S. K. Koul, *Stripline-like transmission lines for microwave integrated circuits* (New Age International, 1989).

[66] G. Catelani, Private Communications.

[67] S. B. Nam, Phys. Rev. **156**, 470 (1967).

[68] S. B. Nam, Phys. Rev. **156**, 487 (1967).

[69] J. P. Turneaure and I. Weissman, J. Appl. Phys. **39**, 4417 (1968).

[70] J. P. Turneaure, J. Halbritter, and H. A. Schwettman, JOSC **4**, 341 (1991).

[71] L. D. Landau and E. M. Lifshitz, *Course of theoretical physics*, Vol. 10 (Elsevier, 2013).

[72] M. Tinkham, *Introduction to Superconductivity* (Courier Corporation, 2012).

[73] T. Brecht, M. Reagor, Y. Chu, W. Pfaff, C. Wang, L. Frunzio, M. H. Devoret, and R. J. Schoelkopf, arXiv preprint arXiv:1509.01119 (2015).

[74] C. Axline, M. J. Reagor, K. Shain, P. Reinhold, T. Brecht, E. T. Holland, C. Wang, R. Heeres, L. Frunzio, and R. J. Schoelkopf, Bulletin of the American Physical Society **60** (2015).

[75] T. Brecht, C. Wang, C. Axline, M. J. Reagor, M. Hatridge, P. Reinhold, L. Frunzio, and R. J. Schoelkopf, Bulletin of the American Physical Society **59** (2014).

[76] T. Brecht, W. Pfaff, C. Wang, Y. Chu, L. Frunzio, M. H. Devoret, and R. J. Schoelkopf, arXiv preprint arXiv:1509.01127 (2015).

[77] M. Fox, *Quantum Optics: An Introduction* (Oxford University Press, 2006).

[78] C. Gerry and P. Knight, *Introductory Quantum Optics* (Cambridge University Press, 2005).

[79] D. F. Walls and G. J. Milburn, *Quantum Optics* (Springer Science & Business Media, 2007).

[80] H. Mabuchi and A. C. Doherty, Science **298**, 1372 (2002).

[81] E. T. Jaynes and F. W. Cummings, Proceedings of the IEEE **51**, 89 (1963).

[82] F. W. Cummings, Phys. Rev. **140**, A1051 (1965).

[83] R. J. Schoelkopf and S. M. Girvin, Nature **451**, 664 (2008).

[84] R. J. Thompson, G. Rempe, and H. J. Kimble, Physical Review Letters **68**, 1132 (1992).

[85] L. S. Bishop, J. M. Chow, J. Koch, A. A. Houck, M. H. Devoret, E. Thuneberg, S. M. Girvin, and R. J. Schoelkopf, Nature Physics **5**, 105 (2009).

[86] S. Haroche and J. M. Raimond, *Exploring the Quantum* (Oxford Univ. Press, 2006).

[87] J.-M. Raimond, M. Brune, and S. Haroche, Reviews of Modern Physics **73**, 565 (2001).

[88] MinutePhysics, "2012 noble prize physics," .

[89] S. Gleyzes, S. Kuhr, C. Guerlin, J. Bernu, S. Deleglise, U. B. Hoff, M. Brune, J.-M. Raimond, and S. Haroche, Nature **446**, 297 (2007).

[90] A. Blais, R.-S. Huang, A. Wallraff, S. M. Girvin, and R. J. Schoelkopf, Physical Review A **69**, 062320 (2004).

[91] V. Bouchiat, D. Vion, P. Joyez, D. Esteve, and M. H. Devoret, Physica Scripta **1998**, 165 (1998).

[92] J. Koch, M. Y. Terri, J. Gambetta, A. A. Houck, D. I. Schuster, J. Majer, A. Blais, M. H. Devoret, S. M. Girvin, and R. J. Schoelkopf, Phys. Rev. A **76**, 042319 (2007).

[93] J. Schreier, A. A. Houck, J. Koch, D. I. Schuster, B. Johnson, J. Chow, J. M. Gambetta, J. Majer, L. Frunzio, M. H. Devoret, *et al.*, Physical Review B **77**, 180502 (2008).

[94] D. I. Schuster, *Circuit Quantum Electrodynamics*, Ph.D. thesis, Yale University (2007).

[95] V. E. Manucharyan, J. Koch, L. I. Glazman, and M. H. Devoret, Science **326**, 113 (2009).

[96] V. E. Manucharyan, *Superinductance*, Ph.D. thesis, Yale University (2012).

[97] M. H. Devoret, Les Houches, Session LXIII (1995).

[98] L. S. Bishop, *Circuit Quantum Electrodynamics*, Ph.D. thesis, Yale University (2010).

[99] S. M. Girvin, *Circuit QED: Superconducting Qubits Coupled to Microwave Photons* (Oxford University Press, 2012).

[100] A. Wallraff, D. I. Schuster, A. Blais, L. Frunzio, R.-S. Huang, J. Majer, S. Kumar, S. M. Girvin, and R. J. Schoelkopf, Nature **431**, 162 (2004).

[101] K. Geerlings, Z. Leghtas, I. M. Pop, S. Shankar, L. Frunzio, R. J. Schoelkopf, M. Mirrahimi, and M. H. Devoret, Phys. Rev. Lett. **110**, 120501 (2013).

[102] S. E. Nigg, H. Paik, B. Vlastakis, G. Kirchmair, S. Shankar, L. Frunzio, M. H. Devoret, R. J. Schoelkopf, and S. M. Girvin, Phys. Rev. Lett. **108**, 240502 (2012).

[103] M. H. Devoret, S. M. Girvin, and R. J. Schoelkopf, Annalen der Physik **16**, 767 (2007).

[104] J. Johansson, P. Nation, and F. Nori, Comput. Phys. Commun. **184**, 1234 (2013).

[105] J. Niemeyer and V. Kose, Appl. Phys. Lett. **29**, 380 (1976).

[106] G. J. Dolan, Appl. Phys. Lett. **31**, 337 (1977).

[107] K. L. Geerlings, *Improving Coherence of Superconducting Qubits and Resonators*, Ph.D. thesis, Yale University (2013).

[108] A. Wallraff, D. I. Schuster, A. Blais, L. Frunzio, J. Majer, M. H. Devoret, S. M. Girvin, and R. J. Schoelkopf, Phys. Rev. Lett. **95**, 060501 (2005).

[109] R. Vijay, D. H. Slichter, and I. Siddiqi, Phys. Rev. Lett. **106**, 110502 (2011).

[110] R. Vijay, C. Macklin, D. H. Slichter, S. J. Weber, K. Murch, R. Naik, A. N. Korotkov, and I. Siddiqi, Nature **490**, 77 (2012).

[111] L. Sun, A. Petrenko, Z. Leghtas, B. Vlastakis, G. Kirchmair, K. M. Sliwa, A. Narla, M. Hatridge, S. Shankar, J. Blumoff, L. Frunzio, M. Mirrahimi, M. H. Devoret, and R. J. Schoelkopf, Nature **511**, 444 (2014).

[112] J. Kelly, R. Barends, A. G. Fowler, A. Megrant, E. Jeffrey, T. C. White, D. Sank, J. Y. Mutus, B. Campbell, Y. Chen, Z. Chen, B. Chiaro, A. Dunsworth, I. C. Hoi, C. Neill, P. J. J. O'Malley, C. Quintana, P. Roushan, A. Vainsencher, J. Wenner, A. N. Cleland, and J. M. Martinis, Nature **519**, 66 (2015).

[113] D. Ristè, C. C. Bultink, K. W. Lehnert, and L. DiCarlo, Phys. Rev. Lett. **109**, 240502 (2012).

[114] D. Ristè, M. Dukalski, C. A. Watson, G. de Lange, M. J. Tiggelman, Y. M. Blanter, K. W. Lehnert, R. N. Schouten, and L. DiCarlo, Nature **502**, 350 (2013).

[115] D. Riste, S. Poletto, M. Z. Huang, A. Bruno, V. Vesterinen, O. P. Saira, and L. DiCarlo, Nat. Commun. **6** (2015).

[116] B. Vlastakis, A. Petrenko, N. Ofek, L. Sun, Z. Leghtas, K. Sliwa, Y. Liu, M. Hatridge, J. Blumoff, L. Frunzio, *et al.*, arXiv preprint arXiv:1504.02512 (2015).

[117] A. D. Córcoles, E. Magesan, S. J. Srinivasan, A. W. Cross, M. Steffen, J. M. Gambetta, and J. M. Chow, Nat. Commun. **6** (2015).

[118] M. D. Reed, L. DiCarlo, B. R. Johnson, L. Sun, D. I. Schuster, L. Frunzio, and R. J. Schoelkopf, Phys. Rev. Lett. **105**, 173601 (2010).

[119] H. Wiseman, Phys. Rev. A **49**, 2133 (1994).

[120] A. C. Doherty, S. Habib, K. Jacobs, H. Mabuchi, and S. M. Tan, Phys. Rev. A **62**, 012105 (2000).

[121] H. M. Wiseman and G. J. Milburn, *Quantum Measurement and Control* (Cambridge University Press, 2009).

[122] R. J. Nelson, Y. Weinstein, D. Cory, and S. Lloyd, Phys. Rev. Lett. **85**, 3045 (2000).

[123] W. P. Smith, J. E. Reiner, L. A. Orozco, S. Kuhr, and H. M. Wiseman, Phys. Rev. Lett. **89**, 133601 (2002).

[124] R. L. Cook, P. J. Martin, and J. M. Geremia, Nature **446**, 774 (2007).

[125] G. Gillett, R. Dalton, B. Lanyon, M. Almeida, M. Barbieri, G. J. Pryde, J. O'brien, K. Resch, S. Bartlett, and A. White, Phys. Rev. Lett. **104**, 080503 (2010).

[126] J. M. Geremia, Phys. Rev. Lett. **97**, 073601 (2006).

[127] I. Dotsenko, M. Mirrahimi, M. Brune, S. Haroche, J.-M. Raimond, and P. Rouchon, Physical Review A **80**, 013805 (2009).

[128] C. Sayrin, I. Dotsenko, X. Zhou, B. Peaudecerf, T. Rybarczyk, S. Gleyzes, P. Rouchon, M. Mirrahimi, H. Amini, M. Brune, *et al.*, Nature **477**, 73 (2011).

[129] X. Zhou, I. Dotsenko, B. Peaudecerf, T. Rybarczyk, C. Sayrin, S. Gleyzes, J. M. Raimond, M. Brune, and S. Haroche, Phys. Rev. Lett. **108**, 243602 (2012).

[130] B. Peaudecerf, C. Sayrin, X. Zhou, T. Rybarczyk, S. Gleyzes, I. Dotsenko, J. Raimond, M. Brune, and S. Haroche, Phys. Rev. A **87**, 042320 (2013).

[131] I. Siddiqi, R. Vijay, F. Pierre, C. M. Wilson, M. Metcalfe, C. Rigetti, L. Frunzio, and M. Devoret, Phys. Rev. Lett. **93**, 207002 (2004).

[132] R. Vijay, M. H. Devoret, and I. Siddiqi, Review of Scientific Instruments **80**, 111101 (2009).

[133] N. Bergeal, R. Vijay, V. E. Manucharyan, I. Siddiqi, R. J. Schoelkopf, S. M. Girvin, and M. H. Devoret, Nature Phys. **6**, 296 (2010).

[134] N. Bergeal, F. Schackert, M. Metcalfe, R. Vijay, V. E. Manucharyan, L. Frunzio, D. E. Prober, R. J. Schoelkopf, S. M. Girvin, and M. H. Devoret, Nature **465**, 64 (2010).

[135] S. B. Bravyi and A. Y. Kitaev, arXiv preprint quant-ph/9811052 (1998).

[136] A. Y. Kitaev, Ann. Phys. **303**, 2 (2003).

[137] R. Raussendorf and J. Harrington, Phys. Rev. Lett. **98**, 190504 (2007).

[138] A. G. Fowler, A. M. Stephens, and P. Groszkowski, Phys. Rev. A **80**, 052312 (2009).

[139] A. G. Fowler, M. Mariantoni, J. M. Martinis, and A. N. Cleland, Phys. Rev. A **86**, 032324 (2012).

[140] M. Mirrahimi, Z. Leghtas, V. V. Albert, S. Touzard, R. J. Schoelkopf, L. Jiang, and M. H. Devoret, New J. Phys. **16**, 045014 (2014).

[141] J. F. Poyatos, J. I. Cirac, and P. Zoller, Phys. Rev. Lett. **77**, 4728 (1996).

[142] S. Diehl, A. Micheli, A. Kantian, B. Kraus, H. Büchler, and P. Zoller, Nature Phys. **4**, 878 (2008).

[143] B. Kraus, H. P. Büchler, S. Diehl, A. Kantian, A. Micheli, and P. Zoller, Phys. Rev. A **78**, 042307 (2008).

[144] C. A. Muschik, E. S. Polzik, and J. I. Cirac, Phys. Rev. A **83**, 052312 (2011).

[145] H. Krauter, C. A. Muschik, K. Jensen, W. Wasilewski, J. M. Petersen, J. I. Cirac, and E. S. Polzik, Phys. Rev. Lett. **107**, 080503 (2011).

[146] A. Sarlette, J.-M. Raimond, M. Brune, and P. Rouchon, Phys. Rev. Lett. **107**, 010402 (2011).

[147] J. T. Barreiro, M. Müller, P. Schindler, D. Nigg, T. Monz, M. Chwalla, M. Hennrich, C. F. Roos, P. Zoller, and R. Blatt, Nature **470**, 486 (2011).

[148] C. A. Muschik, H. Krauter, K. Jensen, J. M. Petersen, J. I. Cirac, and E. S. Polzik, J. Phys. B: At. Mol. Opt. Phys. **45**, 124021 (2012).

[149] K. Vollbrecht, C. A. Muschik, and J. I. Cirac, Phys. Rev. Lett. **107**, 120502 (2011).

[150] Z. Leghtas, U. Vool, S. Shankar, M. Hatridge, S. M. Girvin, M. H. Devoret, and M. Mirrahimi, Phys. Rev. A **88**, 023849 (2013).

[151] J. Cohen and M. Mirrahimi, Phys. Rev. A **90**, 062344 (2014).

[152] A. Metelmann and A. A. Clerk, Phys. Rev. Lett. **112**, 133904 (2014).

[153] C. Aron, M. Kulkarni, and H. E. Türeci, Phys. Rev. A **90**, 062305 (2014).

[154] A. Roy, Z. Leghtas, A. D. Stone, M. H. Devoret, and M. Mirrahimi, Phys. Rev. A **91**, 013810 (2015).

[155] V. V. Albert, S. Krastanov, C. Shen, R.-B. Liu, R. J. Schoelkopf, M. Mirrahimi, M. H. Devoret, and L. Jiang, arXiv preprint arXiv:1503.00194 (2015), 1503.00194 .

[156] K. W. Murch, U. Vool, D. Zhou, S. J. Weber, S. M. Girvin, and I. Siddiqi, Phys. Rev. Lett. **109**, 183602 (2012).

[157] S. Shankar, M. Hatridge, Z. Leghtas, K. Sliwa, A. Narla, U. Vool, S. M. Girvin, L. Frunzio, M. Mirrahimi, and M. H. Devoret, Nature **504**, 419 (2013).

[158] Z. Leghtas, S. Touzard, I. M. Pop, A. Kou, B. Vlastakis, A. Petrenko, K. M. Sliwa, A. Narla, S. Shankar, M. J. Hatridge, M. Reagor, L. Frunzio, R. J. Schoelkopf, M. Mirrahimi, and M. H. Devoret, Science **347**, 853 (2015).

[159] Y. Lin, J. P. Gaebler, F. Reiter, T. R. Tan, R. Bowler, A. S. Sørensen, D. Leibfried, and D. J. Wineland, Nature **504**, 415 (2013).

[160] G. Kirchmair, B. Vlastakis, Z. Leghtas, S. E. Nigg, H. Paik, E. Ginossar, M. Mirrahimi, L. Frunzio, S. M. Girvin, and R. J. Schoelkopf, Nature **495**, 205 (2013).

[161] Y. Hu, G.-Q. Ge, S. Chen, X.-F. Yang, and Y.-L. Chen, Phys. Rev. A **84**, 012329 (2011).

[162] J. Gambetta, A. Blais, D. I. Schuster, A. Wallraff, L. Frunzio, J. Majer, M. H. Devoret, S. M. Girvin, and R. J. Schoelkopf, Phys. Rev. A **74**, 042318 (2006).

[163] B. Vlastakis, G. Kirchmair, Z. Leghtas, S. E. Nigg, L. Frunzio, S. M. Girvin, M. Mirrahimi, M. H. Devoret, and R. J. Schoelkopf, Science **342**, 607 (2013).

[164] A. A. Clerk, M. H. Devoret, S. M. Girvin, F. Marquardt, and R. J. Schoelkopf, Rev. Mod. Phys. **82**, 1155 (2010).